Spring 2020

TEMPLATED SINGLE-CHAIN POLYMER-BASED ELECTROCHEMICAL SENSING

HABIB MUHAMMAD NAZIR AHMAD
University of New Hampshire, Durham

Recommended Citation

AHMAD, HABIB MUHAMMAD NAZIR, "TEMPLATED SINGLE-CHAIN POLYMER-BASED ELECTROCHEMICAL SENSING" (2020). *Master's Theses and Capstones*. 1360.
https://scholars.unh.edu/thesis/1360

TEMPLATED SINGLE-CHAIN POLYMER-BASED ELECTROCHEMICAL SENSING

BY

HABIB MUHAMMAD NAZIR AHMAD

THESIS

Submitted to the University of New Hampshire
in Partial Fulfillment of
the Requirements for the Degree of

Master of Science

in

Electrical and Computer Engineering

May 2020

This thesis has been examined and approved in partial fulfillment of the requirements for the degree of Master of Science in Electrical and Computer Engineering by:

Edward Song, Assistant Professor, Electrical and Computer Engineering

John LaCourse, Professor, Electrical and Computer Engineering

W. Rudolf Seitz, Professor, Chemistry

On May 2020

Original approval signatures are on file with the University of New Hampshire Graduate School.

ACKNOWLEDGEMENTS

I would like to acknowledge the Department of Electrical and Computer Engineering for my graduate study. I would like to thank Professor Dr. Edward Song for giving me chance to work in BioMEMS lab. His encouragement convinced me to pursue cross disciplinary research. I also thank heartfully to Dr. Gaurab Dutta, Post-Doctoral Fellow and Bo Si, PhD student for guiding me time to time. I also thank John Csoros, PhD student in Seitz lab for synthesizing the polymers for characterization and sensing experiments.

I would like to express my gratitude to Professor W. Rudolf Seitz and Professor John LaCourse for serving on my committee and for being helpful during my graduate career.

This thesis is dedicated to my beloved parents and wife. The support of my parents and sacrifice of my wife helped me accomplishing all the hard works in last two years.

TABLE OF CONTENTS

LIST OF TABLES

LIST OF FIGURES

ABSTRACT

TEMPLATED SINGLE-CHAIN POLYMER-BASED ELECTROCHEMICAL SENSING

By

Habib Muhammad Nazir Ahmad

University of New Hampshire

A target receptor is an essential component in developing selective biological and chemical sensors. Among various approaches in receptor implementation, templated polymers are synthetic biochemical receptors that mimic natural molecular recognition. They have the favorable arrangement of polymer structures to be steady in harsh conditions and can also be custom tailored to exhibit target affinity as well as interfacing with transducers. Effective templated polymer synthesis depends on the co-polymerization of functional monomers which will interact with the sensing molecule. This thesis proposes a rational design approach towards the integration of templated polymers with electrochemical sensing. The synthesized single-chain label-free flexible polymers with binding sites show selective affinity toward both electroactive and non-electroactive target molecule.

This thesis proposes a novel approach in electrochemical templated polymer-based sensing platform. The developed platform shows binding-induced changes in the electron transfer kinetics at the templated polymer-attached electrode when the target molecule binds specifically to the receptor. In this work, a stimuli-responsive single-chain copolymer was developed for explicit analyte detection of 4-nitrophenol, a neurotoxin and environmental pollutant, and L-glutamate, a

well-known neurochemical. The polymer backbone experiences a conformation change upon template binding and the electrochemical measurement can be used to characterize these changes. This new detection approach can be used for label-free sensing of various non-electroactive chemical species and can potentially lead to the development of a non-enzymatic electrochemical sensors.

LIST OF ABBREVIATIONS

AA	acrylic acid
AAm	acrylamide
ACN	acetonitrile
AcOH	acetic acid
AFM	atomic force microscopy
AIBN	azo-bis-isobutyronitrile
ATRP	atom transfer radical polymerization
BE	binding energy
CP	control polymer
CRP	controlled radical polymerization
CV	cyclic voltammetry
DDMAT	2-(Dodecylthiocarbonothioylthio)-2-methylpropionic acid
DMSO	dimethyl sulfoxide
DLS	dynamic Light Scattering
DPV	differential Pulse Voltammetry
EIS	electrochemical impedance spectroscopy
ELISA	enzyme-linked immunosorbent assay
EtOH	ethanol
EV	electron volt
FRP	free radical polymerization
FTIR	fourier-transform infrared spectra
FWHM	full width at half maximum
HPLC	high performance liquid chromatography
IF	imprinting factor
LCST	Lower Critical Solution Temperature
LOD	limit of detection
MAA	methacrylic acid
MAm	meth acrylamide
MeOH	methanol

MIP	molecularly imprinted polymer
MISPE	molecular imprinted solid phase extraction
MS	mass spectrometry
NIP	non-imprinted polymer
NIPAm	N-isopropylacrylamide
NMR	nuclear magnetic resonance
NPs	nanoparticles
PBS	phosphate buffered saline
QCM	quartz crystal microbalance
QD	quantum dot
RAFT	reversible addition-fragmentation chain transfer
RSF	relative sensitivity factor
SEM	scanning electron microscopy
SERS	surface-enhanced Raman spectroscopy
SPR	surface plasmon resonance
TEM	transmission electron microscopy
TP	templated polymer
UV	ultraviolet
4NP	4-Nitrophenol
3NP	3-Nitrophenol
4VP	4-vinylpyridine

CHAPTER 1: INTRODUCTION

1.1 OVERVIEW

Most biosensing techniques require both accurate and selective recognition of the target analyte. Antibodies and enzymes are common examples that are used to achieve these prerequisites. Since these are biomolecules, their molecular structures and functionalities can be delicate which may require them to be utilized under gentle conditions. For example, denaturation of the protein can occur if the temperature or the pH is in the range that is hostile to the biomolecule. Moreover, immobilization of such biomolecules to certain surfaces, such as electrodes, can be challenging. The high cost and complexity of manufacturing such bioreceptors can be another factor to take into consideration when using the material. For instance, the cost of antibodies can be in the range \$100–1000 mg^{-1}[1]. Therefore, it is of great interest to develop artificial and synthetic receptors that can overcome some of the limitations that are inherent in natural target receptors.

As an alternative approach to natural bioreceptors, artificial templated polymers, often referred to as templated polymer (TP) have been investigated over the years [2]–[4]. Templated polymers display two significant highlights of natural receptors—the capacity to recognize and bind specifically to the target molecule. Nonetheless, traditional templated polymers contrast from organic receptors in that they are bulky, non-flexible, and insoluble, while their natural counterparts are small, adaptable and in many examples, soluble. Contingent upon their size, templated polymers can have a large number of randomly positioned binding sites [2], whereas the natural receptors such as antibodies typically have one binding site per unit. Moreover, templated polymers tend to be a highly crosslinked bulk matrix, and therefore the ability of the target molecules to access the binding sites may be significantly limited.

For the reasons mentioned above, templated polymers are not being used effectively as a substitute for natural antibodies in real applications. The goal of this thesis is to investigate a new approach to molecular templating that mimics the naturally occurring bioreceptors in terms of target recognition. In general, templated polymers consist of monomers that form the backbone structure of the polymer and functional monomers that interacts with the template molecules that exhibit affinity and binding.

1.2 MOTIVATION

Fast identification of low concentration of target analytes in small volumes is crucial in the early point of-care analysis. While traditional optical based identification is highly sensitive [5], [6], often requires tedious operating procedures, expensive and complex imaging instrumentation, and advanced image processing software. On the other hand, electrochemical biosensors using enzyme modified electrodes, also known as enzymatic electrochemical biosensors, have gained significant consideration, because of their high affinity and selectivity. Electrochemical sensing is more sensitive as it directly interprets electrochemical signals generated in the sensing mechanism of redox reaction between target molecules and surface on the working electrode often termed as the electron exchange of redox reaction. Enzymes are selected biocatalysts that perform and control certain procedures in living frameworks. The execution of the enzymatic electrochemical biosensors relies upon the immobilization of catalysts on the electrode surface [7], [8]. Responsive oxygen species (ROS) is known to play a critical role in controlling protein mixtures, DNA damage, cell apoptosis, and other functionalities. ROS also takes part in some physiological processes such as signal change [9], [10]. However, aggregation of such ROS in cells causes harmful effects to the cells and tissues [11]. Hydrogen peroxide (H_2O_2) is the most widely recognized example of ROS since it can penetrate into the cell compartments with long lifetime to initiate various destructive changes [12]. The concentration of H_2O_2 is fairly low under typical physiological conditions but can increase to $\sim 10^{-3}$ M under influence such as severe cerebrum damage, ischemia-reperfusion, and natural anxieties. [13], [14]

Therefore, the exact recognition and quantification of H_2O_2 in cells and estimations of its dynamic discharge process from living cells are vital for illuminating the cellular signal transduction pathways and for potentially developing clinical treatments and therapy. So far, numerous systems have been developed for the detection of H_2O_2, including colorimetry [15], fluorescence [16], [17], chromatography [18], chemiluminescence [19], and electrochemistry [20], [21]. Among these systems, electrochemical methods, particularly the catalyst-based sensors, have been produced for detecting H_2O_2 because of their excellent sensing performances. However, such enzyme-based biosensors still suffer from instability and poor reproducibility due to the highly sensitive nature of the enzyme catalytic activity that is heavily influenced by the surrounding environment.

In recent years, considerable effort has been made in developing non-enzymatic electrochemical sensors in the hopes of improving the sensor’s reproducibility by eliminating the need for the highly unstable catalysts [22], [23]. Different nanomaterials including metals [24], [25], metal oxides [26], and carbon materials [27], [28] had been utilized to create non-enzymatic sensors because of their high surface area and reactivity as well as their effective charge transfer capabilities. Natural recognition components have high affinity to their targets, but it is quite impossible to use them in practical manner because of their volatility at extreme pressure, temperature. They also display less stability in organic solvents under pH changes [29] and require intermediate assay format to measure generated signal.

Molecular imprinting or templating has been widely used to address most of these drawbacks. Templated polymers (TPs) can be synthesized using different types and mixtures of functional monomers, cross-linkers, initiators and solvents. Templated polymer (TP) based bioprobes and biosensors are easily assembled for further modifications to produce unique structures. Conventional templated polymers are synthesized by bulk polymerization [30] sol–gel processes[31] and emulsion polymerization[32]. Most of these methods require high percentages of cross-linkers. And the synthesized materials are not flexible enough for diverse application. These techniques heavily rely on highly crosslinked structure. Templates buried deep inside can't be removed easily. Highly crosslinked structure also limits the diffusion of template molecules into binding sites.

To address the existing challenges of traditional templated polymeric material Grenier et al. proposed an alternative technique[33] where traditional covalent crosslinking is reduced and non-covalent crosslinking is introduced for retaining the template binding sites. Non-covalent crosslinking includes electronic interactions, acid-base crosslinking and π-π interaction.

1.3 THESIS OBJECTIVES

The goal of this thesis is to develop a non-enzymatic label-free molecularly templated polymer-based biosensing platform with high sensitivity and selectivity for neurochemical detection and to demonstrate that templated polymers can be a viable solution to implementing a label-free biosensing. The specific objectives of this work are the following:

1. Characterize the in-house synthesized templated polymer using three spectroscopy techniques: Fourier-transform infrared spectroscopy (FTIR), X-ray photoelectron spectroscopy (XPS), and Nuclear Magnetic Resonance (NMR).

2. Characterize the effects of electrode surface coverage upon templated polymer deposition using electrochemical analysis.
3. Determine the approximate polymer concentration and deposition time for optimal sensing performances.
4. Characterize the deposition rate kinetics with and without the reducing agent.
5. Use molecular templating technique to create artificial target receptors for detecting electroactive and non-electroactive species such as 4-nitrophenol and N-methyl glutamate, respectively.
6. Characterize the limit of detection and selectivity for the specific analyte using the developed sensing platform.

1.4 THESIS OUTLINE

Chapter 2 gives background information on biosensors, discussing in detail TP based electrochemical biosensors, three electrode method and electrode electrolyte interface theory. Chapter 3 discusses on the materials needed for synthesis and methods for data acquisition for proposed templated polymer-based sensor. Chapter 4 analyzes the characteristics of synthesized homo and templated PNIPAM polymers with data obtained from FTIR, XPS,NMR experiments.

Chapter 5 demonstrates electrochemical results from PNIPAM attached gold electrodes for different condition. Chapter 6 and 7 presents sensing mechanism for 4-Nitrophenol and N Methyl Glutamate respectively using the proposed polymeric sensing platform.

CHAPTER 2: THEORETICAL BACKGROUND

2.1. OVERVIEW

This chapter will give a general idea of biosensors and their classifications. Most widely used electrochemical biosensors and sensing techniques like cyclic voltammetry, electrochemical impedance spectroscopy, differential pulse voltammetry, square wave voltammetry and linear sweep voltammetry are introduced in this chapter. Templated polymer based electrochemical biosensor fabrication and their application is also briefly presented. Integral parts of electrochemical sensing, three electrode setup and electrode electrolyte interphase mechanism are also discussed here.

2.2. BIOSENSORS

Detection of biomolecules plays a critical role in many areas of human life including healthcare, ecological and environmental monitoring, rural and agricultural fields, biosecurity, and defense. Biosensors are diagnostic devices that are made to identify or quantify a certain type of chemical or molecular species, known as analyte, that exist in a human body. Some examples of an analyte include hormones, metabolites, neurochemicals, proteins, DNAs. Biosensors can help identify pathogens, infections, poisons and other abnormalities in our health by measuring certain health indicators or biomarkers [34]. As per the International Union of Pure and Applied Chemistry (IUPAC) terminology, a biosensor is characterized as an analytical gadget that is fit for giving quantitative or semi-quantitative data utilizing explicit biochemical responses with a physicochemical identifier [35]. There has been an extensive amount of research performed for the advancement of biosensors that are sensitive, specific, robust, versatile, and affordable. A typical biosensor contains the arrangement of an explicit probe–target complex in a coupling structure that results in a target recognition and transduction into signal readout [36]. Some examples of transduction mechanisms include electrochemical [34], [37]–[41], optical [42]–[44], piezoelectric [45], [46] and magnetic [47]–[49]. Figure 2.1 shows an example of an electrochemical biosensing platform where bio analyte is captured by sensing platform and reaction during reception is interpreted to meaningful electrochemical signal by a transducer called potentiostat.

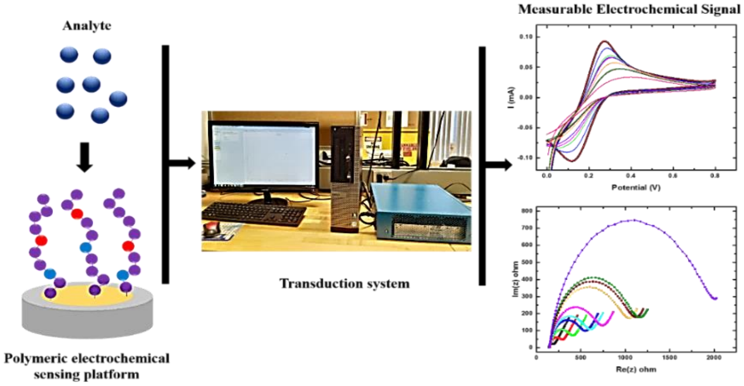

Figure 2.1: General representation of Electrochemical Biosensing Platform

2.3. ELECTROCHEMICAL BIOSENSORS

Electrochemical biosensors are a part of the electrochemical cell that comprises of either two or three electrodes. An ordinary three terminal framework comprises of a working, a reference, and a counter electrode. The working terminal comprises of an electrochemically inert conductive material, usually platinum, gold, or carbon; the reference electrode typically comprises of silver metal covered with a layer of silver chloride (Ag/AgCl); and a platinum wire is commonly utilized as the counter electrode. A two-electrode method consists of working and reference electrodes only [37]. Three main types of measurement are done in electrochemical sensing platform: (1) current measurement (voltammetric and amperometric), (2) potential difference measurement (potentiometry), (3) impedance measurement (electrochemical impedance spectroscopy). The current-based sensors are implemented by applying a voltage to the working electrode with respect to the reference electrode and measuring the current generated. In scanning voltammetry, in particular, a voltage is scanned over a predefined voltage window, and the response of the produced current corresponds to the concentration of the analyte in the sample. Popular voltammetric methods are linear sweep, cyclic, hydrodynamic, differential pulse, square-wave, and stripping voltammetry as shown in Figure 2.2. In amperometric sensing, a steady potential is applied at the working electrode with respect to the reference electrode, and the adjustments in the current caused by the electrochemical reduction or oxidation are specifically observed as a function of time. In Potentiometric sensing, current flow is absent and potential difference between two electrodes is estimated. Then analyte concentration can be interpreted from that measured potential. Potentiometric sensors are non-invasive, low cost, and enables real-time detection

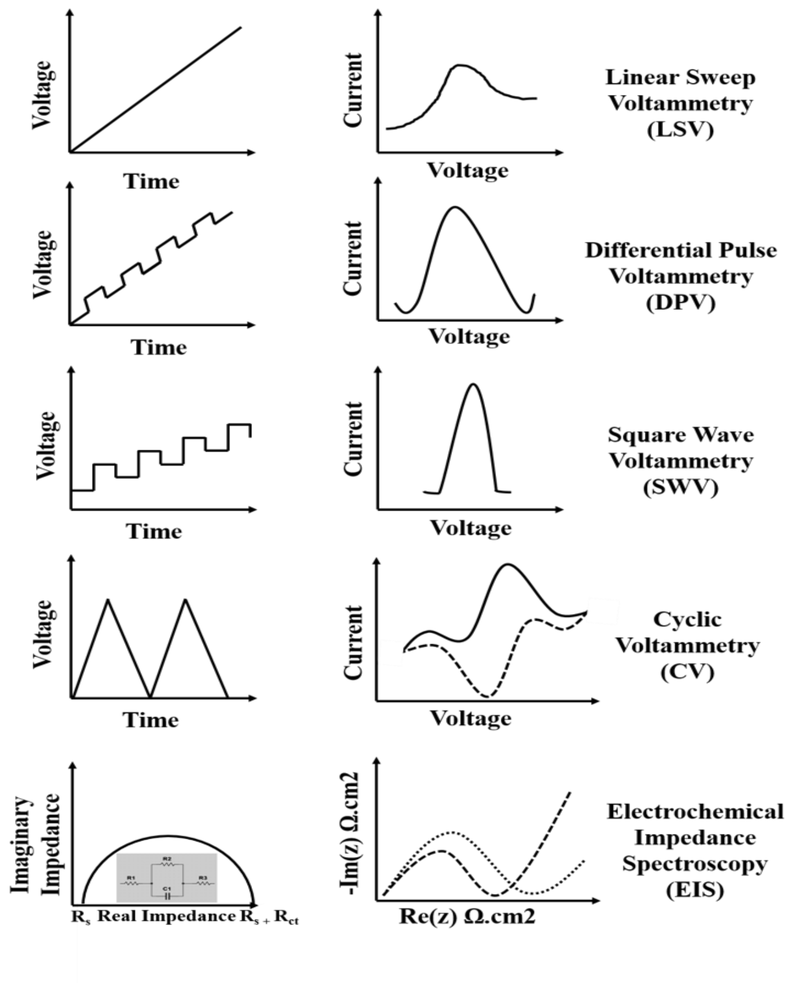

Figure 2.2: Electrochemical sensing techniques

while drawing a negligible amount of current [50]. Electrochemical impedance spectroscopy (EIS) measures the charge transfer impedances and capacitances at the liquid-electrode interface by supplying a low amplitude sinusoidal AC excitation signal. The frequency is varied over a wide range to generate the impedance spectrum. The in-phase and out-of-phase component of AC current responses are interpreted into a circuit structure to obtain the resistive and capacitive components of the impedance. In EIS, mass transfer is dominant at low frequency and charge transfer is dominant at high frequency: this phenomenon can be used effectively in affinity-based biosensing [51].

2.4. TEMPLATED POLYMER BASED ELECTROCHEMICAL BIOSENSORS

Templated polymers (TP)s are artificial target receptors, typically made with polymers, that mimic the function of naturally existing receptors such as antibodies. There has been an abundance of work in the literature demonstrating the potential of templated polymers as a synthetic functioning molecular receptors [52]. A typical procedure for synthesizing a templated polymer involves incorporation of template molecules, functional monomers, reagents for crosslinking, and a radical initiator for polymerization. The functional monomers exhibit affinity with the template molecules through non-covalent bonding (e.g. hydrogen bond, ionic and hydrophobic interactions). A general mechanism by which TPs are synthesized can be broken down into 3 parts: (1) self-assembly of template molecules along with the surrounding monomers; (2) polymerization and cross-linking are initiated forming a template-receptor complex; (3) the removal of the templates from the polymer by elution with a solvent [53]. Figure 2.3 shows a schematic representation of TP principle.

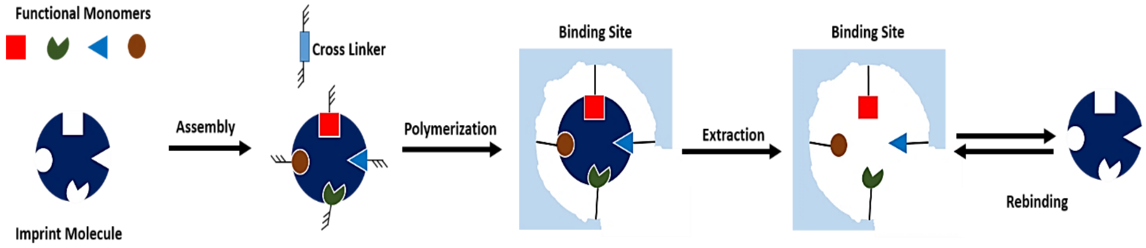

Figure 2.3: Templating Principle

Since polymers are generally more stable than proteins, it is expected that templated polymers would also be more stable than their biological counterparts (e.g. antibodies) under a wide range of pH and temperature. In some cases, templated polymers can bind to the targets with the specificity and affinity that are comparable to natural receptors [54].

TP-based electrochemical biosensors (ECBSs) combine the advantages from both TPs and ECBSs, including superior selectivity, chemical stability, reusability, effortless readiness, low manufacturing cost, automation and miniaturization [53]. TPs-based ECBSs have been extensively utilized for the investigation of vital biomolecules such as proteins, hormones, drugs and nucleic acids as well as in organic analysis, ecological monitoring and food safety evaluation [55].

The combination of TPs as recognition elements and electrochemical devices as a detection platform is promising for creating high performance biosensors [56]. High specificity of targets and accurate detection capability are primary requirements for manufacturing efficient biosensor [57]. Enlarging the effective surface area of the sensor can also enhance the sensitivity of the TP-based ECBs [58]. The ability of TPs to bind selectively to the target analyte enables this sensing platform to be used in environment that may contain interfering species [59]. Depending on the type of the template molecule, the choice of monomers for the templated polymer are selected. The choice for the functional monomers is critical in promoting affinity between the template and the receptor. Methacrylate-based [60]–[69] and vinyl-based [62], [70], [71] monomers are regularly utilized for TPs blend through a free radical system [72]. Moreover, silane-based monomers [73]–[75], pyrrole subsidiaries [76]–[78], and p-aminothiophenol [79]–[81] have also been used as functional monomers. Traditionally, templated polymers are highly crosslinked to retain the 3-dimensional geometry of the synthetic target receptor. The crosslinkers that are often used in molecular templating include methacrylate-based chemicals [82]–[85], thiophenes [86], [87], silanes [73], [88], glutharaldehyde [89], and N,N'-methylene bis-acrylamide [60]. The cross-linker is believed to play a pivotal role in maintaining the structural integrity of the polymer, hence it is a crucial ingredient in templated polymer synthesis [90]–[93].

Although cyclic voltammetry (CV) is one of the most widely used electrochemical technique, it is not often used in sensing applications. This is because the rate of voltage sweep is relatively slow resulting in a substantial build-up of double layer capacitance at the electrode surface. This double layer capacitance creates a screening effect for the Faradaic current generated from the redox reaction resulting in reduced sensitivity. Therefore, CV is often used for qualitative analysis rather than quantitative ones, particularly the characterization of the imprinted surfaces [94].

As an alternative approach to CV, differential pulse voltammetry (DPV) is a more widely utilized technique for quantitative analysis [94]. Another technique with an exceptional flexibility is square wave voltammetry (SWV), which is considered one of the most sensitive voltammetric techniques due to its high signal-to-noise ratio and sensitivity [95], [96].

Electrochemical impedance spectroscopy (EIS) is a procedure that has the benefit of being non-invasive and minimally damaging to the electrode because of its low voltage application. The EIS technique involves applying a small amplitude AC voltage with a wide range of frequencies and observing the charge transfer impedance at the electrode. EIS can also be an effective biosensing technique where the change in impedance can be correlated with the amount of target analyte interacting with the electrode surface [97]. Figure 2.4 shows MIP-based Electrochemical sensing technique.

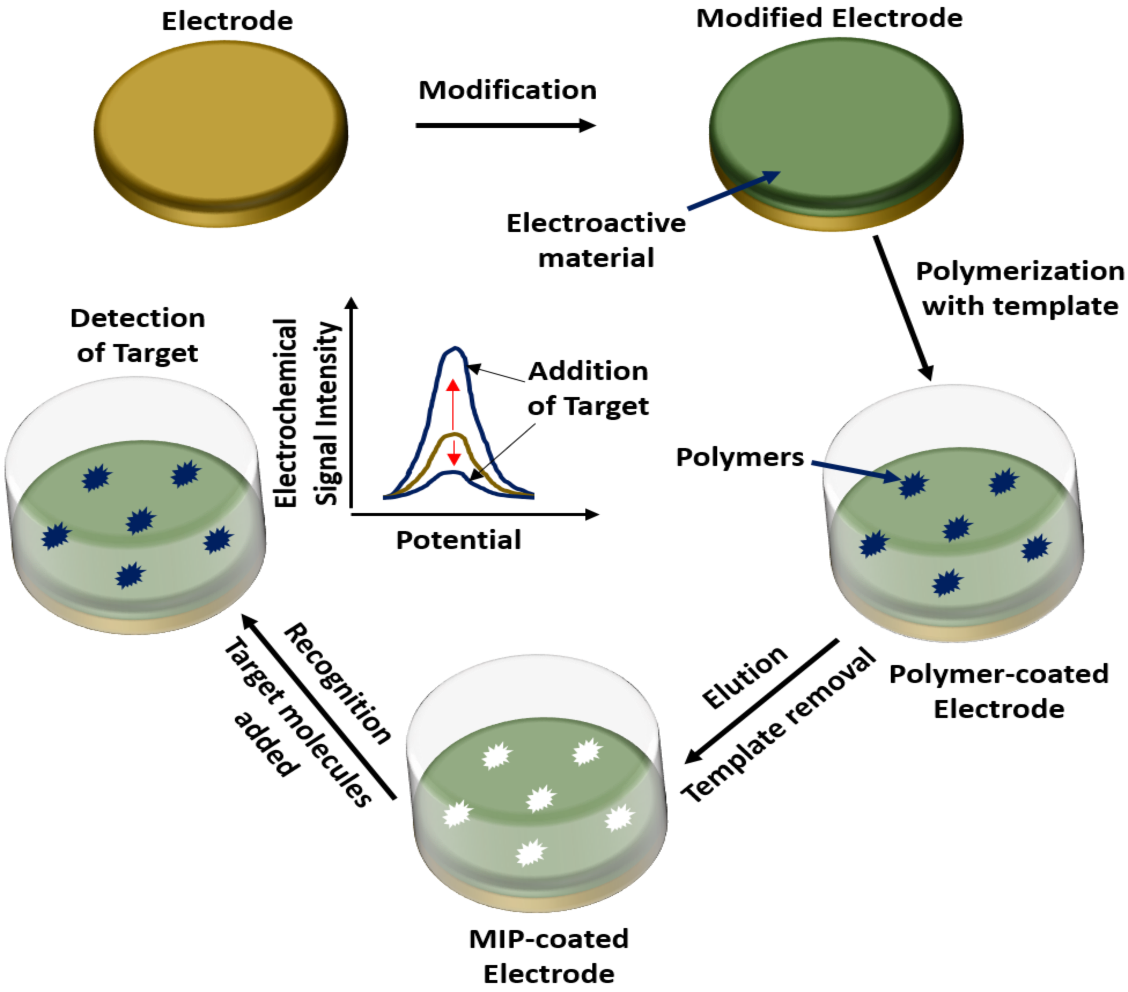

Fig 2.4: Schematic view of TP based ECB analyte detection technique

2.5. THREE ELECTRODE SETUP

An electrochemical experiment typically utilizes a potentiostat with a three-electrode setup that comprises of a working electrode (WE), a reference electrode (RE) and a counter electrode (CE) in an electrochemical cell containing an electrolyte. The RE is used to maintain a constant potential and serves as a reference for the potential control at the WE. The WE and the RE are typically positioned close together to minimize the ohmic drop over the electrolyte [94]. In some cases, it is required that the reactive oxygen species be completely removed from the cell to avoid its interference with the measurements. To minimize the presence of such oxygen, the arrangement is sparged with an inert gas such as nitrogen or argon for 5 – 10 minutes preceding the trial, and the cell is tightly sealed. The cell volume is also an important factor and ranges from microliters to tens of milliliter, depending on the objective of the investigation. Figure 2.5 shows a typical arrangement of a three-electrode electrochemical setup.

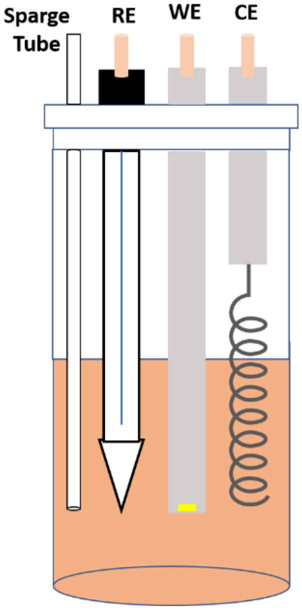

Fig 2.5: Schematic view of Three electrode electrochemical cell

2.6. THE ELECTRODE-ELECTROLYTE INTERPHASE

The investigation of an electric double layer (EDL) first began almost a century ago. Helmholtz was the first scientist to discover that an electrically charged electrode will draw in counterions from the electrolyte [98] to maintain charge neutrality. Figure 2.6 outlines the association of a (positively) charged metal electrode with the ionic zones of the aqueous electrolyte. The EDL that is shaped at the interface is depicted with the Bockris-Devanathan-Muller model, a further improvement of the Stern model. This model utilizes the fixed and the diffuse layers, and also includes polar molecules as well as adsorption of species at the electrode surface [99].

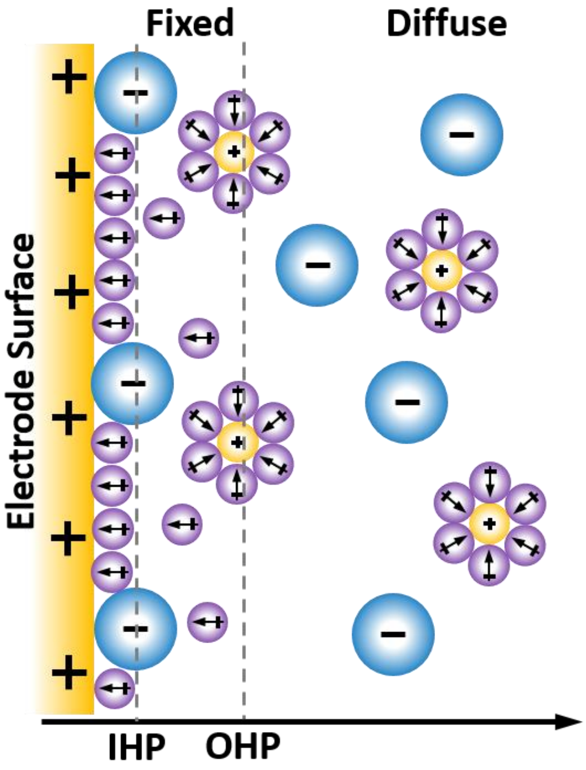

Fig 2.6: Electric Double Layer (EDL) with inner Helmholtz plane (IHP) and outer Helmholtz plane (OHP) at the electrode electrolyte interface, with contact adsorption of vast anions and solvated littler cations, which are not ready to cooperate with the terminal surface. The arrow in the dissolvable particles is pointing towards the negative dipole moment of the solvent.

Polar water molecules will align themselves at the cathode and is able to contact the electrode surface. The plane through the locus of these contact adsorbed species is called the inward Helmholtz plane (IHP). The solvated smaller cations are unable to interface with the electrode surface and are non-explicitly adsorbed, confined by the first layer of water atoms. The plane through their locus is known as the outer Helmholtz plane (OHP). Both Helmholtz planes are found inside the Helmholtz layer and the potential from the terminal surface over this layer drops linearly [100].

The EDL can be considered as a parallel-plate capacitor with two capacities in series when the whole system is at equilibrium and electrically neutral as described by the equation given below:

$$\frac{1}{C} = \frac{1}{C_f} + \frac{1}{C_d}$$

where C is the total capacitance, C_f is the capacitance of the fixed layer and C_d the capacitance of the diffuse layer. Changing electrolyte concentration, desorption furthermore, adsorption procedures can cause charge aggregation at the electrode electrolyte interface resulting in an expanded capacitance. Even though no charge is exchanged, an outer, non-faradaic current can be estimated. Interestingly, a faradaic current stream as the consequence of a charge exchange because of oxidation or on the other hand decrease responses at the interface [94] In electrochemical measurements, the oxidation and reduction (redox) reactions at the interface generate the faradaic current. The equilibrium potential for a redox system in aqueous solution is defined by the Nernst equation:

$$E = E^0 + \frac{RT}{nF} ln \frac{C_0}{C_R}$$

with E^0 is the standard potential, R being the universal gas constant, T the absolute temperature, C_O and C_R the concentrations of the oxidized and reduced form, respectively. In case of an inert (metal) electrode surface in contact with an electrolyte, the reduced component (*Red)* will be oxidized (to O_x) if a current pass through the electrode and the potential at the electrode is set above E as described by the equation below:

$$\text{Red} \leftrightarrow \text{Ox} + ne^-$$

The potential difference between the electrode potential and the equilibrium potential is the overpotential η.

Table 2.1 shows direction terminology depending on the current magnitude and overvoltage condition.

Redox reaction conventions			
Direction	Current	Overvoltage condition	Reaction
Anodic	$i > 0$	$\eta > 0$	$\text{Red} \rightarrow \text{Ox} + ne^-$
Cathodic	$i < 0$	$\eta < 0$	$\text{Ox} + ne^- \rightarrow \text{Red}$

Table 2.1 Redox reaction analogy

2.7 ELECTROCHEMICAL EXPERIMENTAL METHODS

In an electrochemical biosensor, an electrochemical transduction process converts a chemical reaction event into a measurable electrical signal. The electrochemical techniques can be applied to characterize the deposition of the polymer-based receptors on the electrode, the binding kinetics between the analyte and the receptors as well as the conformation change of the polymers upon target recognition. The electrochemical analysis can be achieved by measuring a change in the current at a fixed potential (amperometry), the conductivity (conductometry), the impedance (impedimetry) or the potential (potentiometry). The electrochemical measurements were performed by using a Bio Logic VSP potentiostat operated by EC lab V11.10 software package.

The electrochemical experiments were conducted in a traditional three-electrode cell configuration. A circular gold electrode with a diameter of 3mm was used as a working electrode, an Ag/AgCl was used as the reference electrode and a platinum electrode was used as counter electrode. All the potentials mentioned in the article are given with respect to the Ag/AgCl. All the electrochemical measurements (unless mentioned otherwise) were performed in a Tris buffer solution containing 5 mM $K_3[Fe(CN)_6]/K_4[Fe(CN)_6]$.

2.7.1. CYCLIC VOLTAMMETRY

Cyclic voltammetry (CV) is a broadly utilized electrochemical method [101] that can be utilized to obtain a characteristic behavior or phenomenon at the electrode surface [102]. The potential is applied at the working electrode (WE) with respect to the reference Ag/AgCl electrode (RE). As the potential is scanned positively (forward sweep) and becomes sufficiently positive to oxidize the $Fe(CN)_6^{4-}$ ions, the anodic current is generated due to the reaction occurring at the cathode:

$$Fe(CN)_6^{4-} \rightarrow Fe(CN)_6^{3-} + e$$

As the potential is further increased, most of the $Fe(CN)_6^{4-}$ species near the electrode surface would be consumed and the oxidation current decays. For the reverse direction of the voltage sweep, as the potential at the WE become sufficiently negative vs. RE, a reduction of $Fe(CN)_6^{3-}$ would occur causing the following reaction:

$$Fe(CN)_6^{3-} + e \rightarrow Fe(CN)_6^{4-}$$

The method of CV quickly produces different oxidation states. The amounts of note a CV plot are the anodic peak current i_{pa}, cathodic peak current i_{pc}, anodic peak potential E_{pa}, and cathodic peak potential E_{pc}. Estimating i_p involves the extrapolation of the standard current. A redox couple in which half responses quickly trade electrons at the working terminal are said to be electrochemically reversible couples.

The formal reduction potential $E^{o'}$ for such a reversible couple is the mean of anodic peak potential E_{pa} and cathodic peak potential E_{pc} and the magnitudes of the anodic peak current i_{pa} and the cathodic peak current i_{pc} are nearly identical.

$$E^{o\prime} = \frac{E_{pa} + E_{pc}}{2}$$

A reversible redox reaction also possesses the following relationship:

$$E_{pa} - E_{pc} = \frac{59\ mV}{n}$$

For a moderate electron transfer rate at the electrode surface, such as irreversible procedures, the potential difference between E_{pa} and E_{pc} is wider. The peak current in a reversible framework for the forward voltage sweep is given by the Randles-Sevcik equation,

$$i_{pc} = 2.69 \times 10^8\, n^{3/2}\, A\, D^{1/2} v^{1/2} C$$

where, i_{pc} = peak current [A]; n = # electrons, A = electrode area [m^2]; D = diffusion coefficient [m^2/s]; C = concentration [mol/L] and v = scan rate [V/s].

Therefore, i_{pc} is proportional to the square root of v and the concentration of the species. An example of the CV curve on bare Au electrode in 5mM ferro-/ferricyanide having three electrode setup is plotted in Figure 2.7.

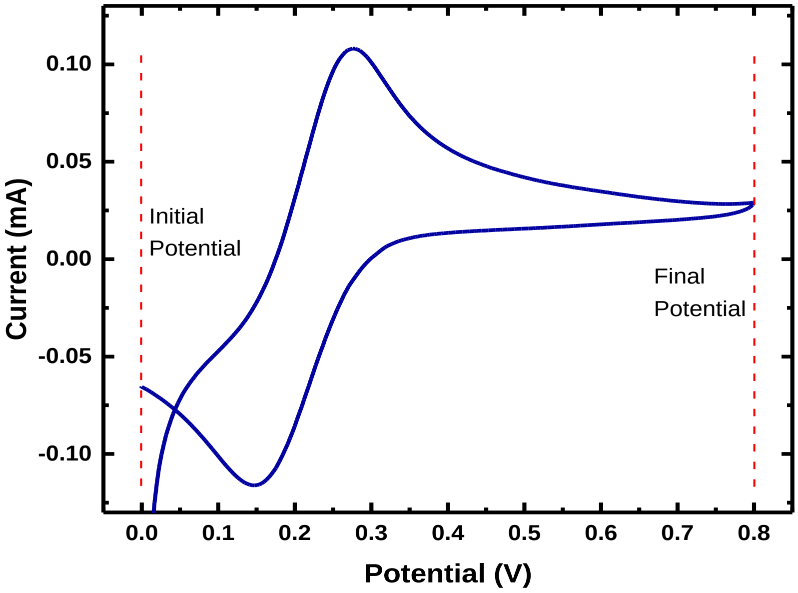

Figure 2.7: Example of Cyclic Voltammetry Curve for Au electrode in 5mM FerroFerri Cyanide solution

2.7.2 ELECTROCHEMICAL IMPEDANCE SPECTROSCOPY

Electrochemical Impedance Spectroscopy (EIS) has recently become popular in sensing and surface characterization because of its unprecedented applications. It works with electrical properties of materials and their interfaces with surface-adjusted electrodes [103]. This methodology has been extensively used in the study of electrochemistry [104], biomedical applications [105], material science [106] to name a few. EIS has been used extensively to study the properties of milk [107], various types of meat [108], quality testing in animal skin [109], sax reed review [110], detection of contaminated seafood with marine biotoxin [111], food endo-toxins [112]–[115], and quality monitoring of beverages [116].

EIS techniques can also help examine the ionic conductivity in electrolytes. The resistivity of materials including ionic glasses, polymers, blended salts, and nonstoichiometric ionic salts can be characterized using EIS whenever ionic transport is present. Moreover, the EIS is also a useful tool for studying energy storage, rechargeable batteries, and consumption of such energy. Another common usage of EIS applies to studying dielectric materials [117]. Therefore, EIS is a powerful tool in functional polymer-based biosensor applications.

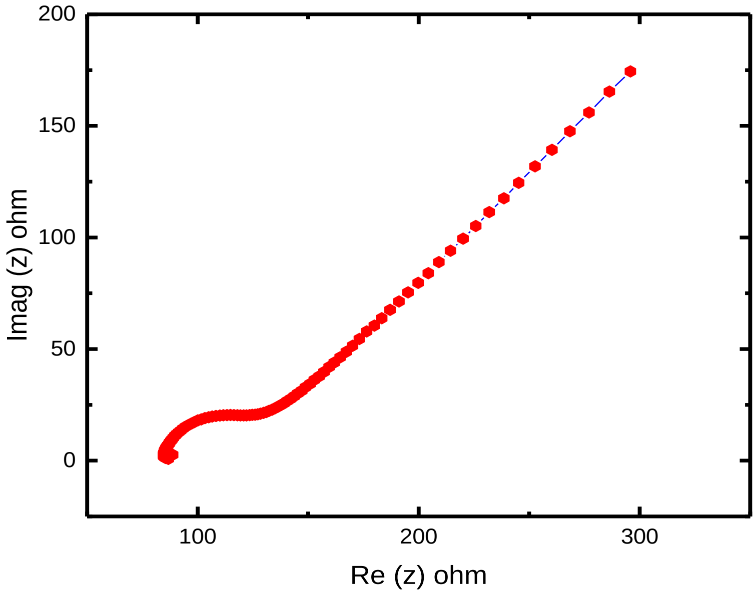

Figure 2.8: Example of Electrochemical Impedance Spectroscopy Nyquist Curve for Au electrode in 5mM FerroFerri Cyanide solution

In the Nyquist plot, shown in Figure 2.9, the impedance can be represented as a vector of length $|Z|$. The angle between this vector and the x-axis is ω. Low frequency data are on the right side of the plot and higher frequencies are on the left. This is generally true in most circuits for *EIS* data where impedance usually decreases as the frequency rises.

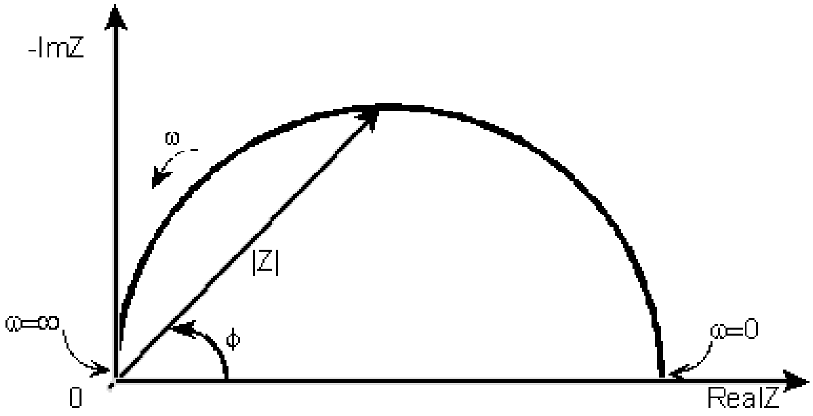

Figure 2.9: Example of Nyquist plot of an RC circuit

Figure 2.9 The semicircle is a characteristic plot of a single "time constant". The electrochemical impedance plots often comprise of several time constants. Typically, only a portion of one or more of their semicircles is seen. Another method to present the EIS data is using the Bode plot. The impedance is plotted with log frequency on the x-axis and both the absolute value of the impedance ($|Z| = Z_0$) and phase-shift on the y-axes. The Bode plot for the RC circuit is shown in figure 2.10. The Bode plot explicitly shows frequency information.

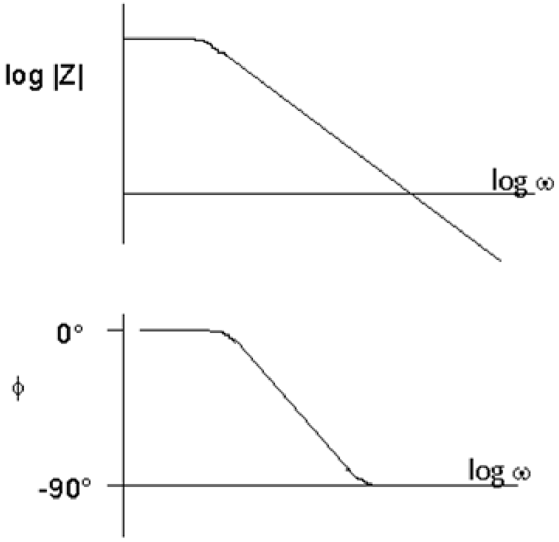

Figure 2.10: Example of Bode plot of an RC circuit

2.7.3 PHYSICAL ELECTROCHEMISTRY AND EQUIVALENT CIRCUIT ELEMENTS

EIS can be utilized to describe mass and interfacial properties of the electrochemical system. It is a highly precise and noninvasive technique. Electrochemical system can be modeled as a network of passive electrical circuit elements, called an equivalent circuit. The EIS response of an equivalent circuit can be calculated and compared to the actual EIS response of the electrochemical system. Randles and Ershler equivalent model are the commonly used circuit models for studying charge transfer in lithium ion batteries, bio sensors, ion selective systems and to examine the stability of films. It incorporates ohmic obstruction of the electrolyte arrangement, Warburg impedance (coming about because of the dispersion of ions from the mass electrolyte to the terminal interface), double layer capacitance and electron transfer resistance (that exists if a redox test is available in the electrolyte arrangement).

2.7.4 ELECTROLYTE RESISTANCE

Solution resistance is an important factor in the impedance of an electrochemical cell. A modern three electrode potentiostat compensates for the solution resistance between the counter and reference electrodes. However, any solution resistance between the reference electrode and the working electrode must be considered during modelling of the system. The resistance of an ionic solution depends on the ionic concentration, type of ions, temperature, and the geometry of the area in which current is flown. In a bounded area with area, A, and length, l, carrying a uniform current, the resistance can be defined as,

$$R = \rho \frac{l}{A}$$

where ρ is the solution resistivity. The reciprocal of ρ (κ) is more commonly used. κ is called the conductivity of the solution and its relationship with solution resistance termed as:

$$R = \frac{1}{\kappa}\frac{l}{A}$$

$$or\ \kappa = \frac{l}{RA}$$

Most electrochemical cells don't have uniform current dissemination through a positive electrolyte zone. The significant issue in figuring course of obstruction in this way concerns assurance of the present flow direction and the geometry of the electrolyte that conveys the current.

2.7.5 DOUBLE LAYER CAPACITANCE

Electrical double layer exists on the interface between a terminal and its encompassing electrolyte. This twofold layer is framed as ions from the solution adsorb onto the electrode surface. The charged electrode is separated from the charged ions by an insulating space, often on the order of angstroms. Charges separated by an insulator form a capacitor so a bare metal immersed in an electrolyte will behave like a capacitor.

2.7.6 POLARIZATION RESISTANCE

At whatever point the capability of an electrode is constrained far from its incentive at open circuit, that is alluded to as "polarizing" the cathode. At the point when an electrode is captivated, it can make current course through electrochemical responses that happen at the anode surface. The measure of current is constrained by the energy of the responses and the dissemination of reactants both towards and far from the cathode. In cells where an anode experiences uniform erosion at open circuit, the open circuit potential is constrained by the harmony between two distinctive electrochemical responses. One of the responses creates cathodic current and the different produces anodic current. The open circuit potential equilibrates at the potential where the cathodic and anodic flows are equivalent. It is alluded to as a blended potential. If the cathode is effectively consuming, the estimation of the current for both responses is known as the consumption current. Blended potential control likewise happens in cells where the anode isn't eroding. While this segment talks about erosion responses, change of the phrasing makes it pertinent in non-consumption cases just as found in the following area.

If there are two, simple, kinetically controlled reactions occurring, the potential of the cell is related to the current by the following equation.

$$I = I_{corr}\left(e^{\frac{2.303(E - E_{oc})}{\beta_a}} - e^{\frac{-2.303(E - E_{oc})}{\beta_c}}\right)$$

where,

I = the measured cell current in amps,

I_{corr} = the corrosion current in amps,

E_{oc} = the open circuit potential in volts,

β_a = the anodic Beta coefficient in volts/decade,

β_c = the cathodic Beta coefficient in volts/decade.

Small signal modelling approach can change the expression as

$$I_{corr} = \frac{\beta_a \beta_c}{2.303\,(\beta_a + \beta_c)}\left(\frac{1}{R_p}\right)$$

Where R_p, the polarization resistance. the polarization resistance behaves like a resistor.

2.7.7 CHARGE TRANSFER RESISTANCE

Resistance in this example is formed by a single, kinetically controlled electrochemical reaction. In this case a mixed potential is absent, but rather a single reaction at equilibrium happens. Consider the following reversible reaction

$$\text{Red} \Leftrightarrow \text{Ox} + ne^-$$

This charge transfer reaction has a certain speed. The speed depends on the kind of reaction, the temperature, the concentration of the reaction products and the potential. The general relation between the potential and the current (which is directly related with the number of electrons and so the charge transfer via Faradays law) is:

$$i = i_0 \left(\frac{C_0}{C_0^*} exp^{\left(\frac{\alpha nF\eta}{RT}\right)} - \left(\frac{C_R}{C_R^*} exp^{\left(\frac{-(1-\alpha)nF\eta}{RT}\right)}\right)\right)$$

with,

i_0 = exchange current density

C_0 = concentration of oxidant at the electrode surface

C_0* = concentration of oxidant in the bulk

C_R = concentration of reductant at the electrode surface

C_R* = concentration of reductant in the bulk

η = overpotential ($E_{app} - E_{oc}$)

F = Faradays constant

T = temperature

R = gas constant

α = reaction order

n = number of electrons involved

When the concentration in the bulk is the same as at the electrode surface, $C_O=C_O*$ and $C_R=C_R*$. This simplifies the previous equation into:

$$i = i_0 \left(exp^{\left(\alpha \frac{nF}{RT}\eta\right)} - \left(exp^{\left(-(1-\alpha)\frac{nF}{RT}\eta\right)}\right)\right)$$

This equation is called the Butler-Volmer equation. It is applicable when the polarization depends only on the charge-transfer kinetics. When the overpotential, η, is very small and the electrochemical system is at equilibrium, the expression for the charge-transfer resistance changes to:

$$R_{ct} = \frac{RT}{nFi_0}$$

From this equation the exchange current density can be calculated when R_{ct} is known.

2.7.8 DIFFUSION

Diffusion additionally can make an impedance called a Warburg impedance. The impedance relies upon the recurrence of the potential annoyance. At high frequencies, the Warburg impedance is little since diffusing reactants don't need to move far. At low frequencies, the reactants need to diffuse more distant, expanding the Warburg-impedance. Warburg impedance is the diffusional impedance for the diffusion layer of infinite thickness which is characterized for the macroelectrode.

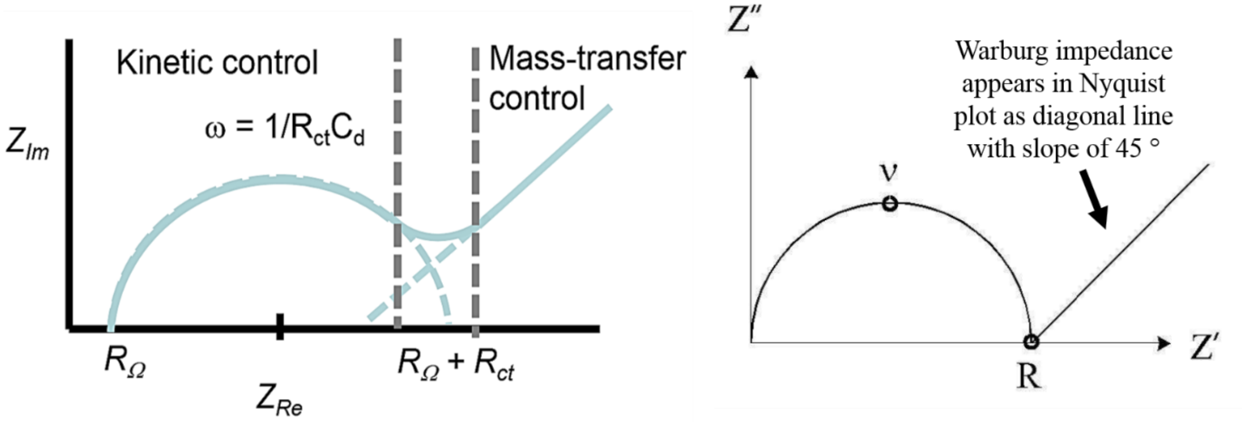

Figure 2.11: Diffusion mechanism in an EIS plot

The equation for the "infinite" Warburg impedance is:

$$Z_w = \sigma\,(\omega)^{-\frac{1}{2}}\,(1 - j)$$

On a Nyquist Plot (Fig 2.11) the Warburg impedance appears as a diagonal line with a slope of 45°. On a Bode Plot, the Warburg impedance exhibits a phase shift of 45°.

σ is the Warburg coefficient defined as:

$$\sigma = \frac{RT}{n^2F^2A\sqrt{2}}\,\left(\frac{1}{C_0^*\sqrt{D_0}} + \frac{1}{C_R^*\sqrt{D_R}}\right)$$

In which,

ω = radial frequency

D_0 = diffusion coefficient of the oxidant

D_R = diffusion coefficient of the reductant

A = surface area of the electrode

n = number of electrons involved

C_0* = concentration of oxidant in the bulk

C_R* = concentration of reductant in the bulk

This type of the Warburg impedance is just substantial if the dispersion layer has an endless thickness. Warburg impedance can be calculated by following expression:

$$Z_0 = \sigma\, (\omega)^{-\frac{1}{2}}\, (1 - j) \tanh(\delta \left(\frac{j\omega}{D}\right)^{\frac{1}{2}})$$

with,

δ = Nernst diffusion layer thickness

D = some average value of the diffusion coefficients of the diffusing species

This more general equation is called the finite Warburg. For high frequencies where ω→∞, or for an infinite thickness of the diffusion layer where δ→∞, tanh(δ(jω/D)½)→1

2.7.9 CONSTANT PHASE ELEMENT

Capacitors in EIS experiments often do not behave ideally. Instead, they act like a constant phase element (CPE) as defined below.

The impedance of a capacitor can be expressed as:

$$Z_{CPE} = \frac{1}{(j\omega)^{\alpha}\, Y_0}$$

where,

Y0 = The admittance

α = An exponent equaling 1 for a capacitor

For a constant phase element, the type α is less than 1. The double layer capacitor on genuine cells frequently carries on like a CPE, not a capacitor. While a few speculations (surface harshness, defective capacitor, non-uniform current dispersion, and so on.) have been proposed to represent the non-perfect conduct of the twofold layer, it is most likely best to treat α as an exact steady with no genuine physical premise.

2.7.10 COMMON EQUIVALENT CIRCUIT MODELS

The elements used in most of the equivalent circuits are presented in Table 2.2. Both the admittance and impedance expressions are given for each circuit element.

Equivalent circuit element	Impedance	Admittance
R	R	
C	$\frac{1}{j\omega C}$	$j\omega C$
L	$j\omega L$	$\frac{1}{j\omega L}$
W (Infinite Warburg)	$\frac{1}{Y_0\sqrt{j\omega}}$	$Y_0\sqrt{j\omega}$
O (Finite Warburg)	$\frac{tanh(B\sqrt{j\omega})}{Y_0\sqrt{j\omega}}$	$Y_0\sqrt{j\omega}Coth(B\sqrt{j\omega})$
Q (Constant Phase Element)	$\frac{1}{Y_0 j\omega^{\alpha}}$	$Y_0 j\omega^{\alpha}$

Table 2.2: Equivalent Circuit parameter

The EIS software uses dependable variables like R, C, L, Y_0, B and α as fit parameters.

2.7.11 SIMPLIFIED RANDLES CELL

The Simplified Randles cell is one of most regular cell models. It incorporates a solution resistance, a double layer capacitor and a charge transfer (or polarization resistance). The double-layer capacitance is in parallel with the charge-move obstruction. Notwithstanding being a helpful model, the Simplified Randles Cell is the beginning stage for other increasingly complex models. The equal circuit for a Simplified Randles Cell is appeared in Figure 2.12

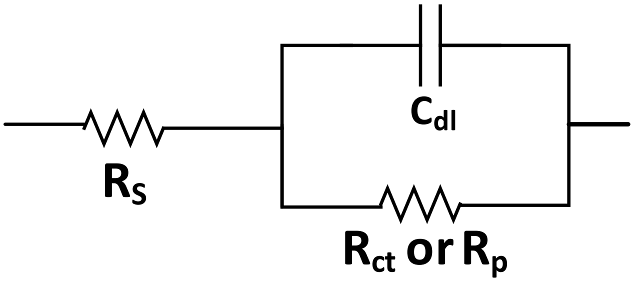

Figure 2.12: Simplest representation of Randles circuit

The Nyquist Plot of a Simplified Randles cell is always a semicircle. The solution resistance can be found by analyzing the real axis value at the high frequency intercept. This is the intercept near the origin of the plot. The real axis value at the other (low frequency) intercept is the sum of the polarization resistance and the solution resistance. Consider a cell where semi-limitless dispersion is the rate deciding advance, with an arrangement opposition as the main other cell impedance. Adding a double layer capacitance and a charge transfer impedance, we get the equivalent circuit in Figure 2.13. This circuit models a cell where polarization is due to a combination of kinetic and diffusion processes.

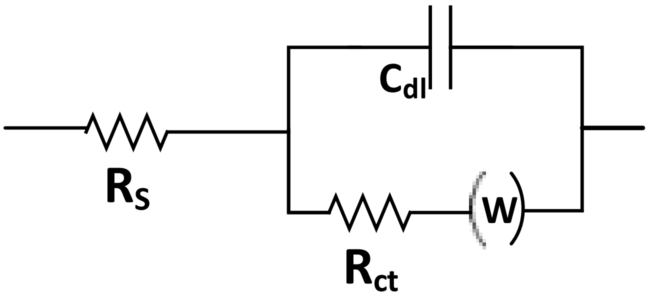

Figure 2.13: Modified Randles circuit for mixed kinetic and diffusion-controlled system

With the presentation of a constant phase element (CPE) as a trade for the limit in EIS estimations, most of the experimental raw data could be fitted by economically accessible software (Gamry, Scribner, Solartron, and so on.). Much better fit outcomes were gotten with CPE in correlation with the fit outcomes acquired by utilizing unadulterated limit, spoken to by parallel plate condenser. Considering that the CPE characterizes inhomogeneity of the surface in the electrochemical EIS trials and inhomogeneity of the charge dissemination in strong state EIS estimations, it is sensible to expect that better fit for genuine frameworks is acquired by utilizing CPE. Figure 2.14 shows the use of constant phase element and infinite Warburg element.

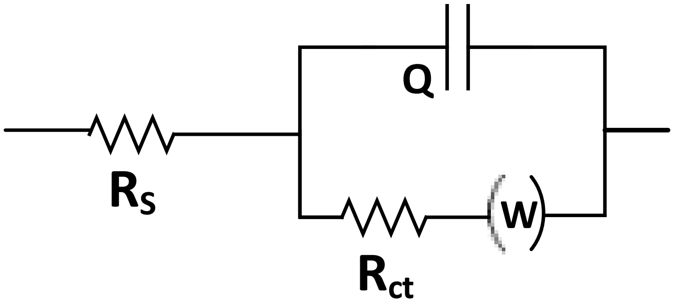

Figure 2.14: Randles circuit where Pure capacitance is replaced with constant phase element in a mixed kinetic and diffusion-controlled system

CHAPTER 3: SYNTHESIS OF A SINGLE-CHAIN TEMPLATED POLYMER

3.1. OVERVIEW

This chapter discusses name of chemicals and reagents used for the thesis and types of electrodes used for electrochemical measurements. The theory of RAFT polymerization is briefly discussed. The synthesis of homo PNIPAM and other functional copolymer are discussed along with the purification process throughout the chapter.

3.2 REAGENTS

Reagents are recorded by their sources. The following rundown of materials and synthetic substances were utilized during different experiment:

Sigma Aldrich (St. Louis, MO, USA)

1. Methacrylic acid 99% purity (**MAA**). was vacuum distilled, then passed through columns of basic alumina and inhibitor remover to remove inhibitor.
2. 4-Vinylpryidine 95% purity (**4VP**). was vacuum distilled, then passed thought a column of basic alumina and a column of inhibitor remover to remove inhibitor.
3. 2-(Dodecylthiocarbonothioylthio)2-methylpropanoic acid 97% purity (**DDMAT**). Used as received.
4. 2,2 Azobisisobutyronitrile 98% (**AIBN**). Used as received
5. 3-Nitrophenol 99% purity (3NP). Used as received
6. 4-Nitrophenol 99% purity (4NP). Used as received
7. 1,4-dioxane, 99.8% anhydrous. Used as received
8. Ethanol, ACS Grade.
9. Acetone, ACS Grade.

Tokyo Chemical Industry (TCI)

N-isopropyl acrylamide 99% purity (**NIPAM**). Recrystallized from hexane (3 times) to remove inhibitor.

3.3 ELECTRODES

The working electrode (Fig 3.1 (A)) used for this thesis is BASI MF-2114 [118] Au electrode. The reference electrode (Fig 3.2 (C)) used is BASI MF-2052 [119] Ag/AgCl (3M NaCl) electrode. The counter electrode (Fig 3.2 (B)) used for the electrochemistry purpose is BASI MW-1033 [120] Platinum coil auxiliary electrode.

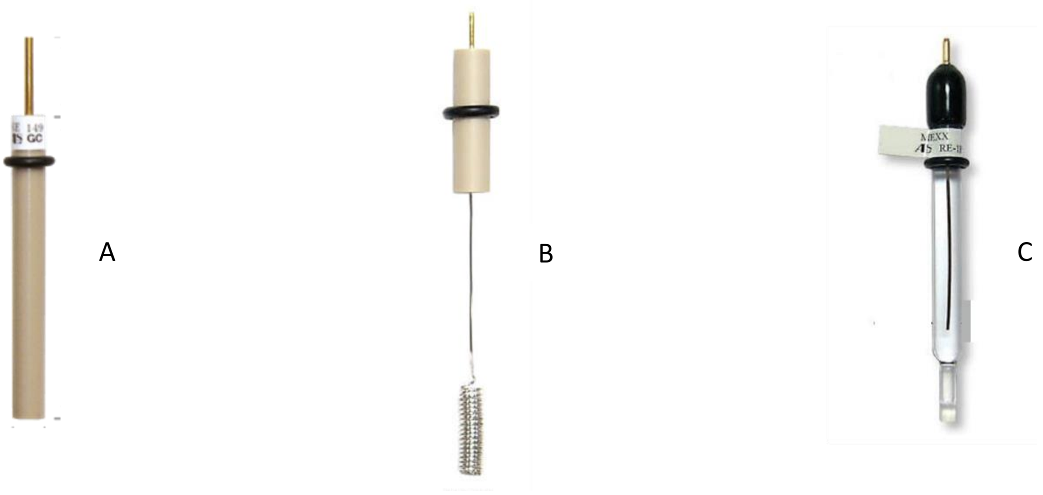

Figure 3.1: A) Working Electrode B)Counter Electrode C) Reference Electrode

3.4 RAFT POLYMERIZATION

The revelation of reversible-deactivation radical polymerization (RDRP) has opened countless opportunities to create a variety of high-fidelity polymers with an abundance of functionality and architecture. RDRP has revolutionized the way polymers were synthesized during recent decades, laying the foundation for the blend of complex macromolecules and enabling the production of polymers that were previously not achievable. The arrival of RDRP began with the development of atom transfer radical polymerization (ATRP) [121] along with reversible addition fragmentation chain transfer (RAFT) polymerization [122]–[125], which has revitalized the free radical polymerization technique for the creation of functional polymers. The basic principle behind RDRP process is based on the existence of a highly controlled and sustained radicals that continue to propagate throughout the polymerization via a reversible initiation and deactivation balance. In nitroxide mediated polymerization (NMP) and atom transfer radical polymerization (ATRP), this balance is established through either nitroxide capping (NMP) or a redox process with a metal halide salt (ATRP) in which the equilibrium strongly favors the dormant species. This mechanism is known as reversible termination of the propagating chain (Figure 3.1) [126].

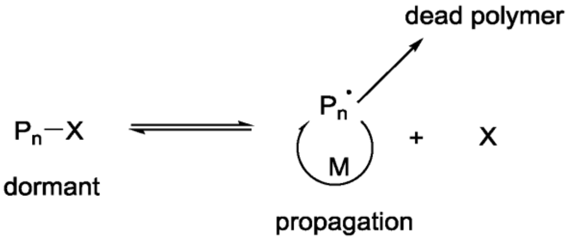

Figure 3.2 : Reversible-deactivation radical polymerization by reversible termination [126]

Radical formation only occurs when dormant species are activated, at a time when the concentration of the propagating radicals remains low. Due to the irreversible termination, formation of prematurely terminated polymers is low in concentration. On the other hand, RAFT follows a degenerative chain transfer process, where the propagating species equilibrate with dormant species (figure 3.2). RAFT process leads to better control over NMP and ATRP in terms of polymer integrity and homogeneity.

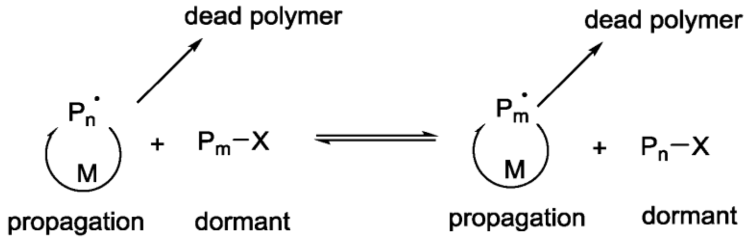

Figure 3.3 : Reversible-deactivation radical polymerization by degenerative chain transfer [126]

RAFT regularly uses a thiocarbonylthio-containing chain transfer agent (CTA). Since there is no net change in the number of free radicals during the activation−deactivation procedure, an external initiator is required with the initiation proceeding like a normal radical polymerization. The mechanism of RAFT polymerization is presented in Figure 3.4 [127].

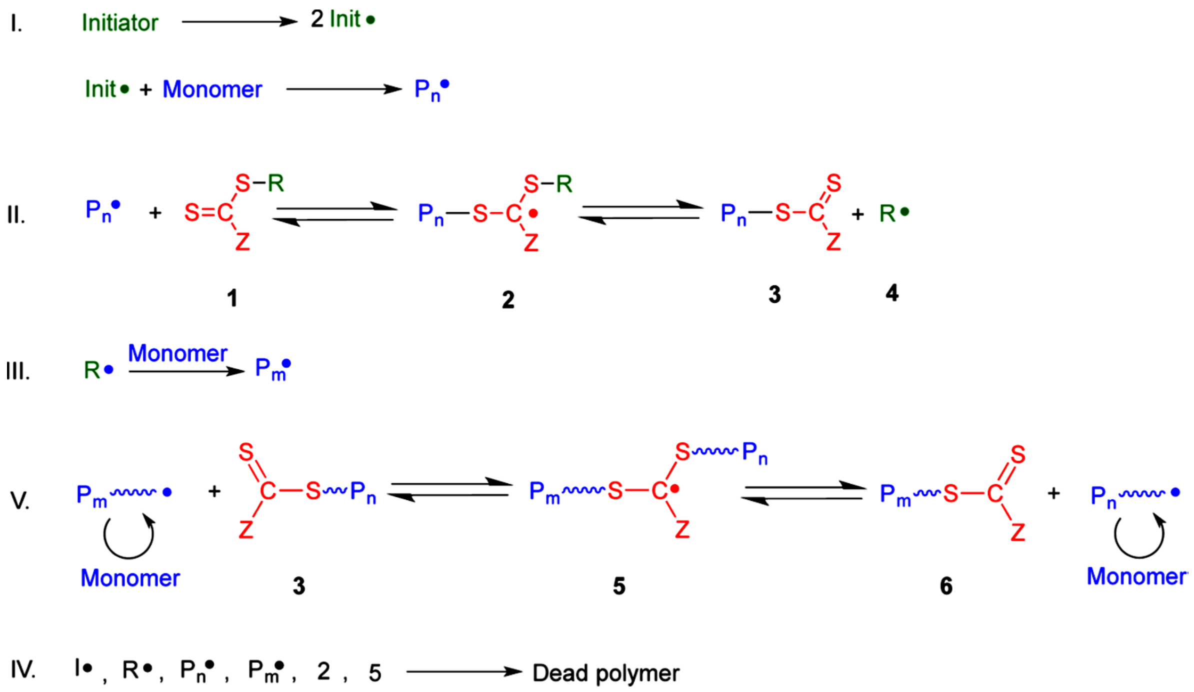

Figure 3.4: Reversible addition−fragmentation chain transfer (RAFT) polymerization mechanism

After initiation, the propagating radical (Pn•) adds to the thiocarbonylthio compound (1) to form the radical intermediate (2), which subsequently fragments to give another thiocarbonylthio group (3) and a new radical (R•) (4). The radical (R•) may then react with the newly formed thiocarbonyl group or reinitiate polymerization by reacting with monomer to form a new propagating radical (Pm•). After the initially added CTA is consumed (i.e., completion of the "initialization period"),[128] the "main equilibrium" of activation−deactivation is established by degenerative chain transfer between propagating (Pm or Pn) and dormant (3/6) chains.

RAFT polymerization is a living radical polymerization strategy that can be utilized to synthesize polymers of various structures including homopolymers, triblock, and star-shaped polymers with predetermined atomic weights [123]. Several types of RAFT chain transfer agents (CTAs) are commercially available, including dithiobenzoates, trithiocarbonates, and dithiocarbamates [129]. In this thesis, RAFT polymerizations of Poly(N-isopropylacrylamide) were performed with the traditional azo-initiator 2,2'-azo-bis-isobutyrylnitrile (AIBN) as a radical initiator and 2-(((Dodecylthio)carbonothioyl)thio)-2-methylpropanoic acid (DDMAT) as the CTA. The polymerization process is shown in Figure 3.5.

This method utilizes the pressure dependence of gas solubility in liquid. The pressure of the gas inside the Schlenk flask is decreased during the pumping process. A new liquid- gas phase equilibrium was established when thaw process ran. As a result, the dissolved gas was released from the liquid as bubbles.

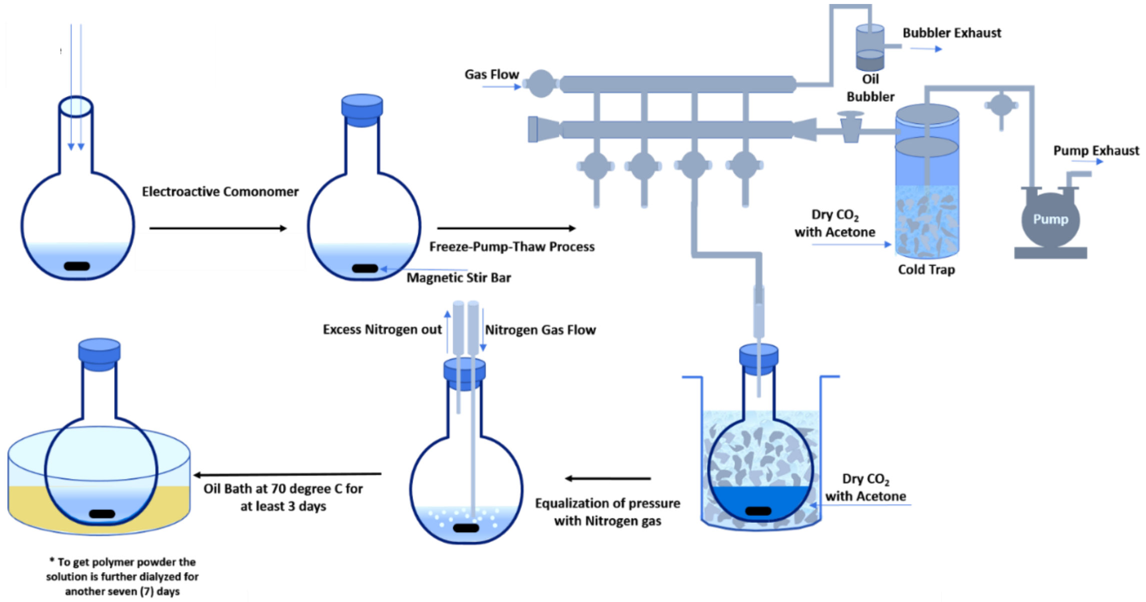

Figure 3.5: Freeze Pump Thaw process to synthesis of PNIPAM

Main Advantages of RAFT polymerization over traditional polymerization include: Simple to implementation, low cost, compatibility with a wide range of monomers, Narrow molecular weight distribution (low dispersity)[130], intricate control over polymer architecture & end group functionality.

3.4 POLY (NIPAM)

Poly(N-isopropylacrylamide) (PNIPAM) is a standout amongst the most examined temperature-responsive polymers and shows temperature dependence phase change in fluid arrangements at its lower critical solution temperature (LCST) of 32° C [107]. Hydrophobicity/hydrophilicity of hydrated PNIPAM chain can be controlled by temperature [108], [109]. The LCST and hydrophobicity/hydrophilicity of PNIPAM can be accurately controlled by the copolymer composition[110], [111]. In past investigations, PNIPAM has been functionalized with outside stimuli-responsivity to pH[112], ions[113],saccharides[114] and light[115] by copolymerization with functional monomers.

Poly(N-isopropylacrylamide) (PNIPAM) is a well-known stimuli-responsive polymer whose phase transitions when interacted with water. It transforms to a swollen hydrated polymer when the solution temperature is below 32°C and becomes a dehydrated and collapsed (or shrunken) phase when the solution temperature is above 32°C. This transition temperature is known as the lower critical solution temperature (LCST). At temperatures below the LCST, the hydrogen bonding from the amide group is strong causing the poly(NIPAm) to dissolve in aqueous solution. In this phase, the polymer chain is in an extended random coil shape as illustrated in Figure 3.6

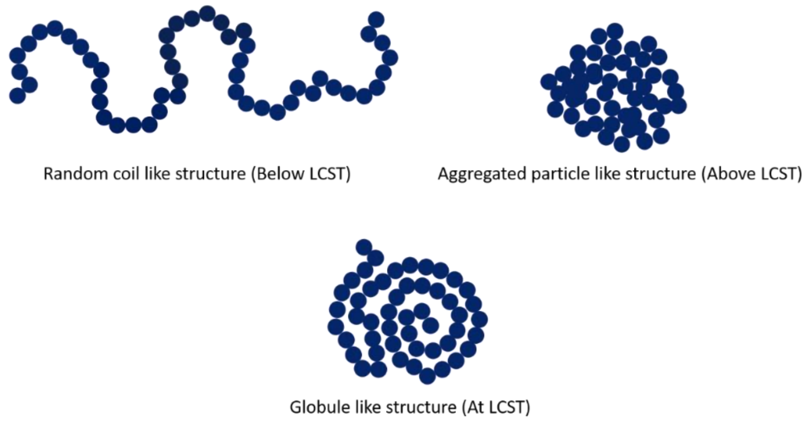
Random coil like structure (Below LCST)
Aggregated particle like structure (Above LCST)
Globule like structure (At LCST)

Figure 3.6: Phase transition behavior of Poly (NIPAM) chain at different temperature

For temperatures above the LCST, the hydrogen bonding between water molecules and the poly (NIPAM) chains is too weak to overcome the hydrophobic interactions within the aliphatic polymer backbone, isopropyl groups, and the water molecules. Therefore, the poly (NIPAM) chains form hydrophobic globules. Further increment in the temperature above the LCST causes the globules to become even more aggregated resulting in larger polymeric solid particles.

Beyond LCST, Critical temperature, Tc is portrayed by two characteristic parameters: the arrest temperature *Ta* and the concentration c_t beyond which the poly (NIPAM) collapses over time. Between Tc and Ta, the framework can develop by phase separation and collapse in time, while phase separation is arrested past Ta. Above Ta, phase space is divided by *ct*. Beneath ct the attributes of the arrested states, mesoglobules and aggregates, are elements of the PNIPAM concentration and the temperature history of the sample or more exactly the time spent at the coarsening conditions among Tc and Ta. Paradoxically, above ct the phenomenology of contracting gels, which are gatherings of completely crumpled microgels, is autonomous of these parameters [131]. Rather, the level of contracting relies upon the profundity of the temperature extinguish characterized as $\Delta \mathrm{T} = \mathrm{T} - \mathrm{Ta}$, a parameter that is immaterial for the captured states shaped underneath ct. The state dependency with variation of concentration and temperature depicted in figure 3.7. The general highlights of the phase behavior are not limited to the PNIPAM microgel framework yet in addition apply to linear PNIPAM. [132]–[137].

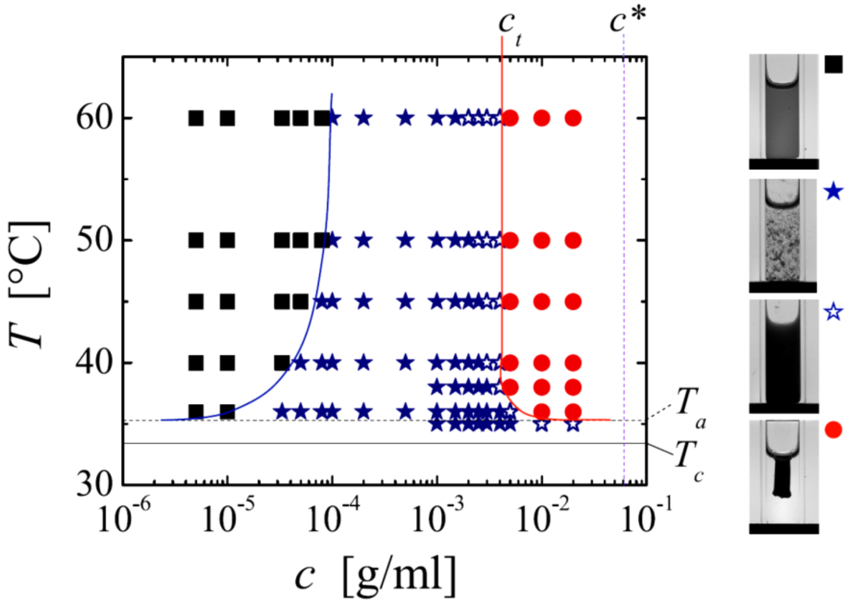

Figure 3.7: The state diagram depicting the arrested states of PNIPAM microgels, as obtained two hours after a quench beyond the lower critical solution temperature *Tc* [131].

Phase separation of PNIPAM is always arrested beyond *Ta*; with increasing concentration this leads to respectively stable mesoglobules (black squares), flocks (blue filled stars), space-filling aggregates (blue open stars) or shrinking gels (red circles) shown in figure 3.7. The blue line denotes the boundary between mesoglobules and flocculated states, as determined in dynamic light scattering experiments. The red line marks the onset to shrinking gels, as determined by visual inspection. The solid horizontal line indicates *Tc*, the dashed horizontal line indicates *Ta*. The dotted vertical line denotes the critical concentration *c** beyond which the PNIPAM microgels are in a glassy state at 30 °C. The images on the right are representative examples for each state and are taken at *T* = 45 °C; from top to bottom: *c* = 1·10−5 g/ml, 1·10−3 g/ml, 3·10−3 g/ml and 2·10−2 g/ml. The errors in concentration are within 3% Poly (NIPAM) will lose about 90% of its water volume when the temperature is raised above 32°C [131]

3.5 HOMOPOLYMER OF N-ISOPROPYLACRYLAMIDE

Primarily the polymer synthesized for this project was a free radical polymerization of nisopropylacrylamide (NIPAM), a homopolymer, for initial testing and baseline experiments for future comparison (Figure 3.8). Initially purified NIPAM (25 mmol) 2.825 grams added in a 50 mL round bottom flask with 25 mL of 1,4-dioxane, 2% (w/w) AIBN, and a stir bar 97. The monomer and initiator were dissolved and sealed with a rubber septum to ensure initial vacuum. Freeze-pumped-thaw process was applied to sealed flask for multiple cycles to get rid of all gas. After three cycles the flask was back filled with inert gas i.e.; nitrogen for at least five minutes. The flask was then placed into an oil bath at 70°C for 24 hours with constant stirring for polymerization process. This N-isopropylacrylamide homopolymer is required for initial testing and future comparison with templated polymers.

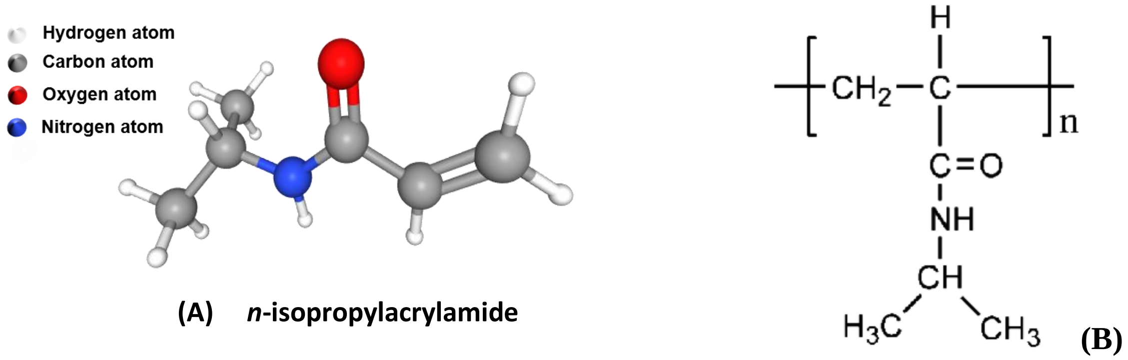

(A) ***n*-isopropylacrylamide**

$H_2C=CHCONHCH(CH_3)_2$

Figure 3.8: A) n-isopropylacrylamide B)Homopolymer of n-isopropylacrylamide

3.6 COPOLYMERIZATION OF TP AND TEMPLATE REMOVAL

For template sensing, 4 Nitrophenol (fig: 3.9(A)) and NMethylGlutamate (fig: 3.9(B)) were used during TP synthesis. 4-nitrophenol (4-NP) is a hazardous waste and a priority toxic pollutant identified by US Environmental Protection Agency (EPA). Glutamate is crucial for cell metabolism in the peripheral tissues and organs. Neurotransmitter like glutamate play a critical role in the nervous system. NMethylGlutamate acts like an analog of L-Glutamic acid.

Several monomers were needed to form a functional TP. In case of template sensing, both 4-vinylpyridine (4VP) and Methacrylic acid (MAA) work as recognition or functional monomers. MAA is hydrogen donor as well as acceptor, so it can form dimer during polymerization. This dimerization could enhance the effect of imprinting[138].

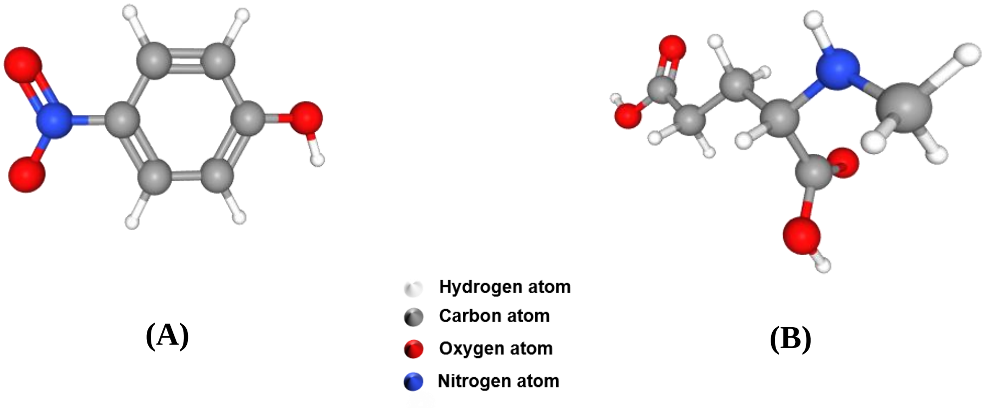

Figure 3.9: (A) 4-Nitrophenol (B) NMethylGlutamate

4VP and MAA forms a non-covalent acid-base crosslinking. Hydrogen bonds (fig: 3.10) between the MAA and 4VP hold the configuration of binding sites on the polymer chain[139], [140]. So, the memory of the target analyte was templated inside the polymer layer.

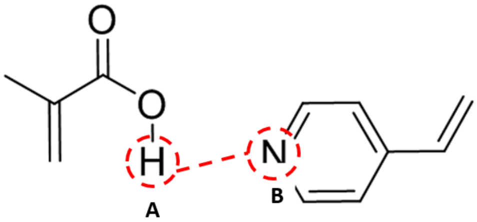

Figure 3.10: The hydrogen (A) in the carboxylic acid group in MAA can behave as a hydrogen bond donor, the nitrogen (B) in aromatic ring of 4-VP act as a hydrogen bond acceptor

To get optimum functional TP, 1,4-dioxane was used at varying volume to vary the concentration before initiation of polymerization. Hexane was added thus the polymer was precipitated out of the solution. The solubility of the monomer in hexane is higher than polymer. So, the unreacted monomer and most of template molecules were left in the hexane. The polymer was separated by centrifugation. It was observed that after 4 rounds of precipitation over 90% template molecules can be removed. Then, the MIPs were dissolved in a good solvent for the template molecules and dialyzed. The polymerized solution was placed in dialysis bag which had 10,000 to 12,000 molecular weight cut off (MWCO) dialysis membrane. The dialysis pack was put into a vessel that has more volume than the pack [141] The whole dialysis process typically kept running in between four weeks to six months to get fully synthesized polymer chain inside the dialysis bag. To get rid of unbound template the polymer solution was alternated in between acidic and basic condition at different temperature with varying duration. This strategy could be useful to determine the required polymer concentration in dialysis bag which affect the time and amount of solvent to remove most of the templates.

3.7 FREEZE DRYING TP SAMPLE

It’s important to have template removed purified TP. First newly synthesized TP is needed to run through equilibrium dialysis. MIP was first diluted in 0.1 M sodium hydroxide and methanol (V:V=30:70) mixture for 6 hours, then flowed by dialysis in pH 10 sodium hydroxide solution for 2 days and D.I. water for 1 day. After the removal process is done, the TP solution is flushed with deionized water and freeze dried with Labconco Freezone 2.5 (figure 3.11). Diminishing the pressure close to 0.130 Torr and with the temperature brought down to - 80°C, underneath waters triple point, takes into consideration the expulsion of water through sublimation, deserting a soft grayish powder of TP sample [142]. The whole freeze-drying process could help to determine the polymer concentration and used to know theoretical bound template molecule to the TP structure.

Figure 3.11: Labconco Freezone 2.5 Lyophilization unit used for water removal in combination with an aluminum tower [143]

CHAPTER 4: POLYMER CHARACTERIZATION

After polymer synthesis, the lyophilized templated polymer powders were analyzed with Fourier Transform Infrared Spectroscopy (FTIR), Nuclear magnetic resonance (NMR) and X-ray photoelectron spectroscopy (XPS).

4.1 FOURIER TRANSFORM INFRARED SPECTROSCOPY (FTIR)

FTIR offers quantitative and subjective investigation for natural and inorganic samples. Fourier Transform Infrared Spectroscopy (FTIR) distinguishes chemical bonds in an atom by delivering an infrared absorption range. The spectra produce a profile of the sample, a unique sub-molecular signature that can be utilized to characterize the molecular composition of the synthesized polymer powder.

The samples were tested with Thermo Nicolet iS10 FT-IR, Windows XP-controlled instrument designed for easy operation using the OMNIC 8 software. The resolution of the spectrometer is 0.4 cm^{-1}, and the spectral range is 7800 to 350 cm. The sample chamber and optics are purged with air with a dew point of 95° F.

Figure 4.1: Thermo Nicolet iS10 FT-IR

4.1.1 PNIPAM-MAA-4VP FTIR

Figure 4.2 shows a random templated polymer chain with functional groups. MAA and 4VP form acid base crosslink throughout the polymer chain. 4VP works as a recognition monomer for the template, which form hydrogen bonding and/or π- π interaction with the template molecule. The Figure 4.2 is a random illustration of the synthesized polymer chain after template removal. Its been assumed that MAA and 4VP are present side by side in the figure but in actual sample PNIPAM can be present in between them. RAFT agent DDMAT provides the R and Z group which are kind of head and tail structure for the polymer chain. Reducing agent like TCEP promotes thiolate bonding to gold by breaking the Z group (C=S bond).

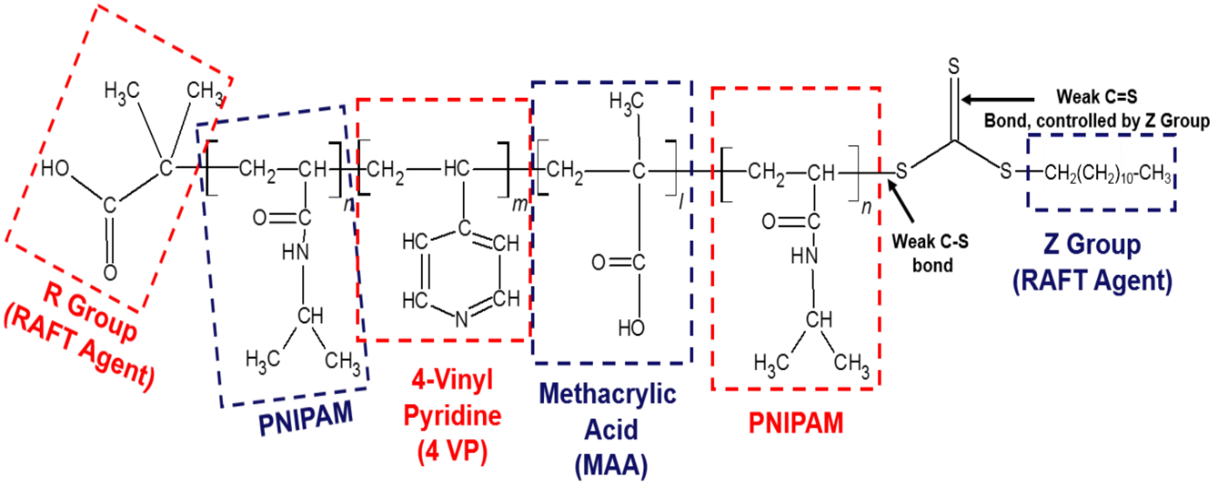

Figure 4.2: PNIPAM chain with functional monomers

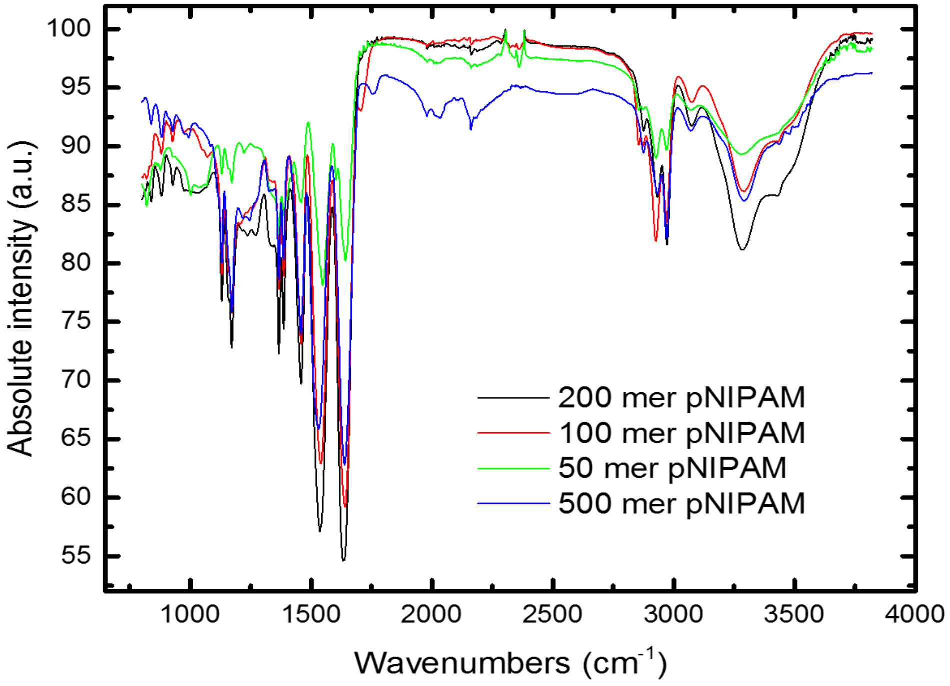

Figure 4.3: FTIR spectra for various chain length of homo PNIPAM

The peaks identified from the FTIR spectra shown in Figure 4.3 which plots various chain length of templated polymer are tabulated in Table 4.1 which shows the corresponding vibrational origins and the functional groups.

Functional Group	**Wavenumbers (cm^{-1})**	**Vibration origin / Functional group for peaks**
PNIPAM	1370,1390	isopropyl group vibration / symmetric doublet with medium intensity is for isopropyl group
	1130	Asymmetric C-N-C is stretching from the secondary amine. [144], [145]
	1462	C–H bending (scissoring) (in CH_3 groups) [144], [146]
	1638	Amide I due to stretching vibration of C=O group
	1553	Amide II (C-N stretching)

	3284	N-H stretch indicates hydrogen bond length ~2.85Å [144], [146]
DDMAT	833 to 930	Symmetric stretching due to C=S in thiocarbonyl linkage and mixed vibration from -N-C=S bands respectively [145], [147], [148]
	1280	ϑ(C-O) vibrations from carboxylic acid (R group)
	1170	$(-C(CH_3)_2-)$ skeletal vibration due to DDMAT (R group)
	1070	ϑ(C=S) stretching vibrations [149]

Table 4.1: PNIPAM FTIR spectra

4.1.2 4-NITROPHENOL (4NP) TP FTIR

Figure 4.4 shows the FTIR spectra for different chain length of 4NP templated polymer powder. Both chain length have signature similarities in FTIR spectra.

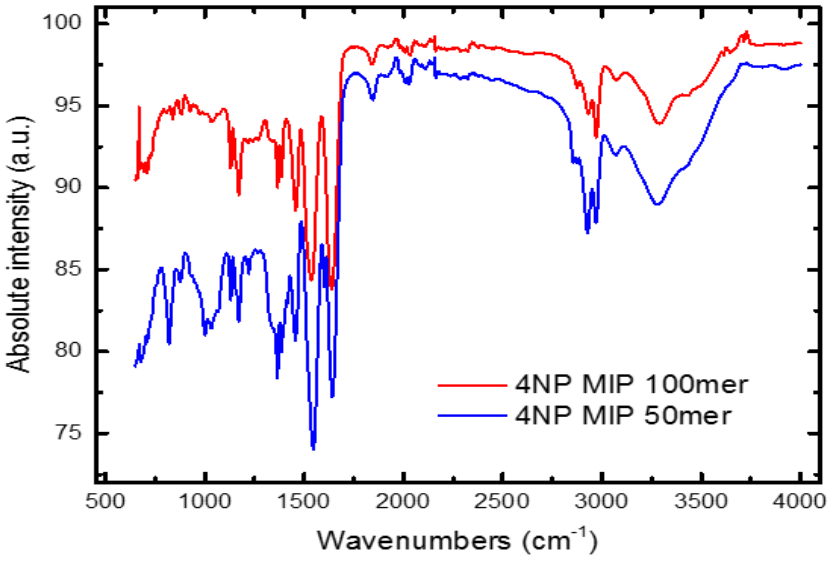

Figure 4.4: FTIR Spectra for 4NP TP

Functional Group/Template	**Wavenumbers (cm^{-1})**	**Vibration origin / Functional group for peaks**
PNIPAM	1370,1390	isopropyl group vibration / symmetric doublet with medium intensity is for isopropyl group
	1130	Asymmetric C-N-C is stretching from the secondary amine.
	1462	C–H bending (scissoring) (in CH_3 groups)
	1638	Amide I due to stretching vibration of C=O group
	1553	Amide II (C-N stretching)
	3284	N-H stretch indicates hydrogen bond length ~2.85Å
MAA	1711	Carbonyl (C=O) group stretch
4VP	1031	C-H in and out of plane bending
DDMAT	833 to 930	Symmetric stretching due to C=S in thiocarbonyl linkage and mixed vibration from -N-C=S bands respectively
	1280	ϑ(C-O) vibrations from carboxylic acid (R group)
	1170	(-C(CH_3)$_2$-) skeletal vibration due to DDMAT (R group)
	1070	ϑ(C=S) stretching vibrations
4-NP	1334	-NO_2 aromatic stretches from 4-NP
	1625	Hydrogen bonding between carbonyl group of functional co polymer and hydroxyl group of 4-NP

Table 4.2: Functional Group with 4NP templated PNIPAM FTIR spectra

The peaks at 1334 cm^{-1} and 1625 cm^{-1} signature for NO_2 aromatic stretches from 4-NP and hydrogen bonding between carbonyl group of the functional copolymer and the hydroxyl group of 4-NP respectively, are present in the pNIPAM-based polymer templated with 4-NP.

4.1.3 N METHYL GLUTAMATE TP FTIR

Figure 4.5 shows the FTIR spectra of purified N-methyl-glutamate templated polymer powder and Figure 4.6 verifies the purification or template removal procedural success.

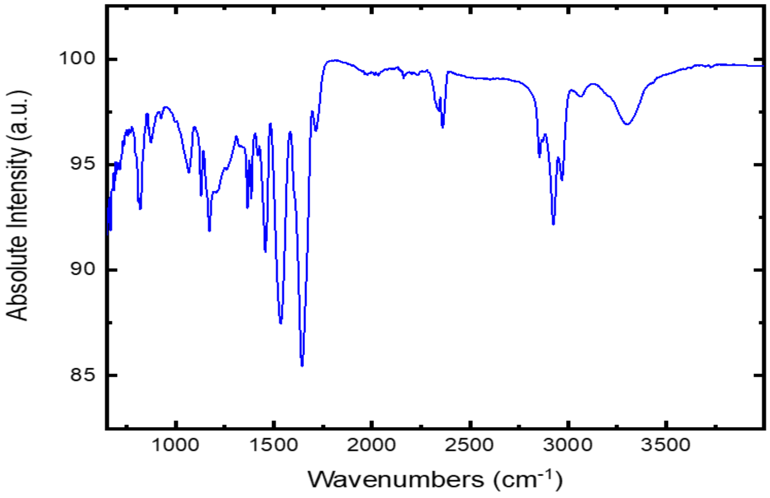

Figure 4.5: FTIR for N Methyl Glutamate removed TP

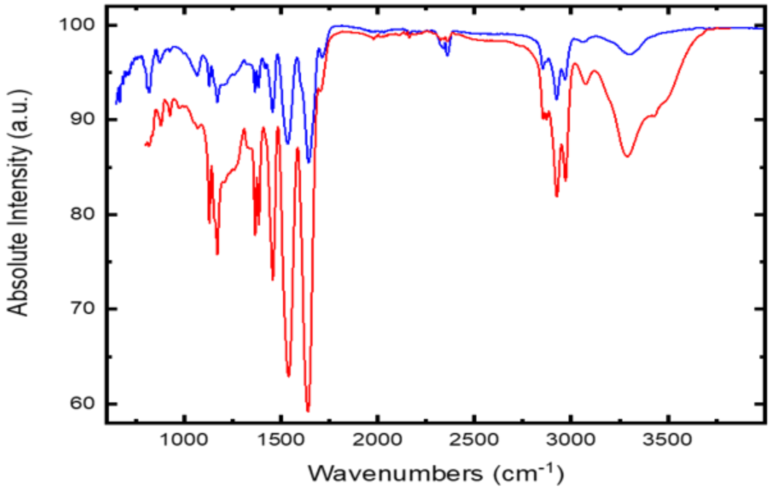

Figure 4.6: FTIR plots between N-Methyl-Glutamate removed TP and 100 mer PNIPAM NIP

In Figure 4.6, 100-mer NIP (red spectra) and N-Methyl-Glutamate removed TP (blue spectra) after template removal show similar kind of spectra in FTIR that confirms the template is removed from the polymer cavity.

Table 4.3 gives the list of the functional groups found in glutamate template removed polymer powder.

Functional Group/Template	Wavenumbers (cm^{-1})	Vibration origin / Functional group for peaks
PNIPAM	1370,1390	isopropyl group vibration / symmetric doublet with medium intensity is for isopropyl group
	1130	Asymmetric C-N-C is stretching from the secondary amine.
	1462	C–H bending (scissoring) (in CH_3 groups)
	1638	Amide I due to stretching vibration of C=O group
	1553	Amide II (C-N stretching)
	3284	N-H stretch indicates hydrogen bond length ~2.85Å
MAA	1711	Carbonyl (C=O) group stretch
4VP	1031	C-H in and out of plane bending
DDMAT	833 to 930	Symmetric stretching due to C=S in thiocarbonyl linkage and mixed vibration from -N-C=S bands respectively
	1280	ϑ(C-O) vibrations from carboxylic acid (R group)
	1170	(-$C(CH_3)_2$-) skeletal vibration due to DDMAT (R group)
	1070	ϑ(C=S) stretching vibrations

Table 4.3: Functional Group with N Methyl Glutamate removed PNIPAM FTIR spectra

4.2 NUCLEAR MAGNETIC RESONANCE (NMR) SPECTROSCOPY

Nuclear Magnetic Resonance (NMR) spectroscopy is an analytical chemistry technique utilized in quality control and research for characterizing the substance and composition. For instance, NMR can quantitatively identify molecules from a mixture of compound. NMR can either be utilized to coordinate against existing spectra databases or to construe the fundamental structure for an unknown compound. Once the basic structure is known, the NMR can be used to determine molecular conformation in solution as well as studying physical properties at the molecular level such as conformational changes, phase changes, solubility, and diffusion.

A 5 mg lyophilized polymer powder is mixed properly with 700 µL $CDCl_3$. Then the solution is transferred to NMR glass tube for experiment. The NMR spectra in Figure 4.8 confirmed that all monomers present in the initial formulation of templated polymer showed signals in the NMR spectra, confirming that each types of monomers was incorporated into the polymer chain as can be seen in Figure 4.7

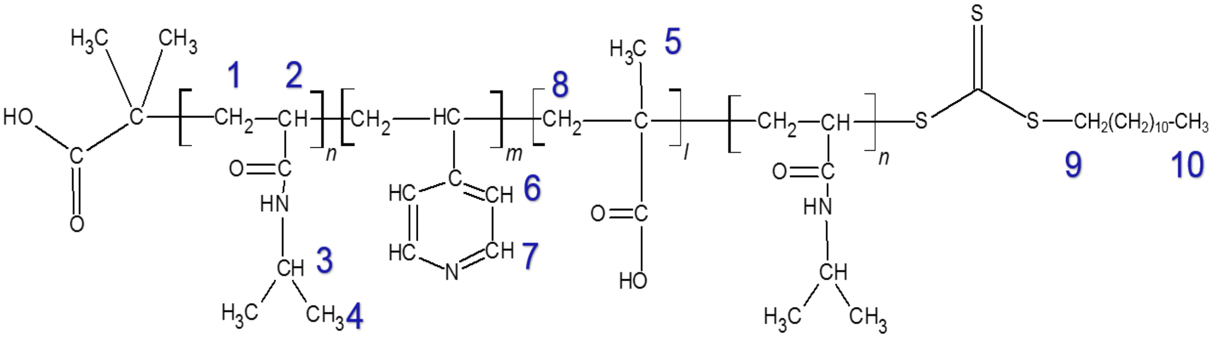

Figure 4.7: PNIPAM co MAA 4VP 100 mer Polymer chain

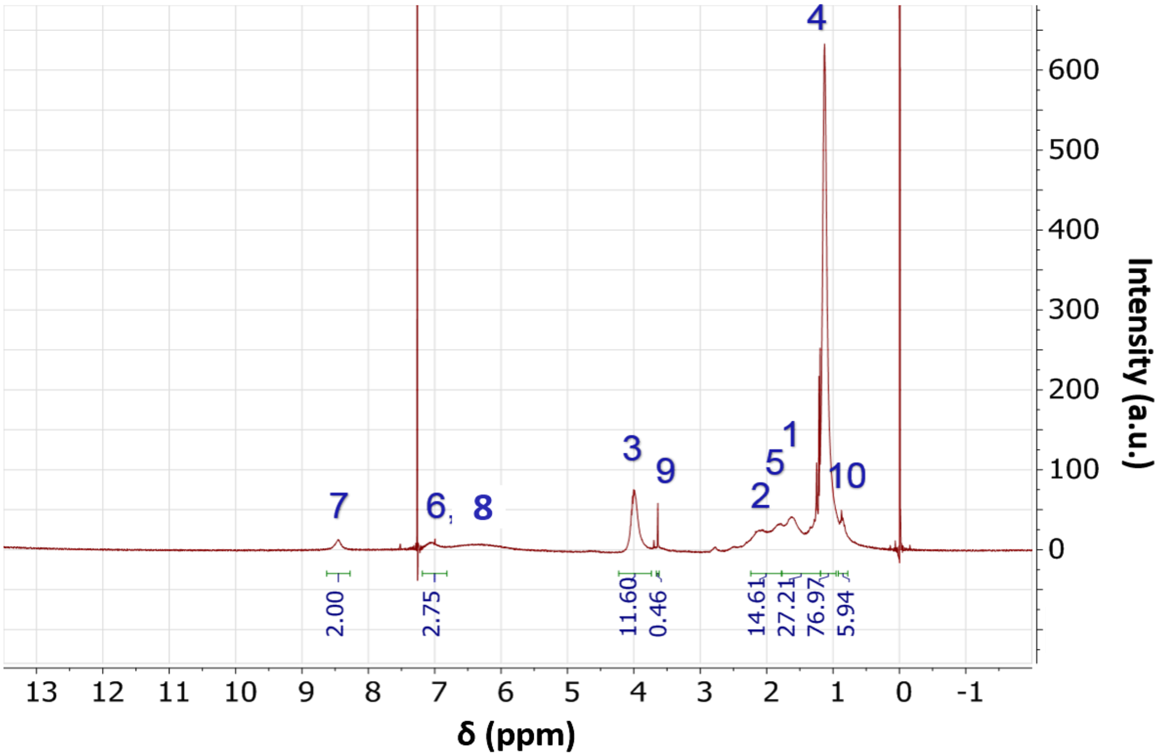

Figure 4.8: ^{1}H NMR (400MHz) spectra of PNIPAM co MAA 4VP 100 mer Polymer

The δ (1.6 ppm) at **peak 1** [-CH_2] and δ (2.1 ppm) at **peak 2** [-CH] can be attributed to the backbone of PNIPAM. The δ (4.0 ppm) at **peak 3** and δ (1.1 ppm) at **peak 4** are attributed to methine (isopropyl group) and methyl protons from NIPAM respectively [150]. The δ (1.95 ppm) at **peak 5** [-CH_3] [151] and δ (6.25 ppm) at **peak 8** [-CH_2] are attributed to MAA . The δ (7.1 ppm) at **peak 6** and δ (8.5 ppm) at **peak 7** are from 4VP [152]. The δ (0.9 ppm) at **peak 10** from [(-S-$CH_2(CH_2)_{10}C\underline{H_3}$) proton] and δ (3.64 ppm) at **peak 9** from [(-S-$C\underline{H_2}(CH_2)_{10}CH_3$) proton] are attributed to Z group of RAFT agent (DDMAT) [152].

4.2.1 FUNCTIONAL MONOMER COMPOSITION ESTIMATION

Figure 4.9 shows ^{1}H NMR spectra for the PNIPAM homopolymer which has the initial composition of 100 mol% NIPAM. The molar ratio between the functional monomer and the NIPAM can be calculated via the following equation:

$$\frac{Functional\ Monomer\ 1\ (Mol)}{Functional\ Monomer\ 2\ (Mol)} = \frac{\frac{A_1}{No.of\ Proton/s}}{\frac{A_2}{No.of\ Proton/s}} \qquad (1)$$

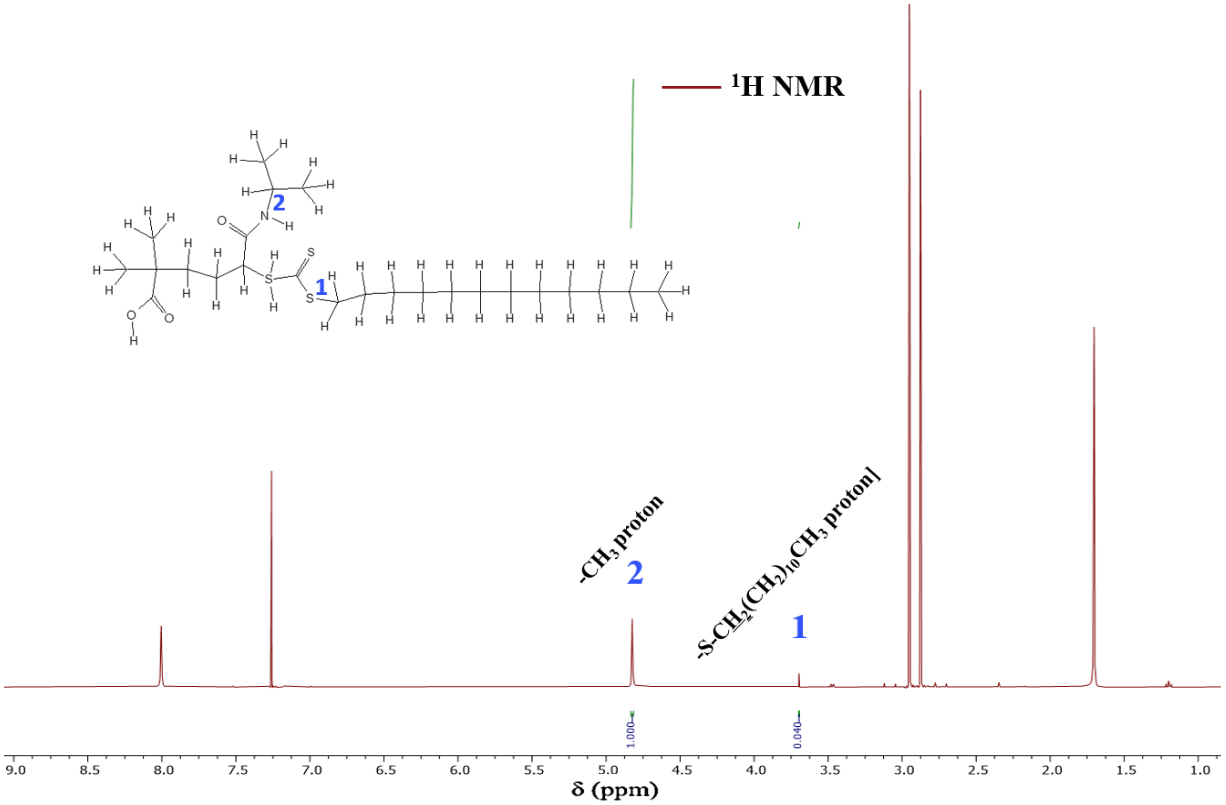

Figure 4.9: ^{1}H NMR spectra of HOMO PNIPAM

The average chain length can be calculated by obtaining the ratio between NIPAM and the chain transfer agent DDMAT as shown in Figure 4.9 using Eq (1):

$$\frac{NIPAM\ (Mol)}{DDMAT\ (Mol)} = \frac{\frac{1.00}{1}}{\frac{0.040}{4}} = \mathbf{100:1}$$

where A_2 is the area of the aromatic protons at 3.64 ppm (coming from RAFT agent) and A_1 is the area of methine protons of isopropyl group (coming from NIPAM) at 4.8 ppm.

Figure 4.10 shows the ^{1}H NMR spectra for 4 nitrophenol templated polymer which had an initial composition of 76 mol% NIPAM, 10 mol% MAA and 14 mol% 4-VP. The ratio between functional monomers NIPAM, 4-VP and MAA can also be calculated using Equation (1).

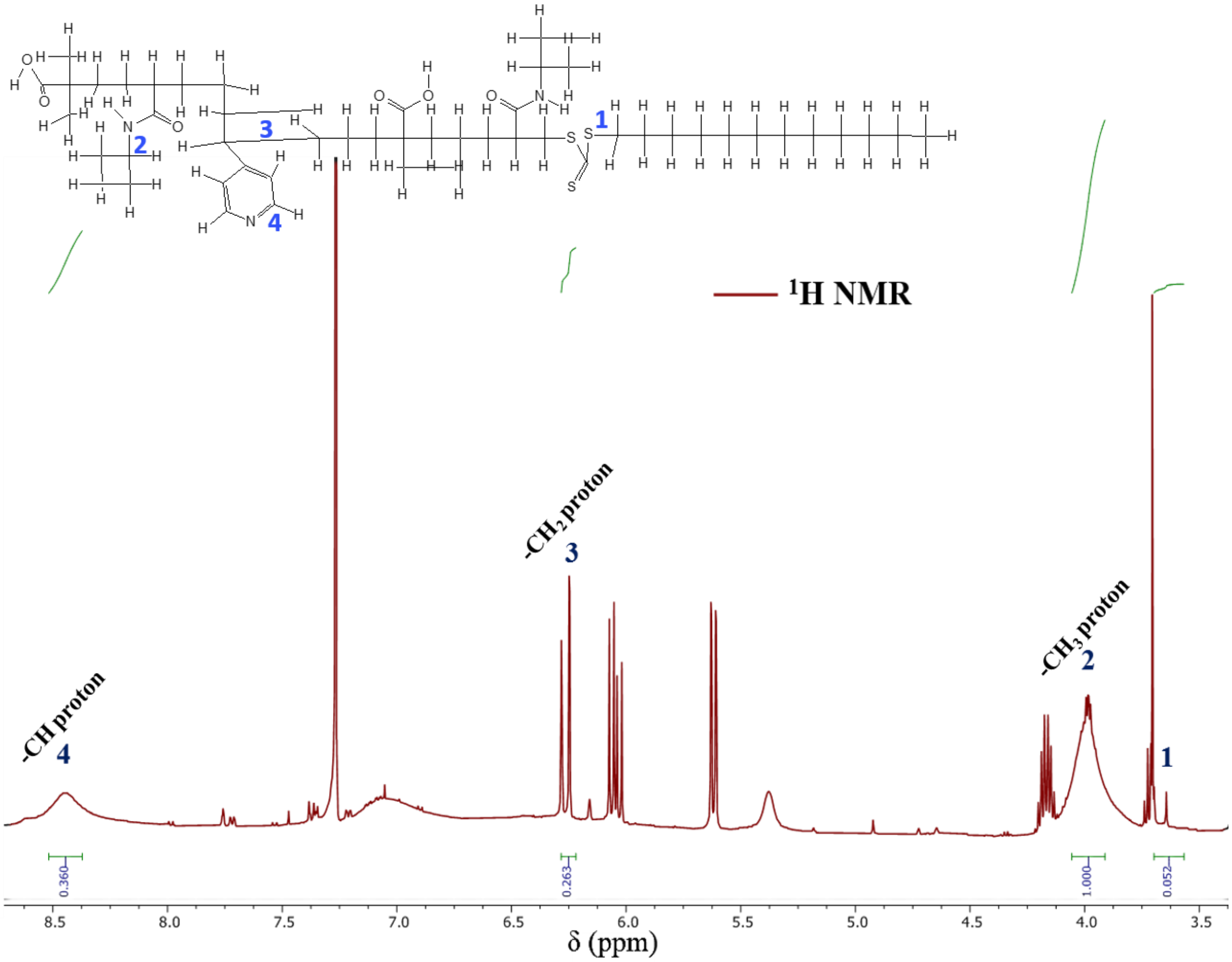

Figure 4.10: ^{1}H NMR spectra of 4 Nitrophenol (4NP) templated (removed) polymer

4-VP : NIPAM

$$\frac{4VP\ (Mol)}{NIPAM\ (Mol)} = \frac{\frac{0.360}{2}}{\frac{1.00}{1}} = \mathbf{13.68 : 76}$$

NIPAM : DDMAT

$$\frac{NIPAM\ (Mol)}{DDMAT\ (Mol)} = \frac{\frac{1.00}{1}}{\frac{0.052}{4}} = \mathbf{76:0.988}$$

Figure 4.11 shows ^{1}H NMR spectra for N methyl glutamate templated polymer which had an initial composition of 87 mol% NIPAM, 5 mol% MAA and 8 mol% 4-VP.

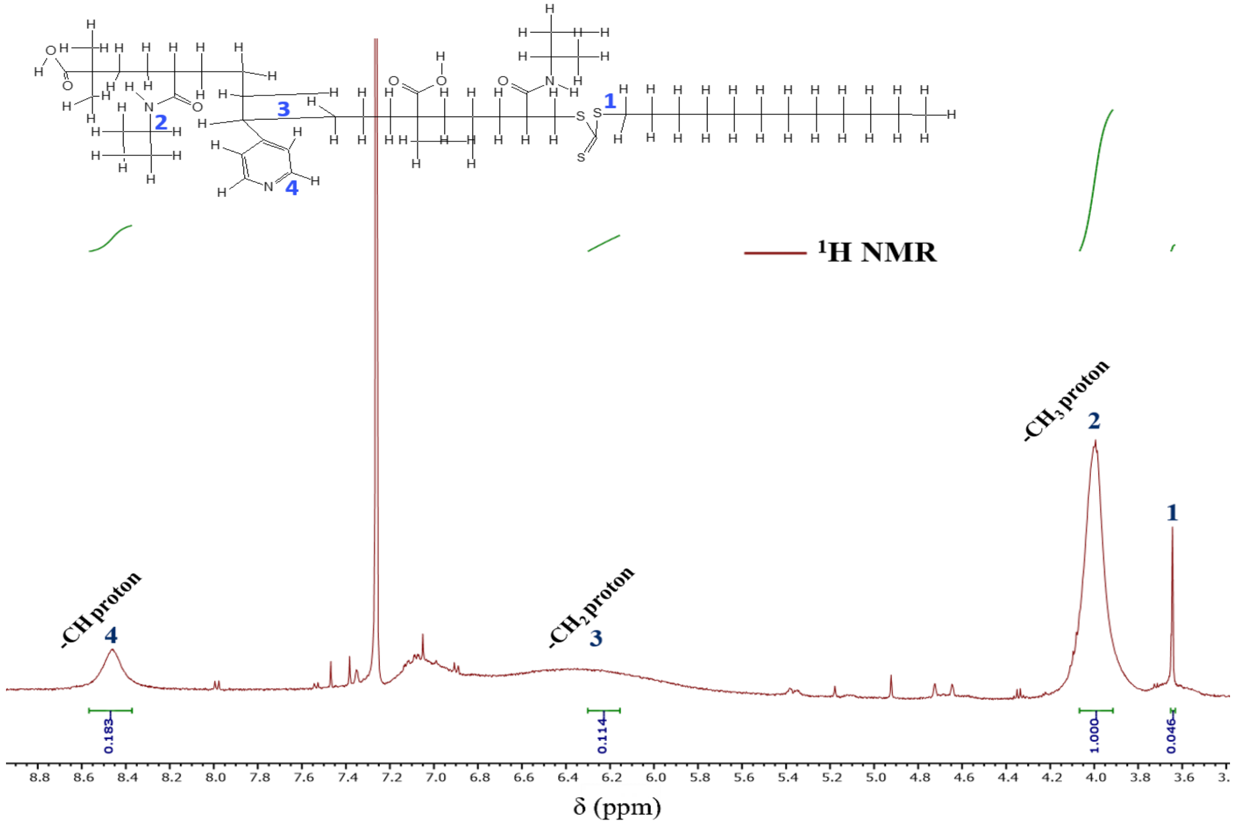

Figure 4.11: ^{1}H NMR spectra of N Methyl Glutamate templated (removed) polymer

The ratio of the functional monomers, the polymer backbone and the chain transfer agent are estimated using Equation (1) as shown below and the ratios closely match the initial composition during synthesis.

4-VP : NIPAM

$$\frac{4VP\ (Mol)}{NIPAM\ (Mol)} = \frac{\frac{0.183}{2}}{\frac{1.00}{1}} = \mathbf{7.96 : 87}$$

NIPAM : DDMAT

$$\frac{NIPAM\ (Mol)}{DDMAT\ (Mol)} = \frac{\frac{1.00}{1}}{\frac{0.046}{4}} = \mathbf{87 : 1}$$

4.3 X-RAY PHOTOELECTRON SPECTROSCOPY (XPS)

X-ray Photoelectron Spectroscopy (XPS), also known as Electron Spectroscopy for Chemical Analysis (ESCA) is the most generally utilized surface investigation technique. It provide an important quantitative information about the chemical binding energy on the surface of the material under study. The average depth of analysis for an XPS measurement is approximately 5 nm. A common XPS can decide the composition (0.1-1.0% minimum is typically quoted) and chemical state of the constituent species.

The samples were tested with the Kratos Axis Supra XPS (X-ray Photoelectron Spectroscopy) system (Figure 4.12) which offers surface analysis, surface chemical mapping, surface imaging, and depth profiling of metallic, semi-metallic and nonmetallic samples as deep as 1 nm. The sample can be evacuated to 10^{-9} Torr or better, for quality measurements.

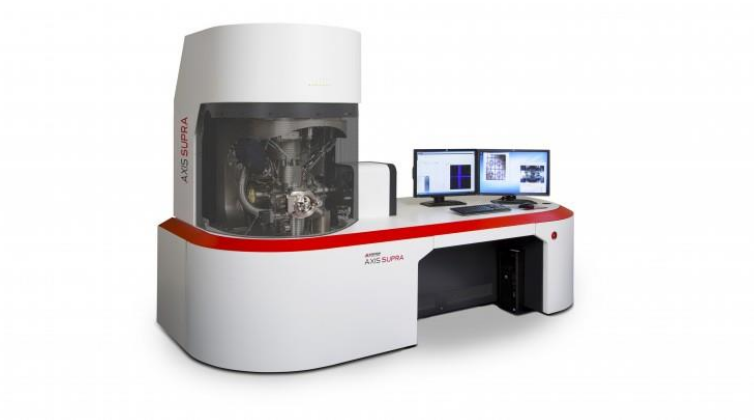

Figure 4.12: Kratos Axis Supra XPS

For XPS measurements, the templated polymer was coated in a custom-made gold electrode array fabricated on a glass slide. Approximately 60 nm gold was initially coated on top of the 5 nm Chromium (Cr) layer via thermal evaporation technique (Edwards E306A). Before photolithography, the Au samples were rinsed sequentially with acetone, ethanol, and deionized water and the dried via nitrogen flow. The samples were spin-coated with S1813 photoresist (MicropsitTM) and baked at 100°C for 1 min followed by exposure to UV. After exposure and development, the samples were rinsed with deionized water and post baked at 120°C for 4 mins. Afterward, the exposed metal area was wet etched via gold and chromium etchant. The sample gold arrays were then cut with a glass cutter to form small pieces of the gold surface which were subjected to a gentle THF and deionized water rinse followed by a N_2 gas blow-dry before use.

4.3.1 SULPHUR (S2p SPECTRA)

Figure 4.13 plots S2p peaks for different polymer deposition conditions. Typically, sulfur content is very low and requires long acquisition time for good quality S2p spectrum. S2p peak has closely spaced spin-orbit components (Δ=1.16eV, intensity ratio=0.511). S2p curve can be decomposed into two components where each one accounts for the spin-orbits splitting doublet such as $S2p_{1/2}$ and $S2p_{3/2}$. Literature indicates that only one bound thiolate species is detectable by

XPS after adsorption of thiol or disulfide molecules onto gold surfaces. The bare Au surface (Figure 4.13(A)) shows S2p peaks associated with SO_2 interaction (~165.8 eV) from the air. The S-O binding in the gold surface can possibly occur due to the binding via the S atom, the two oxygen atoms, and a combination of S and O [153]. The $S2p_{3/2}$ Binding Energy of this bound thiolate species is around 162 eV. The $S2p_{3/2}$ Binding Energies of the unbound thiols and disulfides are between 163.5 and 164 eV [154]. The peaks around 164 eV and beyond are attributed to unbound thiols at the gold surface. This might be due to the physiosorbed thiols at the surface. The peaks around 168 eV and higher can be attributed to the oxidized sulphur at the surface.

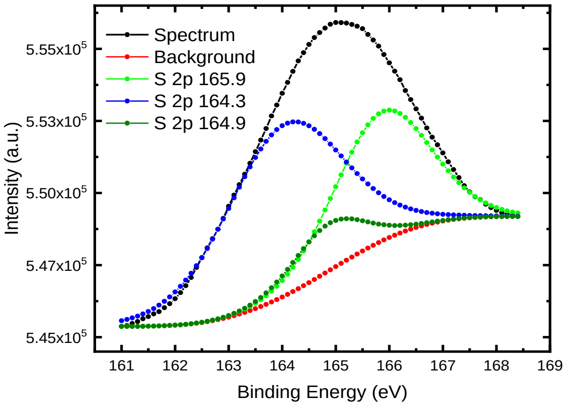

(A)

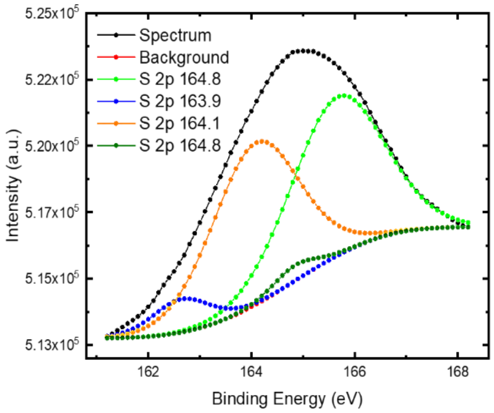

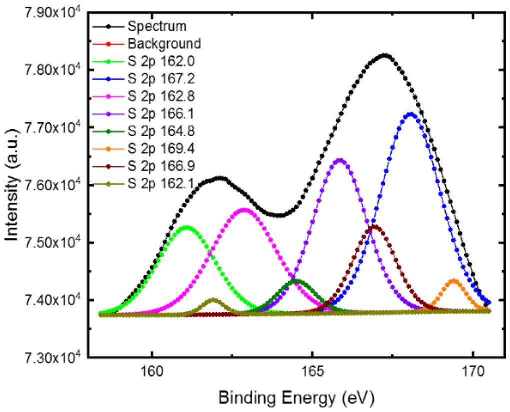

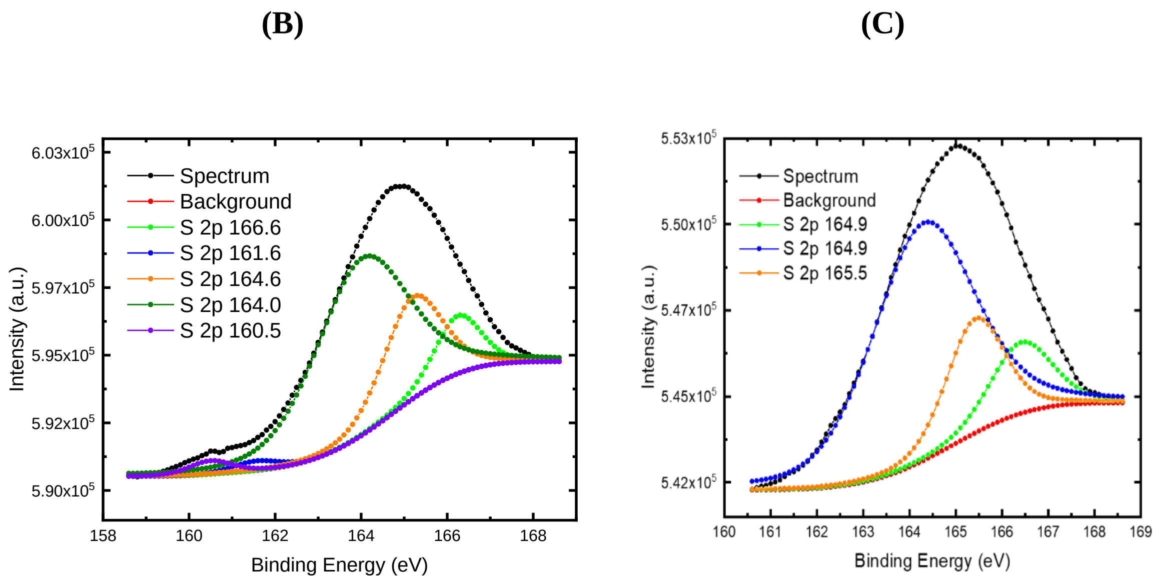

(D)

(E)

Figure 4.13: S2p spectra (A) bare Au ; (B) 20 s polymer attachment without TCEP ; (C) 20 s polymer attachment with TCEP ; (D) 30 mins polymer attachment without TCEP ; (E) 30 mins polymer attachment with TCEP

S2p Intensity vs binding energy fitted data are quantified and tabulated in Table 4.4.

Quantified Data for S2p							
(A) Bare Au							
	BE [eV]	FWHM [eV]	RSF	Atomic conc. [%]	Error [%]	Mass conc. [%]	Error [%]
S 2p 164.9	165.86	2.09	0.67	43.69	10.98	43.69	10.98
S 2p 164.3	164.04	2.59	0.67	56.31	10.98	56.31	10.98
(B) 20 s Polymer attachment without TCEP							
S 2p 164.8	165.66	2.11	0.67	48.82	9.70	48.82	9.70
S 2p 163.9	162.64	1.33	0.67	6.14	7.29	6.14	7.29
S 2p 164.1	164.08	2.00	0.67	45.04	9.47	45.04	9.47
(C) 20 s Polymer attachment with TCEP							
S 2p 162.0	161.07	2.13	0.67	13.31	4.76	13.31	4.76
S 2p 167.2	168.06	2.19	0.67	31.07	5.06	31.07	5.06
S 2p 162.8	162.87	2.40	0.67	17.90	5.19	17.90	5.19
S 2p 166.1	165.85	1.99	0.67	21.79	4.55	21.79	4.55
S 2p 164.8	164.50	1.40	0.67	3.29	3.34	3.29	3.34
S 2p 169.4	169.40	0.90	0.67	1.97	2.17	1.97	2.17
S 2p 166.9	166.93	1.60	0.67	9.84	3.76	9.84	3.76
S 2p 162.1	161.90	0.80	0.67	0.83	1.96	0.83	1.96

(D) 30 mins Polymer attachment without TCEP							
S 2p 164.6	165.20	1.62	0.67	34.83	11.78	34.83	11.78
S 2p 164.0	164.01	2.56	0.67	62.92	12.32	62.92	12.32
S 2p 160.5	160.50	1.20	0.67	2.24	7.38	2.24	7.38
(E) 30 mins Polymer attachment with TCEP							
S 2p 164.9	164.29	2.60	0.67	81.25	8.18	81.25	8.18
S 2p 165.5	165.42	1.48	0.67	18.75	8.18	18.75	8.18

Table 4.4: Quantified binding energies for S2p peak at different deposition scenario

4.3.2 NITROGEN (N 1S) SPECTRA

In Figure 4.14(A), N1s peaks (~396 eV) associated with chemisorbed nitrogen at the bare gold surface occur from the chemical interaction of nitrogen present in the air along with adventitious carbon species [155]. High-resolution N1s XPS scan with a curve is fitted using the peaks with binding energies of 398.5, 398.2, 398.3 and 397.5 eV in Figure 4.14(C). This sample was prepared by 20s attachment of PNIPAM on Au with TCEP. The major peak at 398.3 eV was attributed to the CNH units of PNIPAM [156]. In the case of 30 mins of attachment of PNIPAM with Au, N1s spectra for samples with or without TCEP show binding energy distribution between 396.2 and 399.2 eV. Figure 4.14(D) features a minor characteristic of double peak structure for the azido groups at 396.2 and 399.2 eV, with a BE split of 3.7 eV [157].

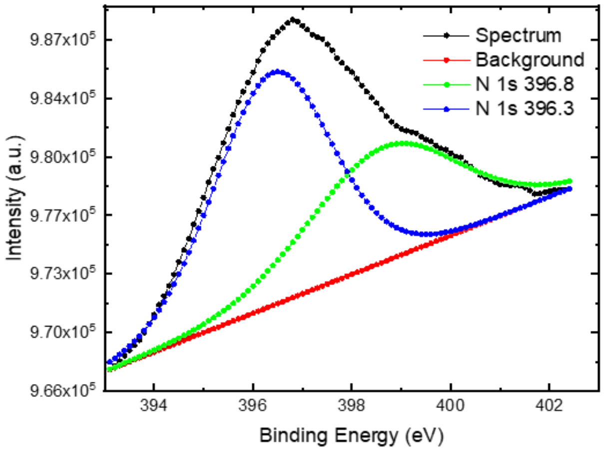

(A)

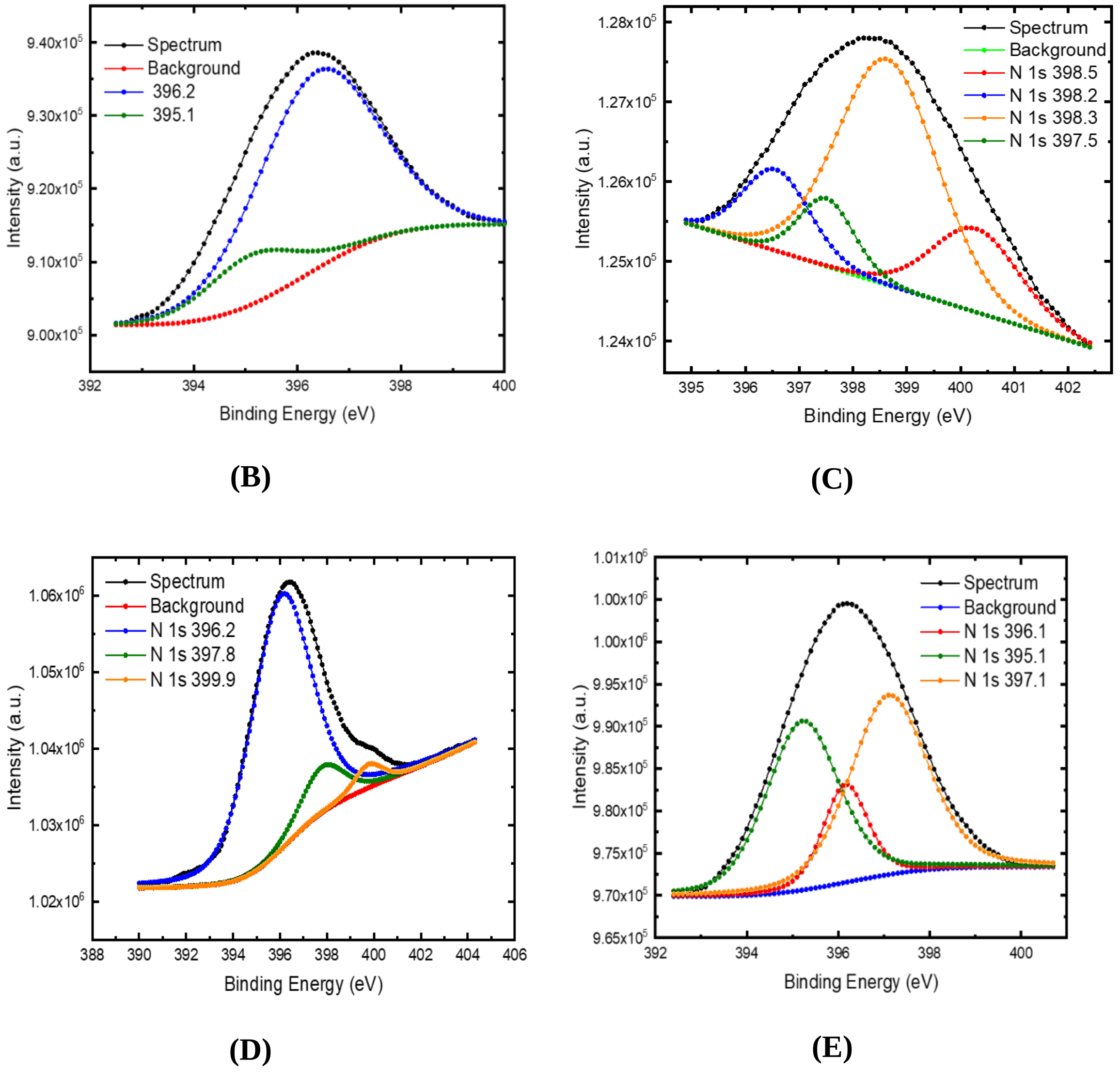

Figure 4.14: N1s spectra (A) bare Au; (B) 20 s polymer attachment without TCEP; (C) 20 s polymer attachment with TCEP; (D) 30 mins polymer attachment without TCEP; (E) 30 mins polymer attachment with TCEP

N1s Intensity vs binding energy fitted data are quantified and tabulated in Table 4.5.

Quantified Data for N1s							
(A) Bare Au							
	BE [eV]	FWHM [eV]	RSF	Atomic conc. [%]	Error [%]	Mass conc. [%]	Error [%]
N 1s 396.8	398.65	3.60	0.48	38.75	14.00	38.75	14.00

N 1s 396.3	396.39	2.80	0.48	61.25	14.00	61.25	14.00
(B) 20 s Polymer attachment without TCEP							
N 1s 396.2	396.37	2.74	0.48	83.92	7.16	83.92	7.16
N 1s 395.1	395.10	2.07	0.48	16.08	7.16	16.08	7.16
(C) 20 s Polymer attachment with TCEP							
N 1s 398.5	400.29	1.93	0.48	18.80	20.05	18.80	20.05
N 1s 398.2	396.57	1.46	0.48	13.87	16.15	13.87	16.15
N 1s 398.3	398.64	2.20	0.48	57.86	21.99	57.86	21.99
N 1s 397.5	397.51	1.20	0.48	9.47	13.70	9.47	13.70
(D) 30 mins Polymer attachment without TCEP							
N 1s 396.2	396.05	3.00	0.48	85.06	7.23	85.06	7.23
N 1s 397.8	397.79	2.20	0.48	11.26	6.36	11.26	6.36
N 1s 399.9	399.76	1.40	0.48	3.68	4.32	3.68	4.32
(E) 30 mins Polymer attachment with TCEP							
N 1s 396.1	396.15	1.16	0.48	14.39	4.19	14.39	4.19
N 1s 395.1	395.22	1.87	0.48	40.14	5.68	40.14	5.68
N 1s 397.1	397.10	2.00	0.48	45.46	5.78	45.46	5.78

Table 4.5: Quantified binding energies for N1s peak at different deposition scenario

4.3.3 CARBON (C 1S) SPECTRA

The high-resolution C1s XPS spectra are shown in Figure 4.15. In Figure 4.15(A), the C1s spectra arise due to the hydrocarbon species present at the surface coupled with such species having complex interaction with air [158]. Figure 4.15(c) which shows C1s binding spectra exhibits the best result in terms of binding. These were curve fitted using the peaks with binding energies of 283.9, 284.9, and 286.1 eV, which are attributable to chemical bonding environments C-C/H, C-N, and C=O, respectively. The binding energies for these three groups are slightly lower than the previously reported value by Yu et. al [159]. The intensity of carbon peak increased after the conjugation of PNIPAM polymer chain onto Au because a higher concentration of carbon is incorporated in PNIPAM chain [160].

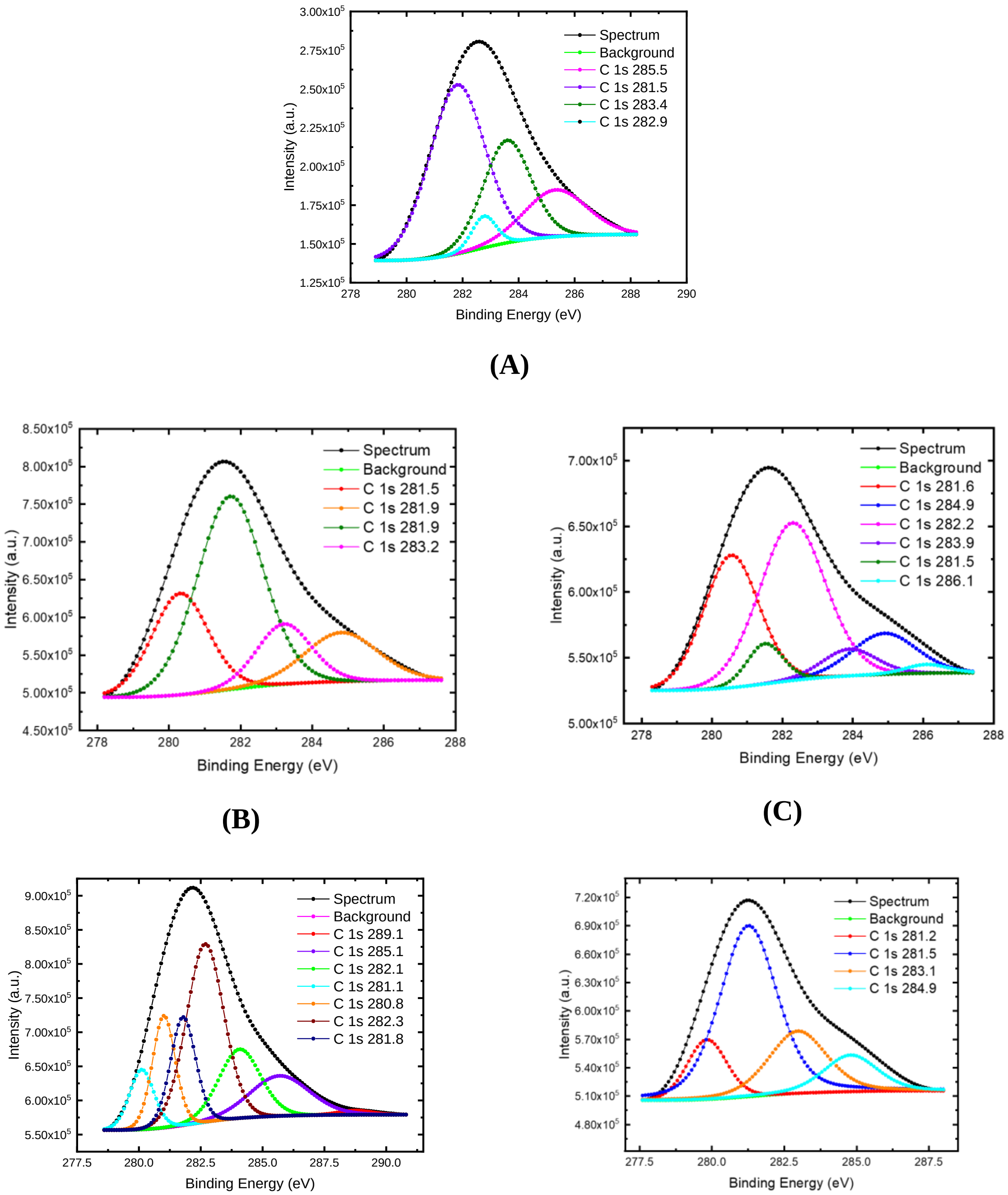

(A)

(B) **(C)**

(D) **(E)**

Figure 4.15: C1s spectra (A) bare Au; (B) 20 s polymer attachment without TCEP; (C) 20 s polymer attachment with TCEP; (D) 30 mins polymer attachment without TCEP; (E) 30 mins polymer attachment with TCEP

C1s Intensity vs binding energy fitted data are quantified and tabulated in table 4.6.

Quantified Data for C1s							
(A) Bare Au							
	BE [eV]	FWHM [eV]	RSF	Atomic conc. [%]	Error [%]	Mass conc. [%]	Error [%]
C 1s 282.5	281.81	2.32	0.28	68.45	0.72	68.45	0.72
C 1s 283.4	283.58	2.00	0.28	27.24	0.66	27.24	0.66
C 1s 282.9	282.76	1.02	0.28	4.30	0.42	4.30	0.42
(B) 20 s Polymer attachment without TCEP							
C 1s 281.5	280.31	1.85	0.28	22.60	0.47	22.60	0.47
C 1s 281.9	281.71	2.16	0.28	64.39	0.57	64.39	0.57
C 1s 283.2	283.21	1.80	0.28	13.01	0.47	13.01	0.47
(C) 20 s Polymer attachment with TCEP							
C 1s 281.6	280.55	1.85	0.28	31.09	0.90	31.09	0.90
C 1s 284.9	284.89	2.16	0.28	11.20	0.97	11.20	0.97
C 1s 282.2	282.28	2.20	0.28	43.94	1.06	43.94	1.06
C 1s 283.9	283.90	1.80	0.28	6.10	0.86	6.10	0.86
C 1s 281.5	281.50	1.20	0.28	6.11	0.62	6.11	0.62
C 1s 286.1	286.10	1.40	0.28	1.56	0.67	1.56	0.67
(D) 30 mins Polymer attachment without TCEP							
C 1s 282.1	284.07	1.98	0.28	28.63	0.68	28.63	0.68
C 1s 281.1	280.12	1.16	0.28	7.78	0.27	7.78	0.27
C 1s 281.8	281.79	1.20	0.28	28.10	0.43	28.10	0.43
C 1s 282.3	282.68	1.79	0.28	35.49	0.48	35.49	0.48
(E) 30 mins Polymer attachment with TCEP							
C 1s 282.2	282.27	1.90	0.28	49.26	1.06	49.26	1.06
C 1s 283.4	283.68	2.04	0.28	28.41	1.07	28.41	1.07
C 1s 280.7	279.86	0.81	0.28	1.87	0.49	1.87	0.49
C 1s 280.8	280.99	1.44	0.28	20.46	0.84	20.46	0.84

Table 4.6: Quantified binding energies for C1s peak at different deposition scenario

4.3.4 GOLD (Au4f) XPS SPECTRA

Figure 4.6 plots Au4f XPS spectra for bare Au and modified Au conditions. The peaks in the Au4f region have an asymmetric peak shape. The Au4f$_{7/2}$ peak is the most meaningful binding energy reference (Au4f$_{7/2}$ at around 84.00eV) [161]. The spectrum (Figure 4.6(A)) of bare gold surface displays the expected peaks, including those at binding energies of 84.2 eV attributed to Au4f$_{7/2}$. The intensity of the bare gold for Au4f$_{7/2}$ is close to 6.6×10^{5} a.u. . The gold signal attenuation, observed at three conditions, plotted in Figure 4.6 (B - D) with intensities of 5.9×10^{5}, 5×10^{4} and 5.7×10^{5} a.u. respectively is due to the covering of the Au surface by the PNIPAM overlayer. As expected, the condition where PNIPAM is deposited on Au for 20s shows nearly 13-fold signal attenuation.

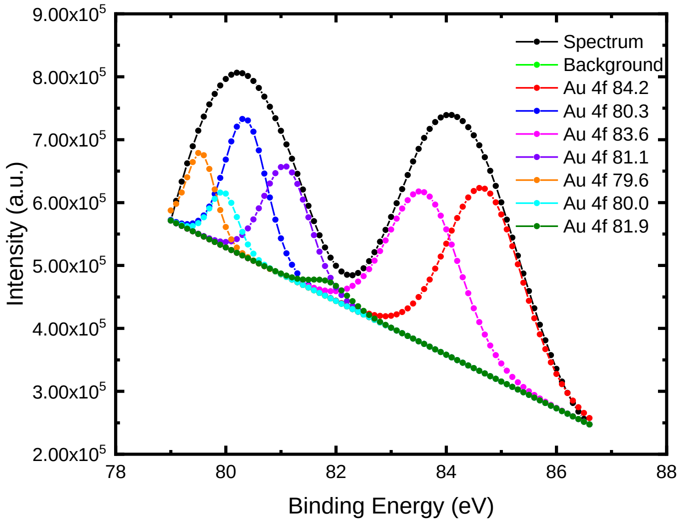

(A)

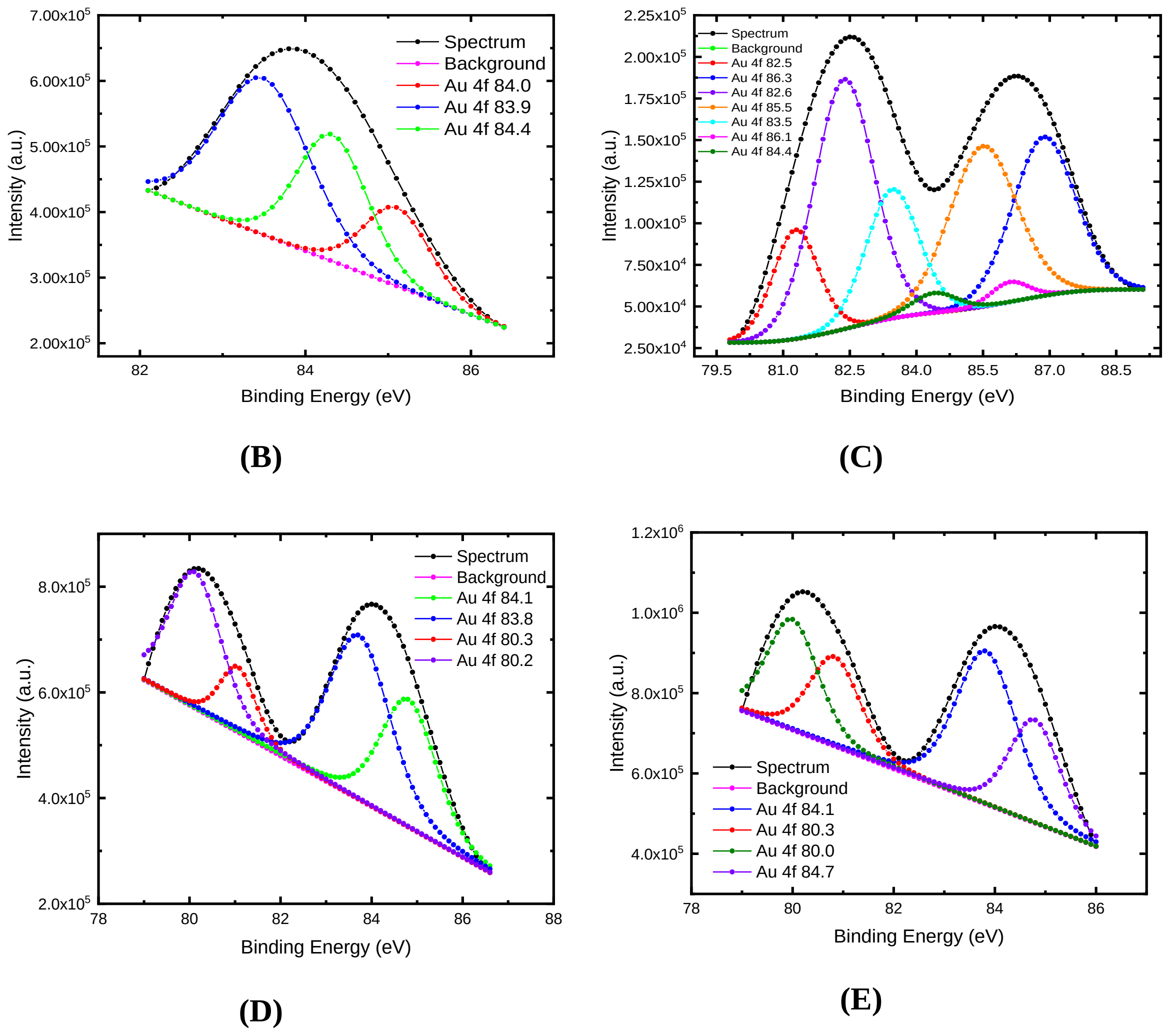

Figure 4.16: Au4f spectra (A) bare Au; (B) 20 s polymer attachment without TCEP; (C) 20 s polymer attachment with TCEP; (D) 30 mins polymer attachment without TCEP; (E) 30 mins polymer attachment with TCEP

Au4f Intensity vs binding energy fitted data are quantified and tabulated in Table 4.7.

Quantified Data for C1s							
(A) Bare Au							
	BE [eV]	FWHM [eV]	RSF	Atomic conc. [%]	Error [%]	Mass conc. [%]	Error [%]
Au 4f 84.2	84.70	1.63	6.25	34.82	0.24	34.82	0.24
Au 4f 80.3	80.36	0.90	6.25	14.37	0.17	14.37	0.17
Au 4f 83.6	83.60	1.54	6.25	26.95	0.24	26.95	0.24
Au 4f 81.1	81.10	1.00	6.25	12.75	0.17	12.75	0.17
Au 4f 79.6	79.55	0.62	6.25	5.88	0.12	5.88	0.12

Au 4f 80.0	79.97	0.60	6.25	3.76	0.12	3.76	0.12
Au 4f 81.9	81.90	0.80	6.25	1.47	0.13	1.47	0.13
(B) 20 s Polymer attachment without TCEP							
Au 4f 80.7	80.75	1.12	6.25	21.64	0.14	21.64	0.14
Au 4f 84.4	84.43	1.64	6.25	32.69	0.17	32.69	0.17
Au 4f 81.6	81.59	1.00	6.25	10.86	0.11	10.86	0.11
Au 4f 79.8	79.80	0.91	6.25	11.20	0.11	11.20	0.11
Au 4f 85.5	85.50	1.20	6.25	8.34	0.13	8.34	0.13
Au 4f 83.1	83.24	1.60	6.25	11.58	0.16	11.58	0.16
Au 4f 80.3	80.30	0.60	6.25	2.15	0.08	2.15	0.08
Au 4f 82.3	82.30	0.80	6.25	1.53	0.09	1.53	0.09
(C) 20 s Polymer attachment with TCEP							
Au 4f 82.5	81.28	1.22	6.25	10.17	0.16	10.17	0.16
Au 4f 86.3	86.87	1.66	6.25	20.19	0.22	20.19	0.22
Au 4f 82.6	82.37	1.59	6.25	30.43	0.23	30.43	0.23
Au 4f 85.5	85.50	1.80	6.25	22.08	0.23	22.08	0.23
Au 4f 83.5	83.46	1.40	6.25	13.79	0.19	13.79	0.19
Au 4f 86.1	86.10	1.00	6.25	1.52	0.17	1.52	0.17
Au 4f 84.4	84.40	1.20	6.25	1.81	0.17	1.81	0.17
(D) 30 mins Polymer attachment without TCEP							
Au 4f 84.1	84.81	1.45	6.25	26.71	0.23	26.71	0.23
Au 4f 83.8	83.73	1.60	6.25	37.94	0.25	37.94	0.25
Au 4f 80.3	81.06	0.93	6.25	8.72	0.18	8.72	0.18
Au 4f 80.2	80.12	1.35	6.25	26.63	0.24	26.63	0.24
(E) 30 mins Polymer attachment with TCEP							
Au 4f 84.1	83.83	1.43	6.25	37.55	0.24	37.55	0.24
Au 4f 80.3	80.84	1.19	6.25	18.27	0.22	18.27	0.22
Au 4f 80.0	80.00	1.20	6.25	22.87	0.22	22.87	0.22
Au 4f 84.7	84.79	1.20	6.25	21.32	0.21	21.32	0.21

Table 4.7: Quantified binding energies for Au4f peak at different deposition scenario

CHAPTER 5: ELECTRODE SURFACE COVERAGE CHARACTERIZATION

5.1 OVERVIEW

PNIPAM shows a temperature-dependent single-chain elasticity when the temperature is increased across the LCST. Such conformation changes originate from the presence/absence of the H-bond donors on the side groups. Containing both H-bond donor and acceptor, the PNIPAM chain is more hydrated at room temperature and will have a larger change in both conformation and hydration upon heating. The chain length reliance of the single chain formation, in this way, not the entire story, yet the interchain progress isn't autonomous of the single chain progress. The compliances framed by the single chain progress will influence conglomeration of various chains and along these lines the universal LCST.

Literatures suggest the coil to-globule formation of PNIPAM chain aided by hydration phenomenon of the polymer [162]. At the point when single chains in water are contemplated by means of atomic elements, the general change in the quantity of hydrogen bonds above and beneath the LCST is irrelevant. But an adjustment in the structure of the water molecules in the first hydration sphere is seen with the beginning of the change with diminishing solvation of the polymer observed beyond the LCST [163]. A shrink in the hydrogen bonding among PNIPAM and water is found just as an expansion in intrachain hydrogen bonds when the collapsed state is contrasted with the extended state [164].

Below the LCST, a few contacts including hydrophobic interactions develop between the chains of the isotactic-rich PNIPAM during the equilibrium phase and the inter-chain contacts persevere throughout the chain. Significant number of hydrophobic contacts is identified for the atactic stereoisomer. Furthermore, the interaction between oxygen and nitrogen atoms show the same difference between stereoisomers. It is important that the N–O contacts are less probable compared to hydrophobic interactions, regardless of stereochemistry. The result of polar interactions is clarified by the hydration of the amide moiety, anticipating relationship of polar gatherings at 283 K [165].

The radiation of gyration of 20-mer PNIPAM does not show significant phase transition when the temperature was switched to higher than LCST and the value is comparable to temperature lower than LCST. Similar kind of results were found for the 40-mer and the 60-mer at temperatures over the phase transition i.e. LCST. Furthermore, at temperatures below the LCST, no uncommon increment in the span of gyration was watched and no unfurling of the chain happened for both 40-mer and 60-mer PNIPAM.

Longer polymer chains comprising of 100 to 400 monomers performed better in terms of change in radiation of gyration when temperature varied compared to shorter polymer chains i.e. 20 to 60-mer. There is a huge drop in the radius of gyration for all chain lengths between the temperatures 180 and 200 K. At temperatures after the drop, the range of gyration does not increment as fast for longer chains with respect to shorter. Just the 100-mer unfolds fundamentally, and not as much as the 40 or 60-mer chains [166]. 100-mer polymer chain was primarily chosen for better stimuli response.

It is evident that, following the initial reduction with $NaBH_4$ and subsequent purification via dialysis, polymeric disulfides, namely, PNIPAM-S-S-PNIPAM, are formed. However, coupling can be easily reversed by the addition of a weak reducing agent. The molecular weight distributions for the coupled PNIPAM at several different time intervals following the addition of TCEP is different [167]. The cleavage of the trithiocarbonate with a strong reducing agent, in this case, $NaBH_4$, can form a mixture of polymeric thiols and disulfides but in the presence of tris(2-carboxyethyl) phosphine HCl (TCEP), the conjugation of Au to the pure polymeric thiol would be easier. TCEP effectively eliminates the formation of polymeric disulfides and thus allows for the desired addition of the free polymeric thiol across the Au.

5.2 TP BASED ELECTROCHEMICAL SENSOR PREPARATION

BASI MF-2114 Au electrodes were used for the TP based electrochemical sensor. The circular Au electrode has 3 mm in diameter. As electrodes were reused for multiple experiments, they were first immersed in 4.5% NH_4OH, 1.5% H_2O_2 and 94% DI water mixture while stirring the solution with a magnetic stirrer for at least 12 hours. Afterward, the electrodes were polished in polycrystalline diamond suspended solution on a micro cloth. The polished electrodes were sonicated in ultra-sonication bath for 10 mins to ensure surface contaminant removal. The steps are shown in Figure 5.1. After drying, the electrode was used in two electrode cyclic voltammetry setup. The electrolyte was 0.5M H_2SO_4 and CV scan rate was chosen as 300mV/s. Cyclic voltammetry ensures the activation of available of Au surface. The initial CV scan ranged from -0.3 V to 1.70 V (Figure: 5.2(A)) and final scan ranged from 0 V to 1.70 V (Fig: 5.2(B)). Both scans were repeated 20 times. After CV, the Au electrode was sonicated in ultra-sonication bath firstly in 100% ethanol and finally in DI water. The sonication duration was 10 minutes for each step. After the sonication steps, the electrode was dried and ready for polymer deposition.

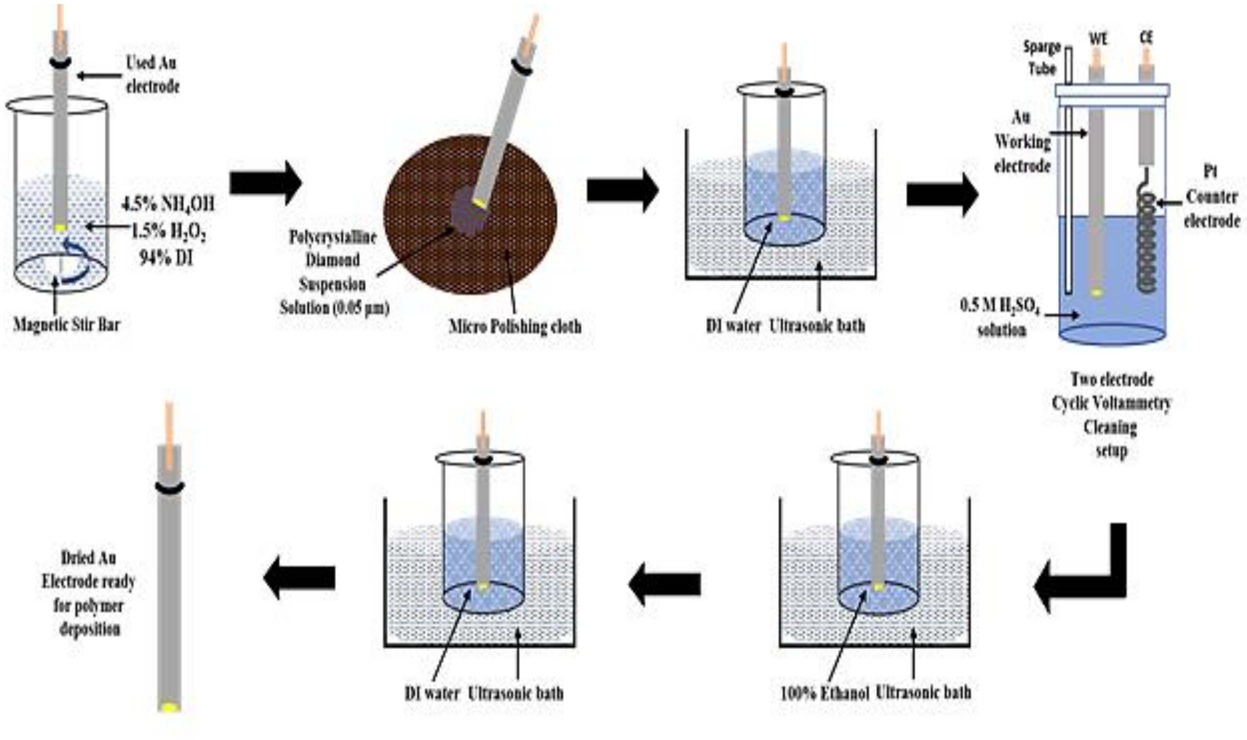

Figure 5.1: Electrochemical sensor preparation

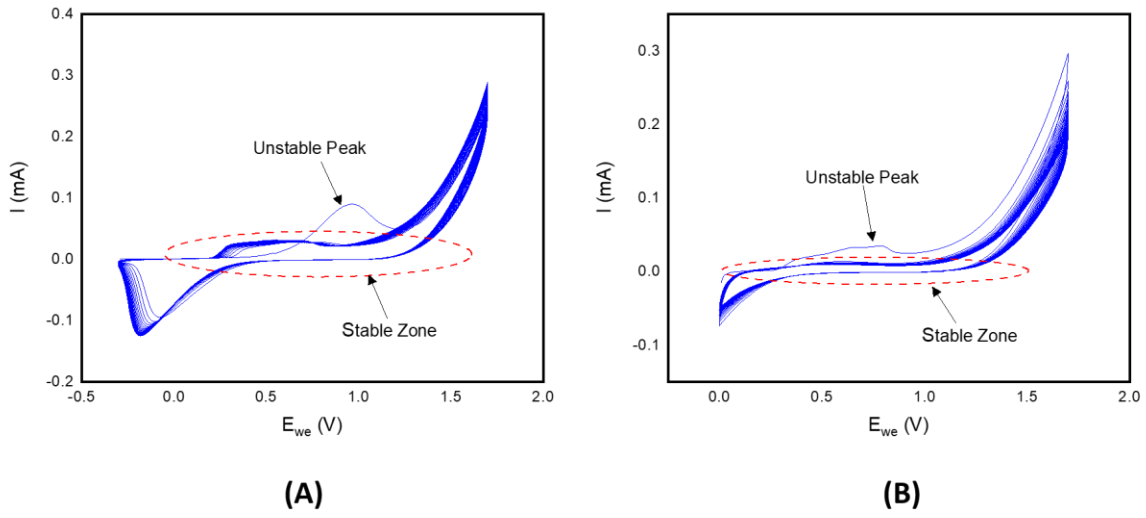

(A) **(B)**

Figure 5.2: Cyclic Voltammetric cleaning cycle in 1M H_2SO_4

5.3 TP ATTACHMENT TO AU ELECTRODE

A desired concentration of Lyophilized PNIPAM powder was mixed in DI water with or without TCEP depending on the experiment criteria. The mixture was slowly stirred with magnetic stir bar until the powder was fully dissolved. The mixture was kept in a sealed container for at least three weeks to ensure the untangling process of the PNIPAM chain. Afterward, the polymers are ready to be attached to Au electrode. During the attachment, the magnetic stir bar was used with low RPM. After attachment, the electrode was cleaned with THF and DI water to ensure that unattached or loosely absorbed polymer on surface was washed away. After the electrode was dried, it was tested with a potentiostat in a 3-electrode electrochemical cell at room temperature.

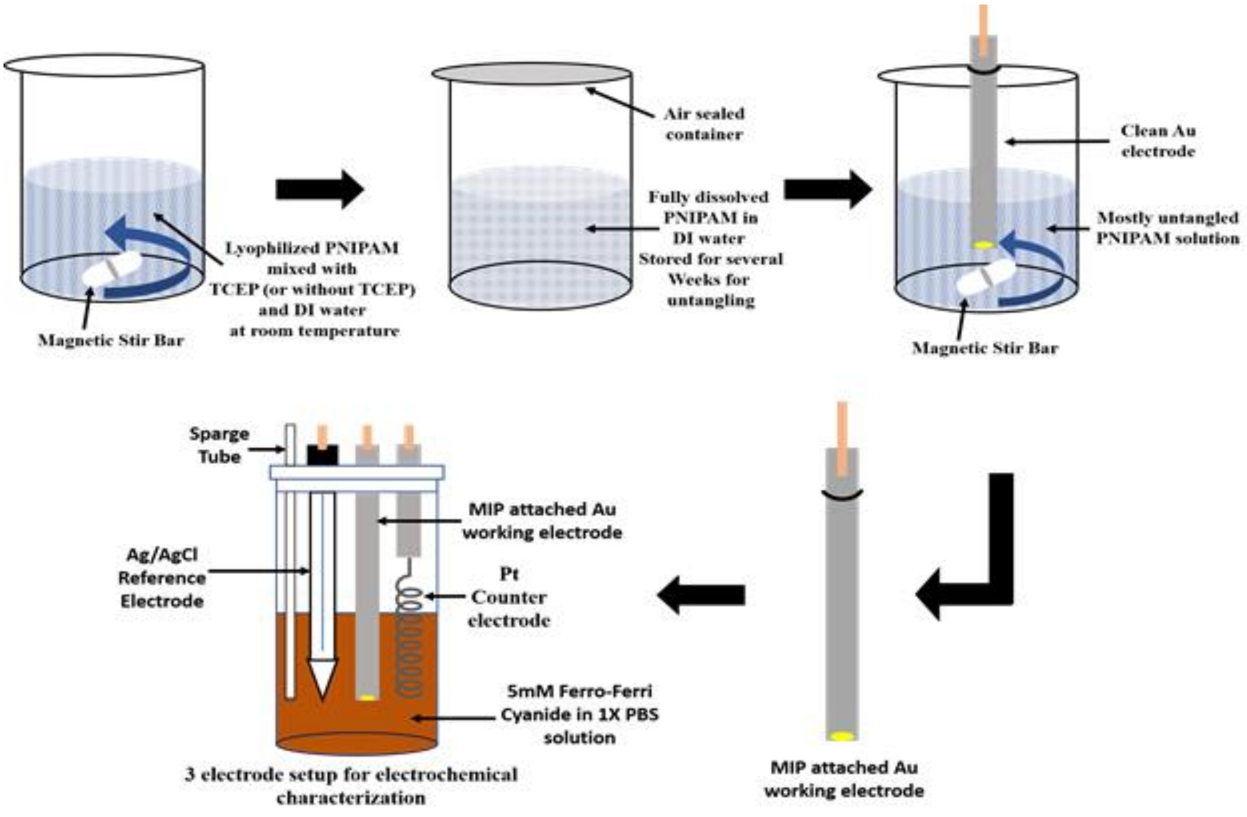

Figure 5.3: Polymer attachment and electrochemical characterization process

This chapter discusses the electrochemical characteristic of an Au surface after depositing of 100-mer PNIPAM with and without TCEP. PNIPAM with different molecular weight, namely, 50, 200, 500-mer are also tested however due to the tangling issue, a 100-mer PNIPAM is chosen for polymeric sensing platform. A modified Au electrode after TP attachment is illustrated in the Figure 5.4.

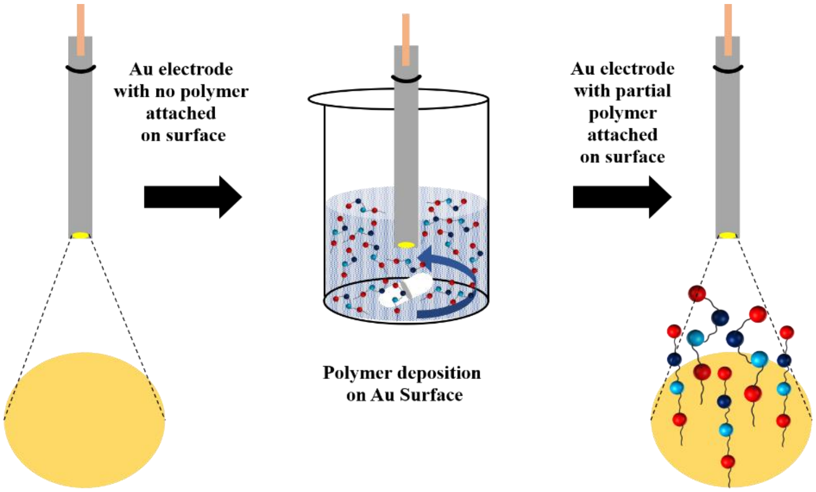

Figure 5.4: Partial Polymer deposition on Au surface

5.4 40 mg/L 100 MER PNIPAM WITHOUT TCEP

The initial concentration was chosen to be 40 mg/L for the electrochemical experiment for the 100-mer non-templated PNIPAM. Figure 5.5 and 5.6 show the cyclic voltammetry and the EIS plot, respectively. The polymer solution was made without TCEP and gradually deposited on the Au surface. The CV current peaks are gradually decreased with increasing polymer attachment as expected. More polymer chains block the Au surface and resisted the electron transfer process between 5 mM Ferro-/ferri Cyanide and the Au electrode. The EIS plot also suggest the increment of surface impedance with higher polymer attachment. These results suggest that the PNIPAM chain can be attached to the Au electrode without a reducing agent such as TCEP. However, the majority of this attachment is physisorption rather than chemisorption as XPS results suggested earlier.

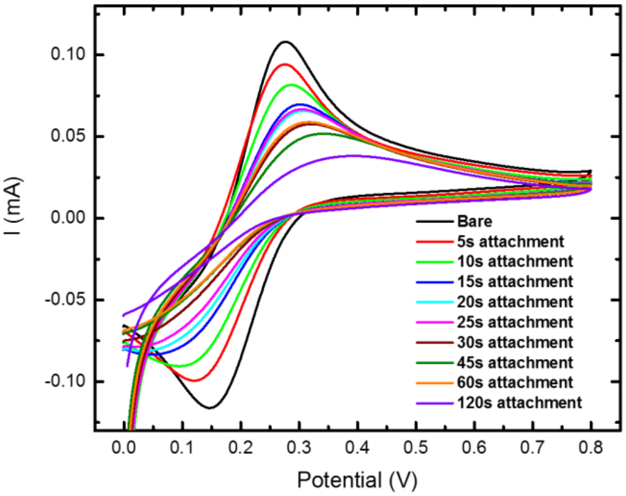

Figure 5.5: CV curve (scan rate: 100mV) for 100 mer 40 mg PNIPAM (without TCEP) attached to Au electrode

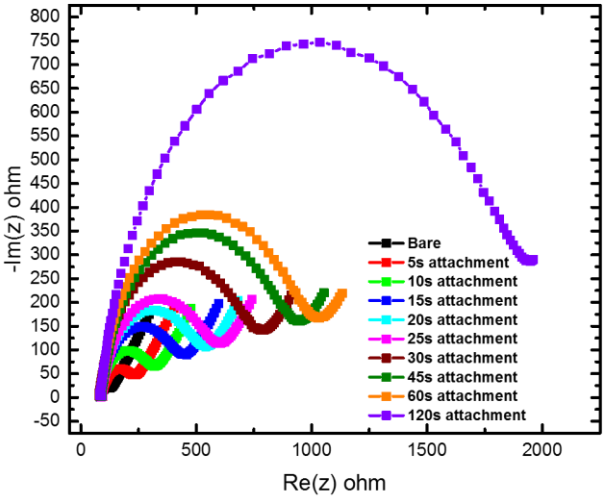

Figure 5.6: EIS curve for 100 mer 40 mg PNIPAM (without TCEP) attached to Au electrode

5.5 40 mg/L 100 MER PNIPAM WITH TCEP

Figure 5.7 and 5.8 show the cyclic voltammetry and the electrochemical impedance spectroscopy plots, respectively for 40 mg/L 100-mer PNIPAM with TCEP. The ratio PNIPAM:TCEP is approximately 1:0.85. The CV current peaks decreased with increasing polymer deposition. The EIS plot also shows an increase in impedance. An important observation is that the diffusion tail of EIS plot starts to disappear at around 40s of deposition time. This suggests that the Au surface is fully covered with PNIPAM well before 40s. The gradual increase of the impedance shows a linear trend compared to that without TCEP. Furthermore, there is a higher percentage of chemisorption as suggested by the XPS data. The 40 mg/L PNIPAM in water is extremely high concentration for achieving controlled deposition and therefore there is a significant portion of tangled polymers attached to the electrode.

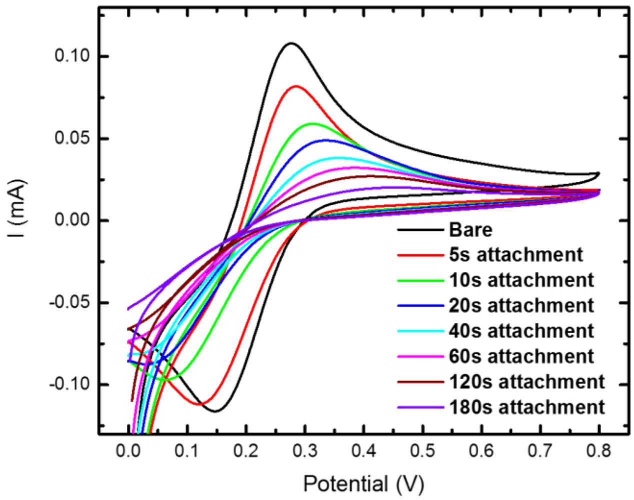

Figure 5.7: CV curve (scan rate: 100mV) for 100 mer 40 mg PNIPAM (with TCEP) attached to Au electrode

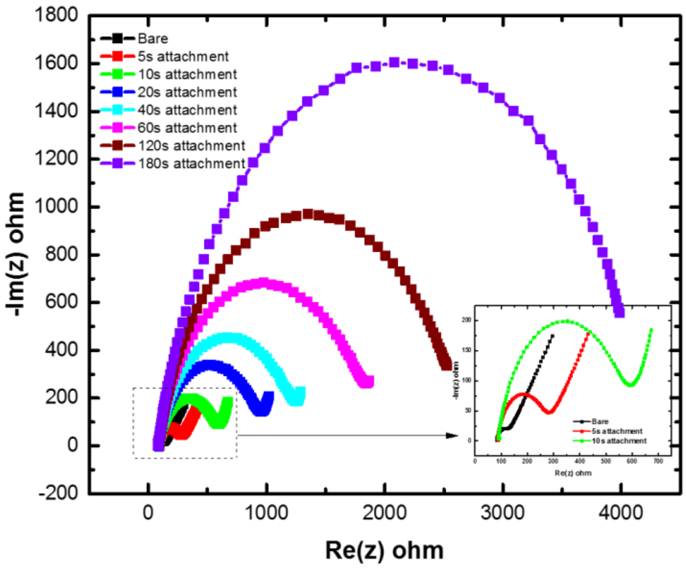

Figure 5.8: EIS curve for 100 mer 40 mg/L PNIPAM (with TCEP) attached to Au electrode

5.6 0.5 mg/L and 0.05 mg/L 100 MER PNIPAM WITH TCEP

Figure 5.9 shows the EIS plot of 0.5 mg/L 100 mer PNIPAM with TCEP after attachment to the Au electrode with varying deposition time. It can be clearly seen that the deposition is more controlled compared to the 40 mg/L concentration since a diffusion tail is still visible even after 30mins. All the EIS curve can be fitted to the following modified Randle's circuit as shown in Figure 5.10.

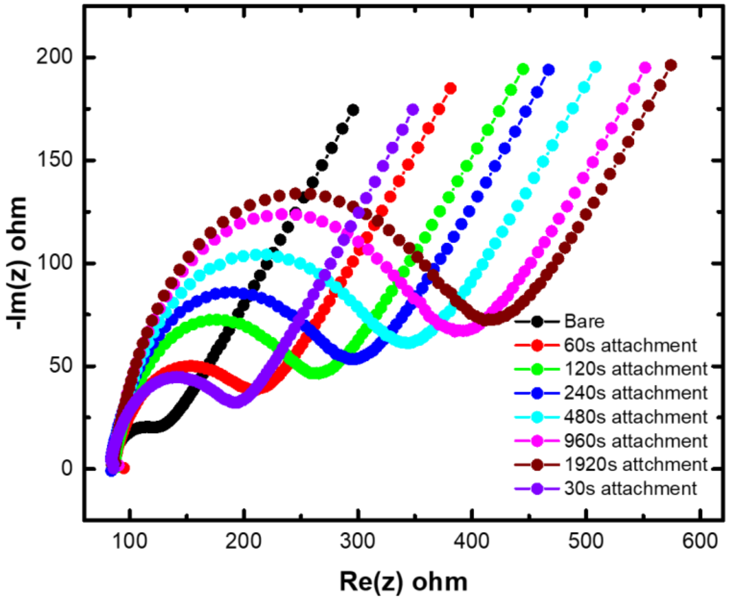

Figure 5.9: EIS curve for 100 mer 0.5 mg PNIPAM (with TCEP) attached to Au electrode

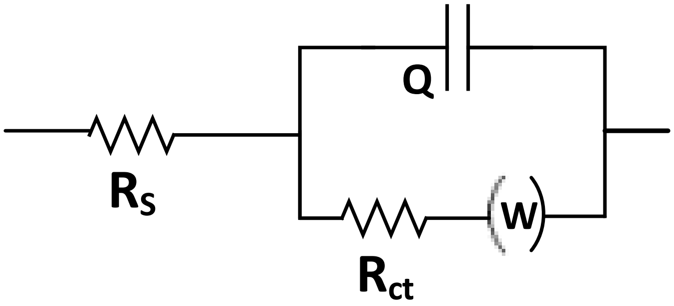

Figure 5.10: Equivalent Randle's circuit model for EIS plot shown in figure 5.5

The charge transfer resistance, Rct, which describes the electron transfer from one phase (e.g. electrode) to another (e.g. liquid), can be calculated from the circuit parameters. The value of R_{ct} can be used to calculate the surface coverage, $\boldsymbol{\theta(t)}$, of PNIPAM attachment to the Au electrode.

$$\text{Surface Coverage, } \boldsymbol{\theta(t)} = \left[\mathbf{1} - \left(\frac{R_{ct,gold\ (t=0)}}{R_{ct,polymer\ (t)}}\right)\right] \times \mathbf{100}$$

Where, $R_{ct,\ gold\ (t=0)}$ = Charge transfer resistance of Blank Au electrode

$R_{ct,\ polymer\ (t)}$ = Charge transfer resistance of polymer attached Au electrode at time t

Table 5.1 shows the calculated surface coverage for different deposition time.

Deposition Time (s)	**Charge Transfer Resistance, R_{ct} (ohm)**	**Electrolyte Resistance, R_s (ohm)**	**CPE, Q ($\mu F.s^{n-1}$)**	**Warburg Element, W (ohm. $s^{-0.5}$)**	**Surface Coverage $\theta(t)$ in %**
0 (Bare Au)	40.63	84.33	10.03	440.1	0
30	99.42	83.47	4.662	432.7	59.13297123 ± 2.38
60	115.1	86.97	6.46	462.9	64.70026064 ± 2.6
120	165.2	86.72	4.13	489.3	75.40556901 ± 3.01
240	196.5	83.35	4.214	484.1	79.32315522 ± 3.2
480	237.3	85.04	3.905	486.5	82.87821323 ± 3.41
960	279.5	85.77	3.402	485.5	85.46332737 ±3.61
1920	304.2	85.73	3.629	486.4	86.64365549 ± 3.87

Table 5.1: Surface Coverage for 0.5 mg/L PNIPAM with other circuit elements

From the Table 5.1, it can be said that nearly 60% surface coverage is achieved within a minute of polymer deposition as charge transfer resistance is increased significantly compared to the Bare Au. To see the change in the deposition rate and the surface coverage, the polymer solution is diluted 10 times to 0.05mg/L and then deposited gradually to the Au electrode. The EIS plot for the 0.05 mg/L polymer deposition is shown in Figure 5.11.

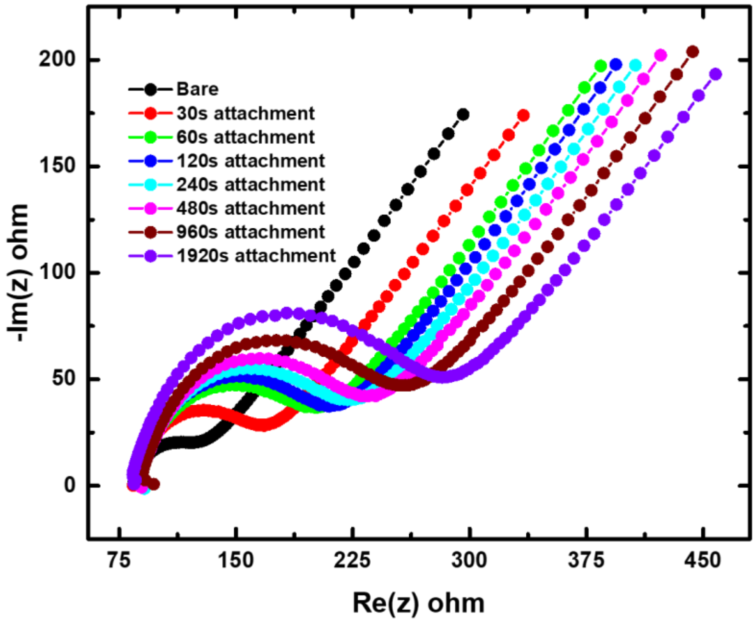

Figure 5.11: EIS curve for 100 mer 0.05 mg PNIPAM (with TCEP) attached to Au electrode

Table 5.2 presents the charge transfer resistance along with the gold surface coverage for 0.05 mg/L polymer attached gold surface. As expected, the surface coverage shows a decreased value compared to the previous 0.5 mg/L deposition.

Deposition Time (s)	**Charge Transfer Resistance, R_{ct} (ohm)**	**Electrolyte Resistance, R_s (ohm)**	**CPE, Q (μF.s^{n-1})**	**Warburg Element, W (ohm. $s^{-0.5}$)**	**Surface Coverage $\theta(t)$ in %**
0 (Bare Au)	40.63	84.33	10.03	440.1	0
30	78.63	83.71	6.307	438.1	48.32761033 ± 1.6
60	106.4	86.53	5.607	493.3	61.81390977 ± 2.52
120	115.3	86.52	4.661	495.6	64.76149176 ± 2.7
240	126	87.61	5.165	496.8	67.75396825 ± 3.01
480	135.6	88.98	4.581	508.1	70.03687316 ± 3.5
960	156	89.37	4.523	512.2	73.95512821 ± 3.7
1920	185.1	83.24	4.242	485.1	78.04970286 ± 3.85

Table 5.2: Surface Coverage for 0.05 mg/L PNIPAM with other circuit elements

From the EIS plot another important information, i.e. the impedance dependency on frequency can be extracted. Figure 5.12 and 5.13 plot |Z| vs f and – Phase(Z) vs f for 0.5 mg/L and 0.05 mg/L PNIPAM deposition on Au respectively. The impedance value is much higher at low frequency region (1Hz ~ 100Hz) compared to high frequency ranges.

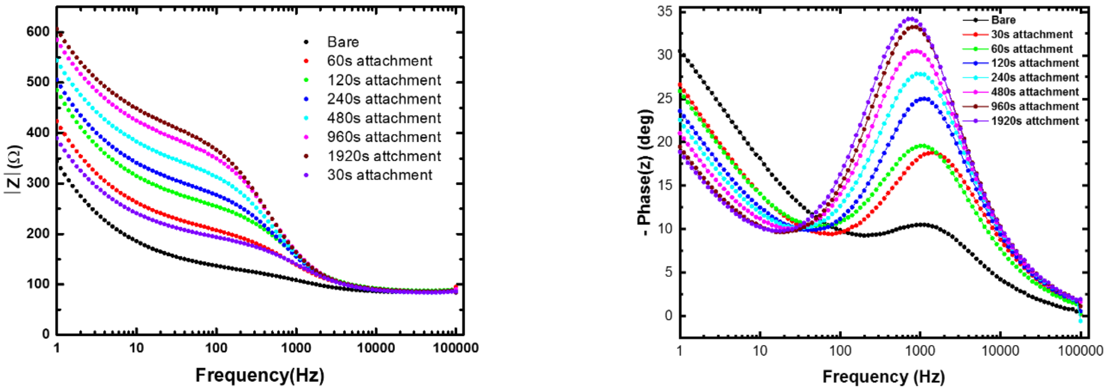

(a) **(b)**

Figure 5.12: (a) |Z| vs f curve and (b) - Phase(z) vs f curve for 100 mer 0.5 mg PNIPAM (with TCEP) attached to Au electrode

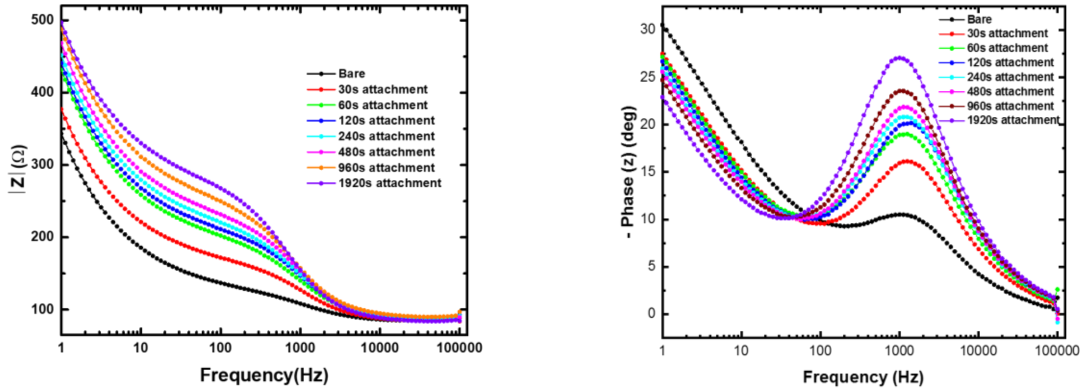

(a) **(b)**

Figure 5.13: (a) |Z| vs f curve and (b) - Phase(z) vs f curve for 100 mer 0.05 mg PNIPAM (with TCEP) attached to Au electrode

With gradual deposition for both polymer concentrations, the impedance shows a linear trend for both cases. The phase change due to frequency can be categorized into three regions: low frequency (1 ~ 100 Hz), mid frequency (100 ~ 10KHz) and high frequency (beyond 10 KHz) ranges. In the high frequency range, the plot is dominated by capacitive like elements, such as the polymer layer Constant Phase Element (*Q*). This is clear from the steady change in total impedance with frequency, and a correspondingly low phase value in Figures 5.12(a) and 5.13(b) (close to 0°, the phase response of a capacitor). Here, the impedance of the polymer CPE is less than that of the polymer resistance, and the resistor is effectively bypassed. Mid-frequency range depicts the resistive plateau, where the magnitude of the total impedance is varying nominally with frequency.

Here, the polymeric resistive path ($R_{ct}+W$) is the predominant factor in the impedance response, as the CPE is effectively shut off and the interfacial capacitance is still relatively small. The parallel combination of the polymeric resistive path ($R_{ct}+W$) and CPE gives rise to the characteristic semicircle seen in both Figure 5.9 and 5.11 Nyquist plots. Finally, the low frequency zone is the capacitive regime where the impedance is frequency dependent. The magnitude of the impedance increases due to the interfacial capacitance which models the processes such as the formation of the double layer capacitance at the electrode-polymer interface. This capacitance manifests itself in the Nyquist plot as a straight line at the end of the partial semicircle.

5.4 LANGMUIR-FREUNDLICH ISOTHERM

The PNIPAM surface coverages for the 0.5 mg/L and 0.05 mg/L polymer concentrations are compared in Figure 5.11. Both curves fit well with the Langmuir Freundlich isotherm which can be expressed as **Langmuir-Freundlich isotherm,** $\boldsymbol{\theta(t) = \frac{\theta_{sat} * k * t^{n}}{1+(k * t^{n})}}$

where, **θ(t)** is the surface coverage (%) , $\boldsymbol{\theta_{sat}}$ is the maximum surface coverage (%), **K** is the affinity constant for binding (L/mg), **n** is the index of heterogeneity.

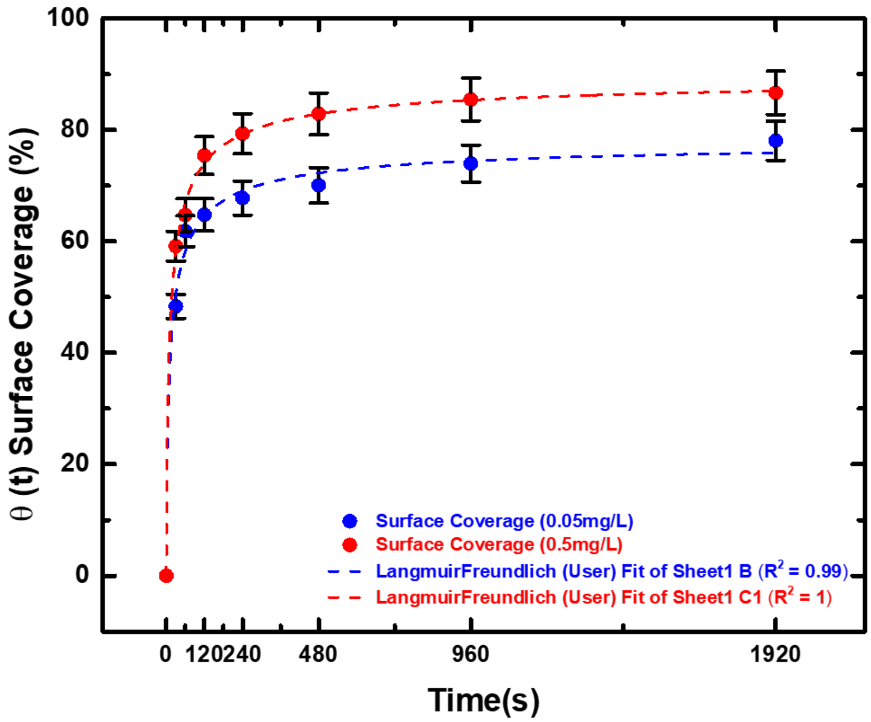

Figure 5.14: Surface Coverage for diluted PNIPAM (0.5 mg/L and 0.05 mg/L)

The Langmuir Freundlich isotherm is sometimes also referred to as the Sips equation [168]. It describes a specific relationship between the equilibrium concentration of bound polymer (θ) with respect to time (t) in a heterogeneous system with three fitting coefficients, θ_{sat}, K and n. K, the affinity constant for adsorption (L/mg) is related to median binding affinity (K_0) via $K_0 = K^{\frac{1}{n}}$ [169]. n is the heterogeneity index, which varies from 0 to 1. For a perfect homogeneous material, n = 1. When n < 1, the material is heterogeneous. In contrast to the heterogeneous Freundlich isotherm, the Langmuir Freundlich isotherm model has the advantage that it does not require an independent measure of the total number of binding sites (θ_{sat}), which is often impossible to measure in heterogeneous TPs. Figure 5.12 shows the Langmuir-Freundlich isotherm model fitted curve for impedance vs various deposition time and also shows that the goodness of fit is excellent ($R^2 = 0.99$).

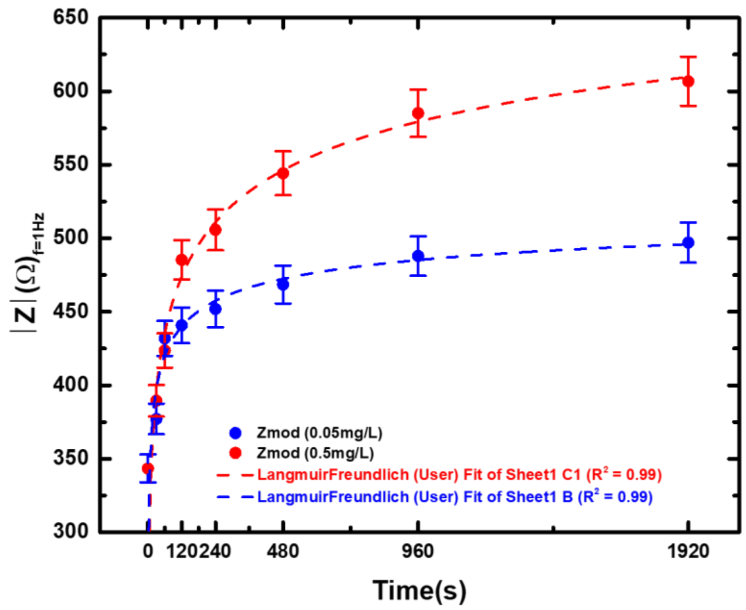

Figure 5.15: |Z| vs deposition time (at 1 Hz) for diluted PNIPAM (0.5 mg/L and 0.05 mg/L)

For Figure 5.15, the modified Langmuir-Freundlich isotherm can be written as

$$|\boldsymbol{Z}| = \frac{|\boldsymbol{Z_{sat}}| * \boldsymbol{k} * \boldsymbol{t^{n}}}{\mathbf{1}+(\boldsymbol{k} * \boldsymbol{t^{n}})}$$

where |Z| is the surface impedance, $|Z_{sat}|$ is the maximum surface impedance, K is the affinity constant for adsorption (L/mg), n is the index of heterogeneity.

The Langmuir-Freundlich isotherm has been effective in displaying the adsorption characteristics of numerous heterogeneous frameworks, including gas adsorption onto surfaces [170], [171], ligand proclivity to polyclonal antibodies [172], and adsorption of metal particles to ecological samples [173].

5.5 APPARENT RATE CONSTANT

The estimation of the heterogeneous electron transfer rate constant is of critical importance when it comes to analyzing binding characteristics. The rate constant indicates the electron movement between an electroactive species and the electrode surface, regardless of whether the electrode material decides the general rate of the electrochemical response and could even be utilized to assess the allotrope of the material being referred to. Electrochemical Impedance Spectroscopy (EIS) is a technique which can quantify k_0 values for charge transfer reactions and the charge transfer resistance, R_{CT} reflects the charge transfer kinetics at the solution-electrode interface is related to the faradic current by the following expression:

$$R_{ct} = \frac{R\,T}{n\,F\,A\,I_0}$$

where,

$$I_0 = n\,F\,A\,K_{app}\,C$$

R_{ct} = Charge Transfer Resistance

R = Universal Gas Constant

T = Temperature in Kelvin

I_0 = Exchange Current Density

n = Number of Electron Transfer

C = Concentration of analyte or redox element

A = Geometrical Area

All the above mentioned expressions [174], [175] are really important for calculating rate constant. The apparent rate constant Kapp can be expressed as

$$K_{app} = \frac{R\,T}{n\,F^2\,C\,A\,R_{ct}} \quad [176]$$

For calculation of K_{app} , the following constant parameters have been used:

Universal Gas Constant, R = 8.314 J/K.mol

Faraday's Constant, F = 96485.33 s.A/mol

Room temperature in kelvin, T = 298K

Number of electron transfer, n= 1

Concentration of ferro-/ferri cyanide solution, C = 5 mM=0.000005 mol/cm3

Au electrode surface area, A=0.0701cm^2

The apparent rate constants for both 0.5 mg/L and 0.05 mg/L PNIPAM deposition on gold electrode is shown in Table 5.3.

Time (s)	Kapp (0.5mg/L) cms^{-1}	Kapp (0.05mg/L) cms^{-1}
0	0.01869 ± 0.001308	0.01869 ± 0.013457
30	0.00764 ± 0.000535	0.00966 ± 0.006955
60	0.0066 ± 0.000462	0.00714 ± 0.005141
120	0.0046 ± 0.000322	0.00659 ± 0.004745
240	0.00386 ± 0.00027	0.00603 ± 0.004342

480	0.0032 ± 0.000224	0.0056 ± 0.004032
960	0.00272 ± 0.00019	0.00487 ± 0.003506
1920	0.0025 ± 0.000175	0.0041 ± 0.002952

Table 5.3: Calculated apparent rate constant for both 0.5mg/L and 0.05mg/L cases.

Figure 5.13 plots the apparent rate constants for both 0.5 mg/L and 0.05 mg/L of PNIPAM concentration when deposited on a gold electrode. Both curves were fitted ($R^2 = 0.99$) with a second order exponential decay function, $y = A_1e^{(-x/t1)} + A_2e^{(-x/t2)} + y_0$

For 0.5 mg/L deposition,

$$y_0 = 0.00266 \pm 2.32505E\text{-}4$$

$$A_1 = 0.00914 \pm 0.003$$

$$t_1 = 18.86156 \pm 10.48099$$

$$A_2 = 0.00461 \pm 0.00203$$

$$t_2 = 179.01992 \pm 93.42105$$

For 0.05 mg/L deposition,

$$y_0 = 0.00358 \pm 4.52461E\text{-}4$$

$$A_1 = 0.01197 \pm 2.0705E\text{-}4$$

$$t_1 = 21.43787 \pm 0.95444$$

$$A_2 = 0.00315 \pm 3.76291E\text{-}4$$

$$t_2 = 1072.27912 \pm 351.23399$$

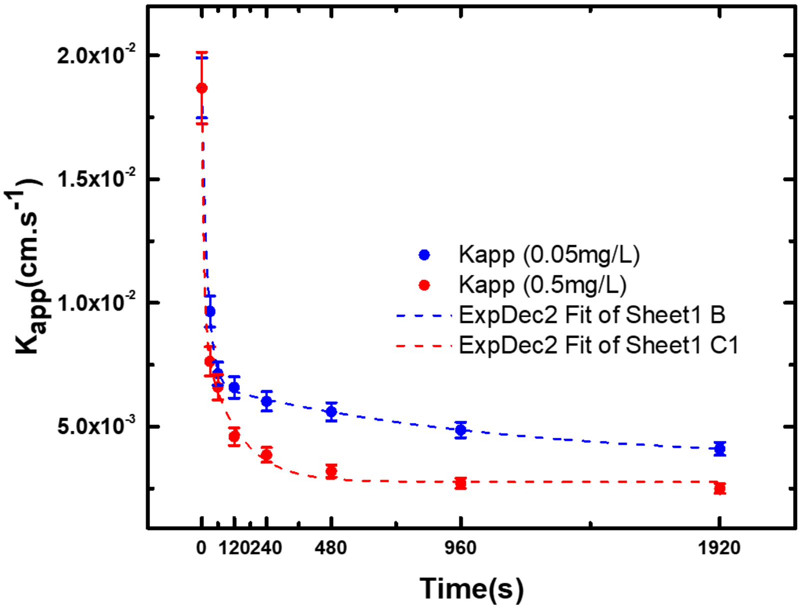

Figure 5.16: K_{app} vs deposition time for diluted PNIPAM (0.5 mg/L(blue) and 0.05 mg/L(red))

From the rate constant plot it is evident that the initial (0 ~ 60s) rate constants are similar for both 0.5 mg/L and 0.05 mg/L concentrations and in the mid region (60s ~ 720s) the value of K_{app} for 0.05 mg/L is comparatively larger and after 960s the K_{app} quickly saturates for both cases.

CHAPTER 6: DETECTION OF NITROPHENOL

6.1 OVERVIEW

Nitrophenol isomers usually coexist in natural and ecological samples, which are essential organic compounds in industrial, agricultural and defense applications. These synthetic compounds are frequently utilized as intermediates in the manufacturing of explosives, pharmaceuticals, pesticides, dyes, elastic synthetic concoctions and fungicides and so forth. Phenols-based aromatic nitro compounds are considered anthropogenic toxins, which can cause irreversible harm to animals and plants even at low concentration [177]. Traditional wastewaters and water refinement plants experience issues disposing of these substances, as they require specific treatments with long incubation periods because of their high stability and solubility in water [178]. In addition, 4-NP is a typical intermediate for the generation of analgesics, leather products, colors, and pharmaceuticals. It is additionally perceived as a toxin, which will in general stay in agricultural products, vegetables, organic products, or water sources when utilized as a fixing in composts or pesticides [179], [180].

Therefore, it is essential to develop a fast, selective, sensitive and low-cost sensor to measure the nitrophenol content quantitively in freshwater, wastewater, or marine conditions. Different techniques have been developed to detect phenols in a sample solution, such as chromatography [181], capillary electrophoresis [182], spectrophotometry [183] and electrochemical techniques [184], [185]. However, these techniques each have their very own limitations. For example, Chromatography, capillary electrophoresis and spectrophotometry require a complex and tedious sample pretreatment process. Furthermore, these instruments are costly and a long investigation time are often involved, which make them inappropriate for routine examination.

Electrochemical sensors offer array of opportunities for performing on-site examination at low cost with quick and reliable outcomes. Unfortunately, there are several challenges that needed to be addressed e.g., interferents, and electrode fouling. Furthermore, if a conventional electrode is utilized as an electrochemical detector or transducer, the overpotential is high and the sensing selectivity is poor [186]. Hence, much effort has been directed at creating a sensor that exhibits high selectivity. Recently, work has been done in electrochemical detection of various nitrophenol species depending on the surface alteration of sensor electrode. Some examples include chitosan–ZnO nano-needles [187] poly(p-aminobenzene sulfonic corrosive) films [188] , and graphene oxide particles modified with chitosan and cyclodextrine [189]. A few intriguing investigations on the oxidation and reduction of 4-NP have been reported that utilize electrodes such as modified with nanomaterials, carbon nanotubes (CNTs), ordered mesoporous carbons, glassy carbon electrode (GCE), graphene, fullerene-b-cyclodextrin, poly (methylene blue), silver nanoparticles, and nano porous gold [190]–[197].

Additionally, templated polymers (TPs) are polymeric materials that can be modified to exhibit high selectivity towards target molecules and are generally used in sensing and catalyst platform [198], [199]. Surface alteration of electrodes in electrochemical sensors by immobilization of recognition elements is an effective way to deal with get a high authoritative of target compound with great selectivity. This thesis discusses Reversible Addition-Fragmentation chain Transfer (RAFT) technique to establish highly selective fast polymer-based electrochemical sensing platform. Such platform would enhance the sensitivity as well as the reaction time. Once the templates are completely removed from polymeric chain, the synthetic target receptors are attached onto the gold electrode, forming a flexible continuous brush like monolayer structure.

During analyte detection, when the target (4-Nitrophenol) binds to the synthetic receptor, the conformation of the polymer changes which can be estimated electrochemically.

To enhance the affinity between polymer receptor and 4-nitrophenol, 4-vinylpyridine (4VP) monomer was incorporated [200]. Previous reports suggested that 4VP is a better recognition monomer for 4-nitrophenol format than Methacrylic Acid (MAA). [201], [202]. The non-covalent crosslinks utilized by acid-base can be joined into the TP system to accomplish high binding cavity without a high level of covalent crosslinking. Nakayama's work has demonstrated that it is conceivable to accomplish this with hydrophobic cooperation. A less rigid bond can be made by presenting a sort of electrostatic cooperation between monomers that will enable the TP to be available as a solute in an aqueous domain.

6.1 ELECTROCHEMICAL RESULTS OF 4-NITROPHENOL (4NP) BINDING

Figure 6.1 shows cyclic voltammetry plot for TP (template removed) attached Au electrode and Au electrode after exposure to different concentration of 4NP. The electrochemical measurements were taken in 5 mM ferro-ferri cyanide electrolyte. Polymer attachment was carried out for 2 minutes. Then the polymer attached electrode was exposed to different concentration of 4NP. CV peaks are distinguishable for concentrations higher than 5µM 4NP. The peak values gradually fell due to blockage of charge transfer path from bulk electrolyte solution to gold electrode surface. For analysis, the sensing of 4NP was based on impedimetric technique, also known as EIS. In impedimetric sensing, changes in current, resistance or impedance upon the binding of target species (hybridization) as well as conformational changes of the polymeric receptor can be monitored.

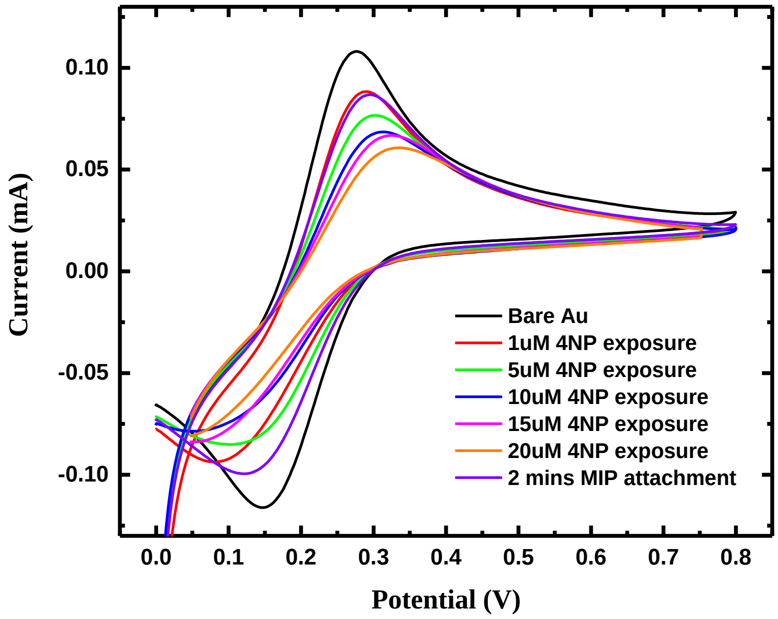

Figure 6.1: CV curve for 4NP attachment

EIS measurements were employed to determine the changes that occurred during the modification of the Au electrode. Figure 6.2 shows the Nyquist plots of $[Fe(CN)_6]^{3-/4-}$ for the bare Au electrode, TP (template removed) attached Au electrode and modified Au electrode with different 4NP concentrations.

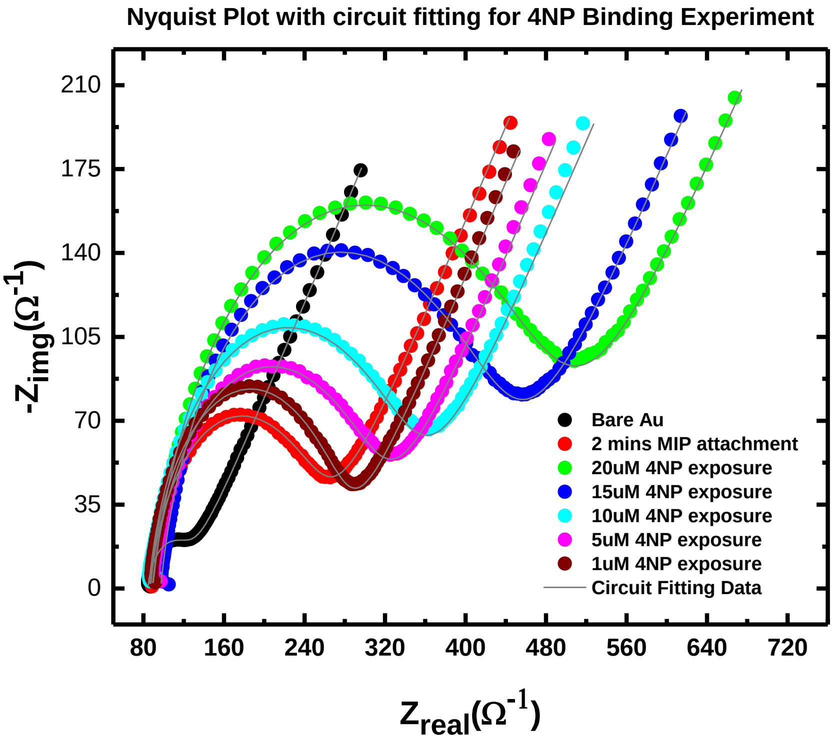

Figure 6.2: EIS curve for 4NP attachment

The bare Au electrode shows a small semicircle domain in comparison to the modified Au electrode with TP attached and exposed with 4NP, which is characteristic of a smaller charge transfer resistance (R_{ct}). This represents polarization resistance at equilibrium potential, and hence a faster electron transfer [203]. The increased polarization resistance of the TP (template removed) attached Au electrode (purple curve) is possibly due to two factors; the first is due to the blocked path for electron transfer between $[Fe(CN)_6]^{3-/4-}$ in the electrolyte and Au surface, and the second is due to the negative charges of the polymer backbone which may cause an electrostatic repulsion to the negative redox couple $[Fe(CN)_6]^{3-/4-}$ anions. Due to this repulsion force, the anions present in electrolyte face a greater blockage to reach the Au surface. The R_{ct} values corresponding 4NP exposed TP (template removed) attached Au show a linear increment (orange, magenta, blue, green and red) with respect to increased concentration of 4NP which suggest increasing 4NP molecules are bounded to the polymer backbone.

EIS or Nyquist plots are fitted with modified Randle's Circuit model shown in Figure 6.3. Circuit parameters are extracted and shown in Table 6.1.

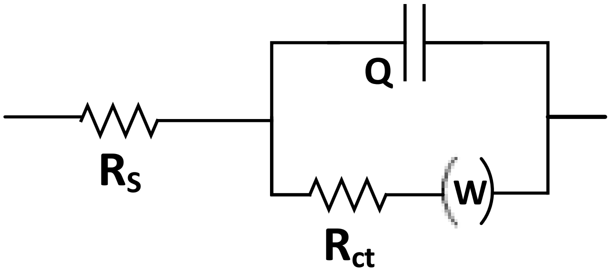

Figure 6.3: EIS Circuit model to fit Nyquist plot

Samples	**Electrolyte Resistance, R_S (Ω)**	**Charge Transfer Resistance, R_{ct} (Ω)**	**CPE, Q (μF.s^{n-1})**	**Warburg Element, W (Ω. $s^{-0.5}$)**	**Exponent, n_1**
Bare Au	84.33 ± 4.2165	40.63 ± 1.82835	10.03±0.1	440.1±0.9	0.8697±0.5
0 µM 4NP	86.7±0.2	165.2±0.7	4.1±0.2	489±1.2	0.87±0.5
1 µM 4NP	86.9±0.2	180.5±0.6	3.6±0.2	453±1.0	0.90±0.5
5 µM 4NP	88.7±0.2	219.6±0.7	4.1±0.2	464±1.3	0.86±0.5
10 µM 4NP	86.1±0.2	275.4±0.7	4.4±0.1	479±1.4	0.86±0.5
15 µM 4NP	87.0±0.2	333.2±0.7	4.7±0.1	487±1.6	0.86±0.5
20 µM 4NP	88.9±0.2	391.6±0.7	5.5±0.1	506±1.7	0.84±0.5

Table 6.1: Equivalent circuit parameters for TP attachment and 4NP binding

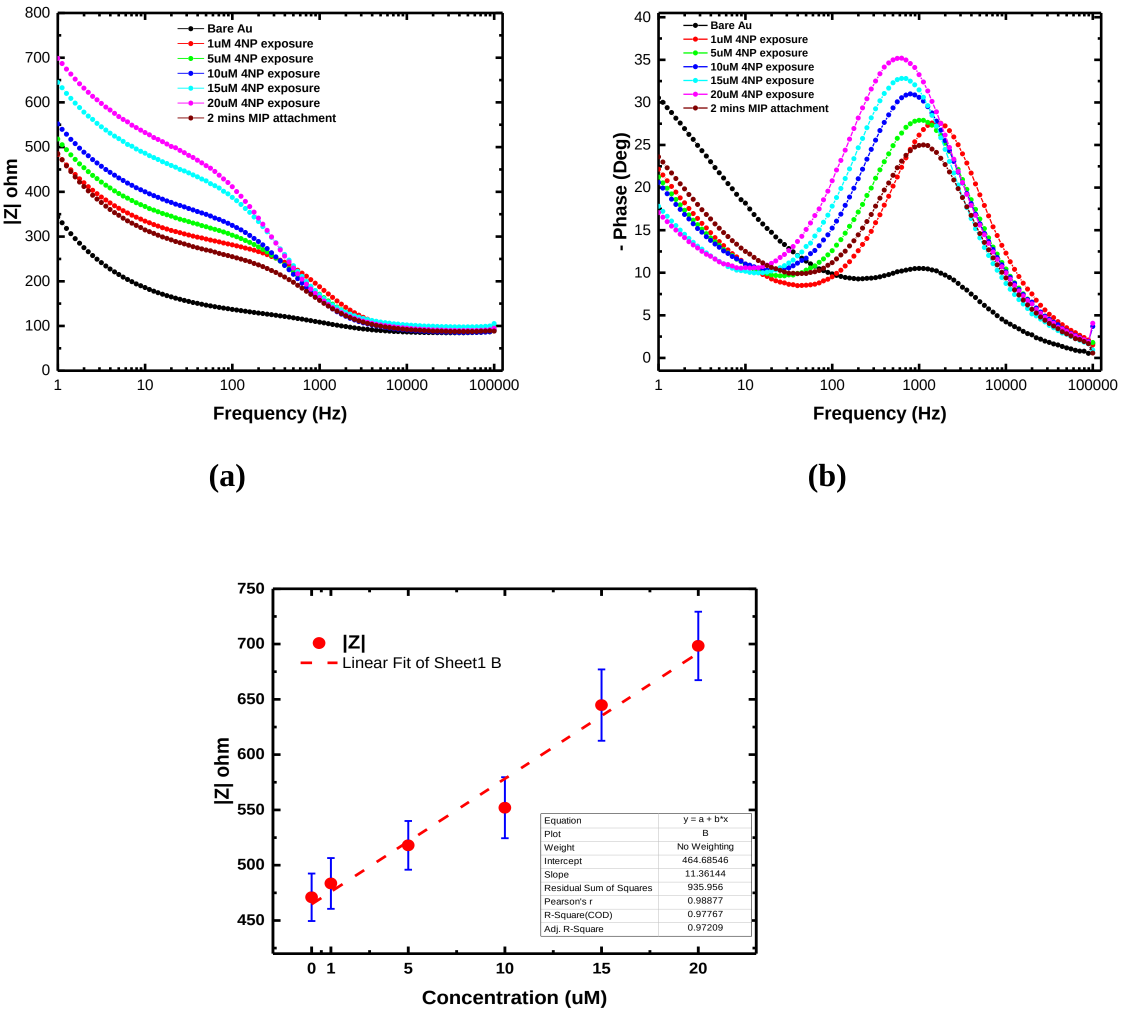

Equation	y = a + b*x
Plot	B
Weight	No Weighting
Intercept	464.68546
Slope	11.36144
Residual Sum of Squares	935.956
Pearson's r	0.98877
R-Square(COD)	0.97767
Adj. R-Square	0.97209

(a) **(b)**

(c)

Figure 6.4: (a) |Z| vs f curve and (b) -Phase(Z) vs f curve for 4NP attachment

(c) Linear increment of |Z|

Figure 6.4 (a) and (b) show the change in impedance magnitude and phase respectively after TP (template removed) attachment and 4NP exposure. The impedance magnitudes gradually increase upon TP attachment and with increasing 4NP exposure. The plot of Figure 6.4 (c) shows the linear increment trend (R^2=0.97) in terms of |Z|. In the phase plot in Figure 6.4 (b), the phases at the lowest frequency, i.e. 1 Hz shows the phases are in between -17° and -23° for the polymer attached gold surface and after 4NP exposure. The phase angle is resistive (~0°) at high frequencies (~10^5 Hz), then changes to significant negative values when the impedance becomes partially capacitive at medium frequencies (~10^3 Hz) and becomes again partially resistive at low frequencies. The phase drops from -23° (template removed polymer attached surface) to -17°(highest concentration of 4NP exposed to polymer attached surface) suggest template binding.

6.3 SELECTIVITY CHARACTERIZATION

To characterize the receptor's selectivity, the sensor was exposed to 3NP, an isomer of 4NP. Figure 6.5 and 6.6 show CV and EIS plot for TP attached and modified electrode after 3 NP exposure, respectively. The CV peaks show a continuous increment with 3NP exposure though the trend is not linear. On the other hand, the Nyquist plot shows a decrement in impedance. Interestingly, 3NP exposed electrode shows comparatively shorter diffusion tail compared to 4NP exposed electrode that suggests much less 3NP is binding with the polymer network and thus conformational change is minimal.

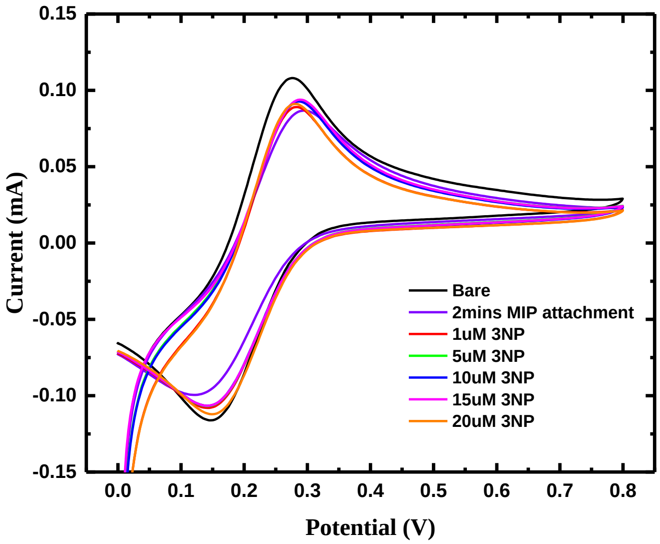

Figure 6.5: CV curve for 3NP attachment

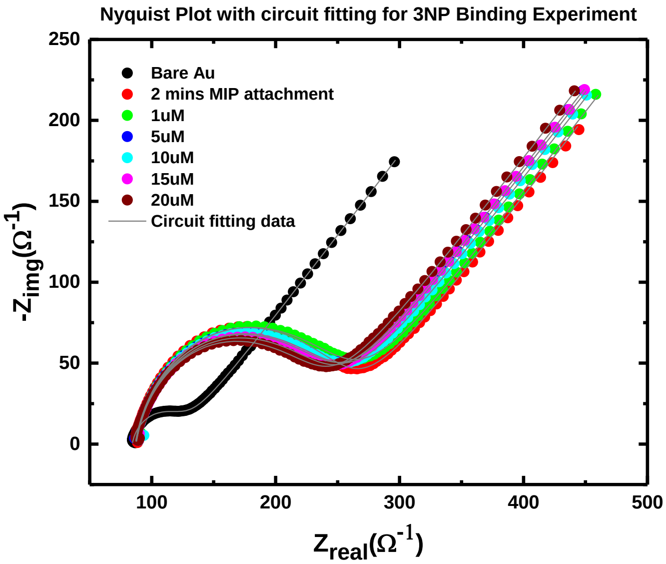

Figure 6.6: EIS curve for 3NP attachment

The parameters of EIS plot in Figure 6.6 can be fitted to the circuit shown in Figure 6.7.

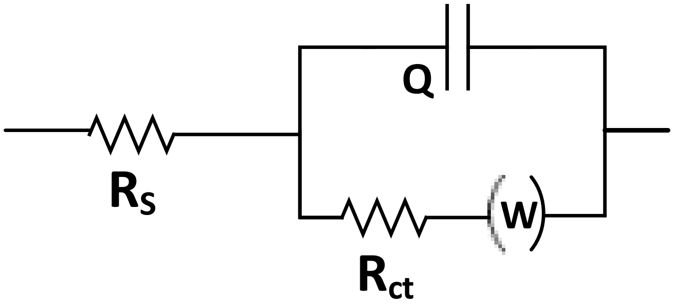

Figure 6.7: EIS Circuit model to fit Nyquist plot

Table 6.2 shows the circuit parameters for the circuit fitting model 3NP sensing.

Samples	**Electrolyte Resistance, R_s (ohm)**	**Charge Transfer Resistance, R_{ct} (ohm)**	**CPE, Q ($\mu F.s^{n-1}$)**	**Warburg Element, W (ohm. $s^{-0.5}$)**	**Exponent, n_1**
Bare Au	84.33 ± 7.5897	165.2±0.7	4.1±0.2	489±1.2	0.87±0.5
0 μM 3NP	86.7±0.2	163.3±0.8	4.9±0.3	536±1.3	0.87±0.5
1 μM 3NP	87.3±0.2	152.8±0.8	4.9±0.3	543±1.3	0.87±0.5

5 µM 3NP	87.0±0.2	154.5±0.8	5.0±0.3	537±1.3	0.87±0.5
10 µM 3NP	87.3±0.2	149.3±0.8	4.9±0.3	546±1.3	0.87±0.5
15 µM 3NP	87.1±0.2	147.3±0.8	5.0±0.3	544±1.2	0.87±0.5
20 µM 3NP	86.9±0.2	165.2±0.7	4.1±0.2	489±1.2	0.87±0.5

Table 6.2: Equivalent circuit parameters for TP attachment and 3NP binding

The change in R_{ct} from 0 µM to 20 µM in the case of 3NP is not significant compared to the 4NP binding case.

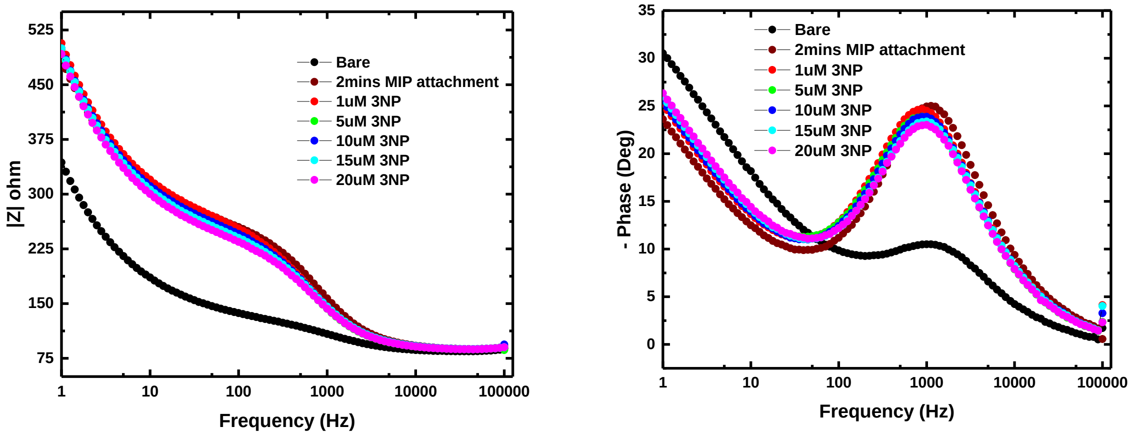

(a) **(b)**

Figure 6.8: (a) |Z| vs f curve and (b) Phase(Z) vs f curve for 3NP attachment

Figure 6.8 (A) and (B) plots the magnitude and the phase spectra of the modified electrode after polymer attachment and 3NP exposure respectively. The impedance magnitudes are quite packed in between 480 and 520 ohms at 1Hz frequency compared to 4NP sensing. Such high impedance values indicate poor conductivity i.e. low binding affinity.

6.4 SENSOR SELECTIVITY

Figure 6.9 illustrates the non-specific adsorption phenomenon for both analyte, 4NP and 3NP. For the proposed system, the Rct value is similar for Bare Au electrode, after 4NP and 3NP exposed electrodes which suggest negligible non-specific adsorption for short exposure time.

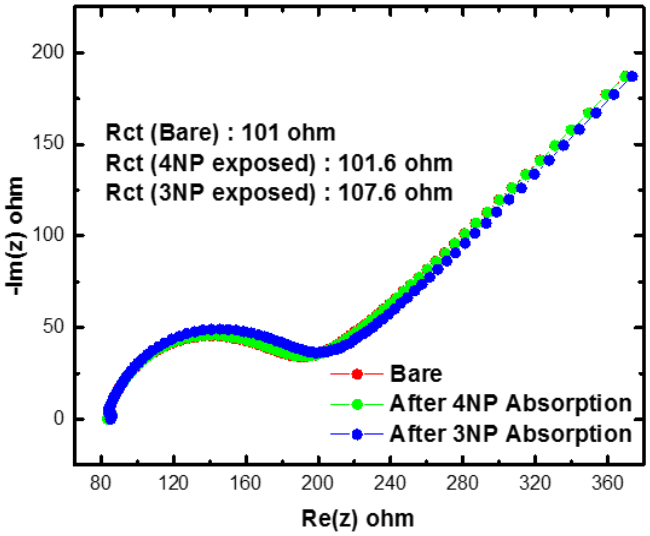

Figure 6.9: Nonspecific absorption for 4NP and 3NP

Figure 6.10 illustrates the electroactive nature of 4NP. The experiment was performed in 1X PBS and hence no redox element was present.

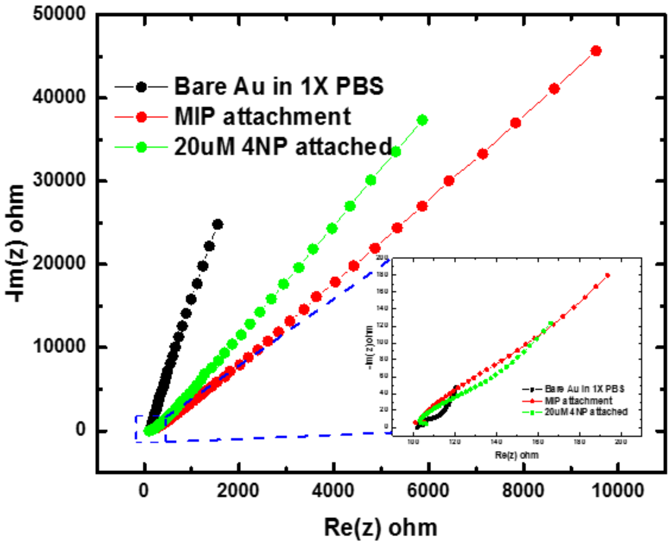

Figure 6.10: EIS curve for 4NP attachment (in 1X PBS)

The sensing calibration curve is found plotting the association constant from charge transfer resistance, $K_a = \left|\frac{R_{ct,n\mu M} - R_{ct,0\mu M}}{R_{ct,0\mu M}}\right|$ vs concentration of 4NP and 3NP. Here, $R_{ct,n\mu M}$ is the charge transfer resistance calculated from the equivalent circuit in Figure 6.7 upon nitrophenol exposure to modified electrode. $R_{ct,0\mu M}$ is the charge transfer resistance after TP attachment to the Au electrode. The increasing value of K_a indicates that more template is bounded to the polymer from the initial condition. Figure 6.11 plots both calibration curves for 4NP and 3NP sensing results. Clearly, the slope of 4NP binding calibration curve shows steeper response compared to 3NP binding system which suggests the template 4NP binds better than 3NP.

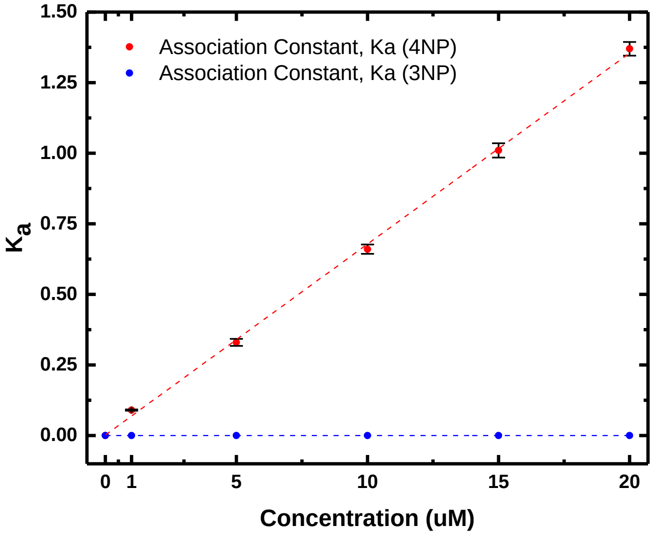

Figure 6.11: Calibration curve in terms of association constant (K_a) from charge transfer resistance for 4NP & 3NP attachment

In Figure 6.12, the apparent rate constants for 4NP and 3NP are plotted. In case of 4NP binding, the apparent rate constant decreases with the increasing 4NP concentration which suggest more blockage of electron transfer between the bulk electrolyte solution and gold electrode surface.

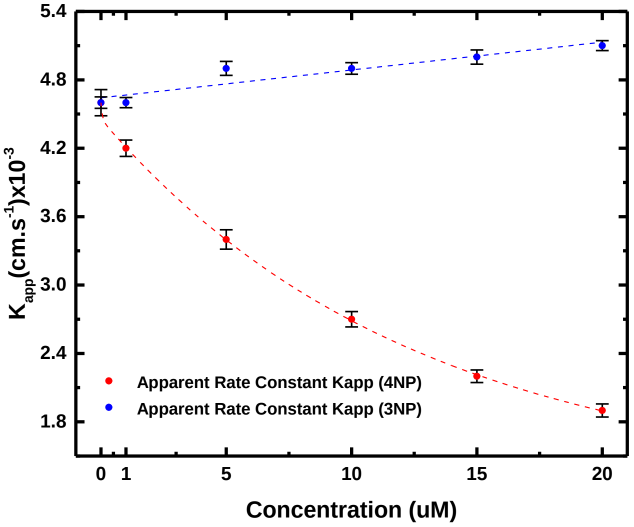

Figure 6.12: Calibration curve in terms of apparent rate constant (K_{app}) for 4NP & 3NP attachment

CHAPTER 7: DETECTION OF GLUTAMATE

7.1 OVERVIEW

Glutamate is an amino acid which exists in principle part of numerous proteins and peptides and a key neurotransmitter in the central nervous system. Glutamate is produced in the body, utilized in the biosynthesis of proteins and assumes a fundamental job in human digestion It is a vital excitatory neuro signal in the human brain. It also plays a critical role in many neurological disorders such as Parkinson's, Schizophrenia and Alzheimer's disease [204]. Glutamate released or absorbed at excitatory synapses are essential to many aspects of normal brain functioning. Extracellular glutamate in the synaptic cleft can prompt over the top calcium passage, which is the fundamental driver of neuronal damage such as stroke and cerebral hypoxia/ischemia [205].

Enzyme based electrochemical detection is a typical detection approach for non-electroactive nature of certain analyte like glutamate. However, enzyme-based biosensors can be costly because of the manufacturing cost and faces chemical degradation over the time results lack of stability. As a result, more straightforward techniques for example, non-enzymatic biosensors have been considered recently.

Because of the fast reaction time, compactness, real-time quantitative analysis capability, electrochemical sensing is a popular method for detecting glutamate when compared with other sensing mechanisms, for example, spectrophotometric, chromatographic, fluorescence, and slim electrophoresis procedures. Accomplishing a quick and sensitive detection of glutamate using of novel nanomaterial-based sensor has been the subject a subject of research in recent years [206].

Voltammetric sensor depends on the analyte's redox activity, if other interfering redox active chemical species present in electrolyte solution then it might be difficult to distinguish between signal due to analyte and interfering species. One effective approach is to use molecular imprinted polymer for improving the target selectivity [188]. Molecularly imprinted polymers based biosensing platforms have been utilized for various chemical species. The imprinting of biomolecules including pharmaceuticals, pesticides, amino acids, peptides, nucleotide bases, steroids and even metals and different particles have shown to support the specific association in the imprinting network. Generally, molecularly imprinted polymers were based on highly crosslinked polymer matrix with molecular cavities that serve as target receptors. In this system, the analyte must infiltrate through the polymer layer to access the binding sites. Moreover, highly crosslinked polymer-based receptors in general are rigid, further hindering the binding and release of the target molecule.

7.2 N-METHYL-GLUTAMATE SENSING

The electrode preparation and electrochemical measurement for N-Methyl-Glutamate is like the 4NP sensing experiment as discussed in earlier chapters. The template removed TP was first attached to the electrode and then was exposed to different concentrations of N-Methyl-Glutamate. A distinguishable increment in the R_{ct} was observed with increasing N-Methyl-Glutamate concentration. A Nyquist plot for the EIS measurements to different concentrations of N-Methyl-Glutamate along with TP attachment is displayed in Figure 7.1. The plot suggests that there is a correlation between N-Methyl-Glutamate concentrations and the R_{ct} values. The diffusion tail in the curve is nearly vanished around after 300nM of N Methyl Glutamate was exposed to the sensor. This proportional increment in R_{ct} suggests that the proposed framework can quantitatively detect target analyte, in this case, N-Methyl-Glutamate.

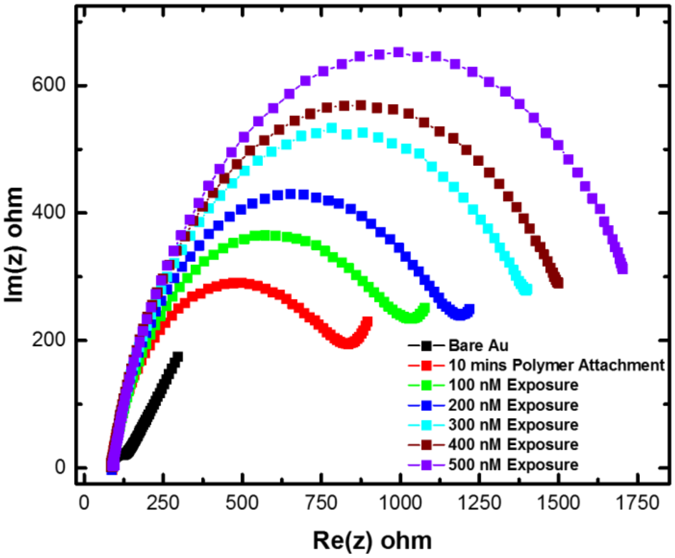

Figure 7.1: Nyquist curve for N-Methyl-Glutamate attachment

The Nyquist plot data is fitted with modified Randle's circuit shown in Figure 7.2 which is similar earlier mentioned circuit. Table 7.1 presents the important circuit parameters extracted from the EIS circuit fit.

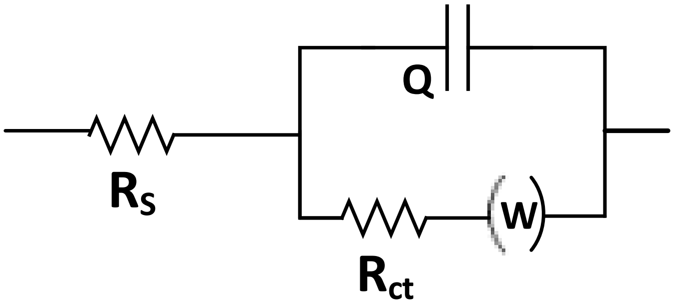

Figure 7.2: Equivalent Circuit for N-Methyl-Glutamate attachment

Samples	**Electrolyte Resistance, R_s (ohm)**	**Charge Transfer Resistance, R_{ct} (ohm)**	**CPE, Q ($\mu F.s^{n-1}$)**	**Warburg Element, W (ohm. $s^{-0.5}$)**	**Exponent n_1**
Bare Au	84.33	40.63 ± 1.665	10.03	440.1±16.943	0.8697
0 nM N Methyl Glutamate	86.88	689 ± 28.249	12.63	483.3±18.607	0.8444
100 nM N Methyl Glutamate	88.45	881.1 ± 36.125	14.03	478.3±18.414	0.8382
200 nM N Methyl Glutamate	85.71	1043 ± 42.763	11.93	445.8±17.163	0.8402
300 nM N Methyl Glutamate	88.86	1268 ± 51.988	11.66	459.2±17.679	0.8429
400 nM N Methyl Glutamate	86.25	1383 ± 56.703	11.38	456.6±17.579	0.8386
500 nM N Methyl Glutamate	91.33	1600 ± 65.6	10.26	464.9±17.898	0.8324

Table 7.1: Equivalent circuit parameters for TP attachment and N Methyl Glutamate binding

The charge transfer resistance R_{ct} is found to be approximately 689 Ω for TP attached gold surface and linearly increases with the concentration of N Methyl Glutamate and 1600 Ω is measured for the highest N Methyl Glutamate concentration exposure. Higher R_{ct} suggest that more Au surface is being blocked and less electron transfer between Au and electrolyte.

Figure 7.3 (A) and (B) display the impedance magnitude and phase plot for the system, respectively. The inset of Figure 7.3 (A) indicates linear increment of impedance magnitude upon polymer attachment and template binding. The lower frequency (f < 100 Hz) domain at the magnitude plot shows lower shunt capacitance upon the polymer attachment and further binding of higher concentrations of analyte to the polymer backbone. In the low frequency zone i.e., 1 ~ 100 Hz, the impedance response is capacitance dominated and beyond 100 Hz, it is dependent on the resistive parameter.

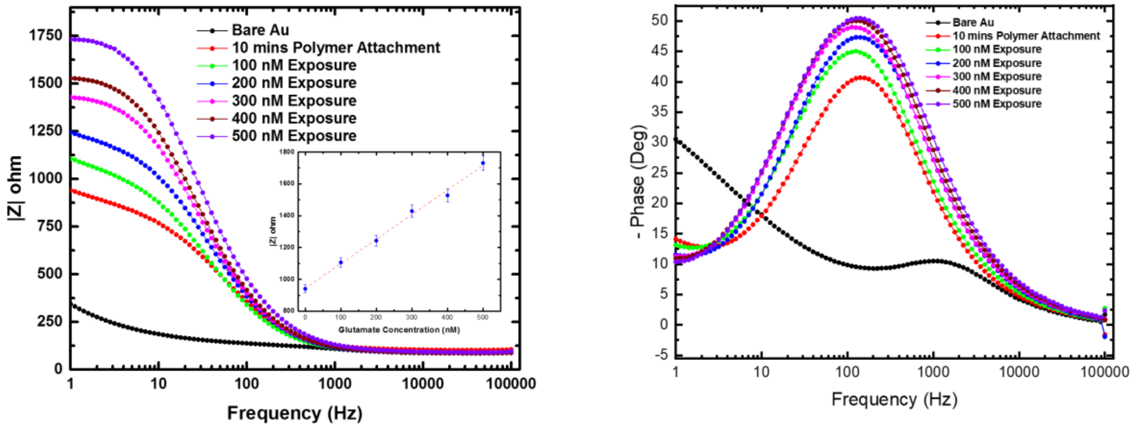

(A) **(B)**

Figure 7.3: (A) |Z| vs f curve and (B) -Phase(Z) vs f curve for N Methyl Glutamate attachment

The conformational change (from an extended to a folded state) of the single-chain templated polymer contributes towards the change in phase as shown in Figure 7.3 (B).The maximum angular phase obtained from the phase plot around 60 Hz in the lower frequency domain (f < 100 Hz) has proportionally increased upon N Methyl Glutamate binding.

7.3 L GLUTAMIC ACID SENSING

An effective electrochemical sensor should not only be sensitive to the target molecule, but also selective for that species. The selectivity of the TP is surveyed by exposing the N Methyl Glutamate templated polymer to L Glutamic Acid. The EIS data are plotted in Figure 7.4. The data are fitted with the same equivalent circuit as shown in Figure 7.2. Circuit parameters are extracted and tabulated in Table 7.2.

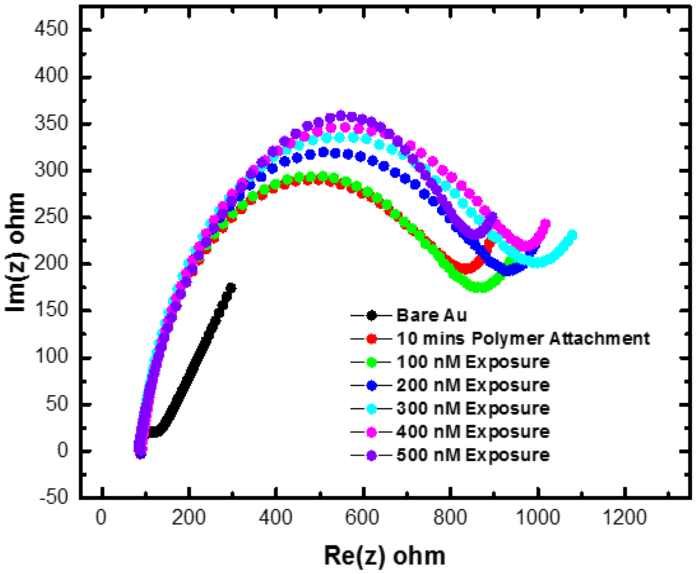

Figure 7.4: EIS curve for L Glutamic acid attachment

Table 7.2: Equivalent circuit parameters for TP attachment and L Glutamic Acid binding

Samples	**Electrolyte Resistance, R_s (ohm)**	**Charge Transfer Resistance, R_{ct} (ohm)**	**CPE, Q (μF.s^{n-1})**	**Warburg Element, W (ohm. $s^{-0.5}$)**	**Exponent n1**
Bare Au	84.33	40.63±2.539	10.03	440.1±24.205	0.8697
0 nM L Glutamic Acid	88	689±43.062	12.63	483.3±26.581	0.8444
100 nM L Glutamic Acid	86.22	723.5±45.218	9.689	471±25.905	0.8394

200 nM L Glutamic Acid	84.31	788.9±49.306	10.36	478.2±26.301	0.8331
300 nM L Glutamic Acid	83.34	851.3±53.206	10.86	478±26.29	0.8245
400 nM L Glutamic Acid	89.27	820.5±51.281	12.43	483.2±26.576	0.8463
500 nM L Glutamic Acid	86.78	861.6±53.85	13.99	486.1±26.735	0.8381

The change in R_{ct} shows minimal correlation with L-Glutamic Acid concentrations compared to previously discussed N-Methyl-Glutamic acid sensing experiment.

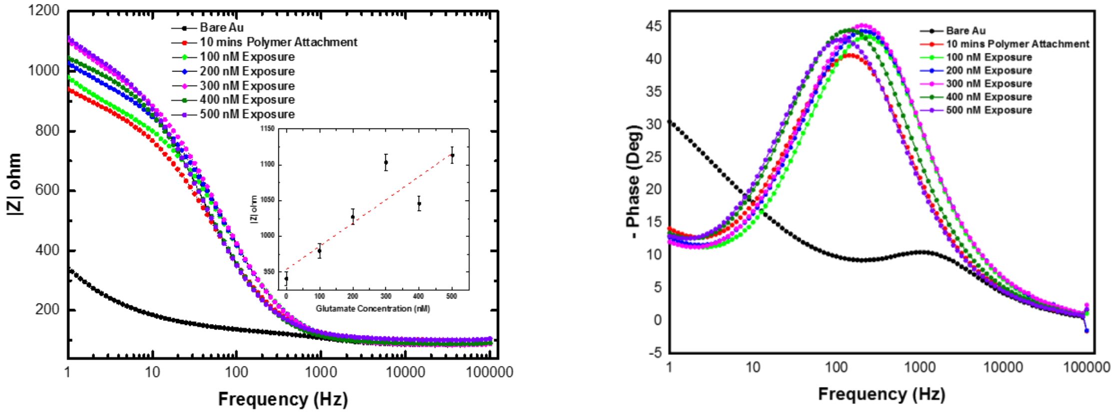

(a) **(b)**

Figure 7.5: (a) |Z| vs f curve and (b) -Phase(z) vs f curve for L Glutamic acid attachment

Figure 7.4 (A) and (B) shows the magnitude and phase plot for the L Glutamic Acid selectivity test. It is evident that change in impedance magnitude and phase displacement upon L-Glutamic Acid exposure TP attachment and target exposure is not significant compared to N Methyl Glutamate sensing data. The inset in Figure 7.4 (A) shows that the data points significantly deviate from the linear trend.

7.3 SENSOR SELECTIVITY

Figure 7.6 presents the sensing calibration curves for both N-Methyl-Glutamate (Red dotted line) and L-Glutamic Acid (Blue dotted Line). Both fitted curves show linear trend however the data points for N-Methyl-Glutamate follow a closer linear trend. The R^2 value for N-Methyl-Glutamate ($R^2 = 0.99$) is greater than that of the L-Glutamic-Acid ($R^2 = 0.86$). It also tells N Methyl Glutamate binding data has better goodness of fit with the trend line.

$\frac{R_{ct}}{R_{ct0}}$ gives the ratio between charge transfer resistance after glutamate analog binding and without any bound target.

$\frac{R_{ct}}{R_{ct0}} - 1$ gives the numerical condition of binding, where 0 means no analyte is bound with the polymer backbone. The value linearly increases with concentration of Glutamate analogs.

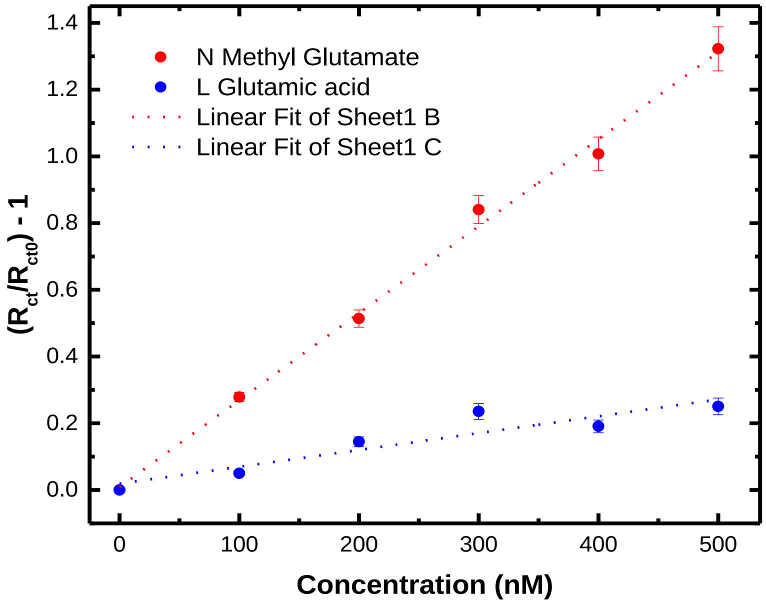

Figure 7.6: Calibration curve for N Methyl Glutamate and L Glutamic acid attachment

Linear regression parameters for N Methyl Glutamate calibration curve:

Equation	y = a + b*x
Plot	N Methyl Glutamate
Weight	No Weighting
Intercept	0.00876 ± 0.02544
Slope	0.00261 ± 8.40313E-5
Residual Sum of Squares	0.00494
Pearson's r	0.99793
R-Square(COD)	0.99586
Limit of detection for N Methyl Glutamate sensing: 11.06 nM	

Table 7.4: Curve fitting parameter for N Methyl Glutamate Sensing

Linear regression parameters for L Glutamic Acid calibration curve:

Equation	y = a + b*x
Plot	L Glutamic acid
Weight	No Weighting
Intercept	0.01923 ± 0.03016
Slope	5.04416E-4 ± 9.96058E-5
Residual Sum of Squares	0.00694
Pearson's r	0.93009
R-Square(COD)	0.86507
Limit of detection for L Glutamic Acid sensing: 125.91 nM	

Table 7.5: Curve fitting parameter for L Glutamic Acid Sensing

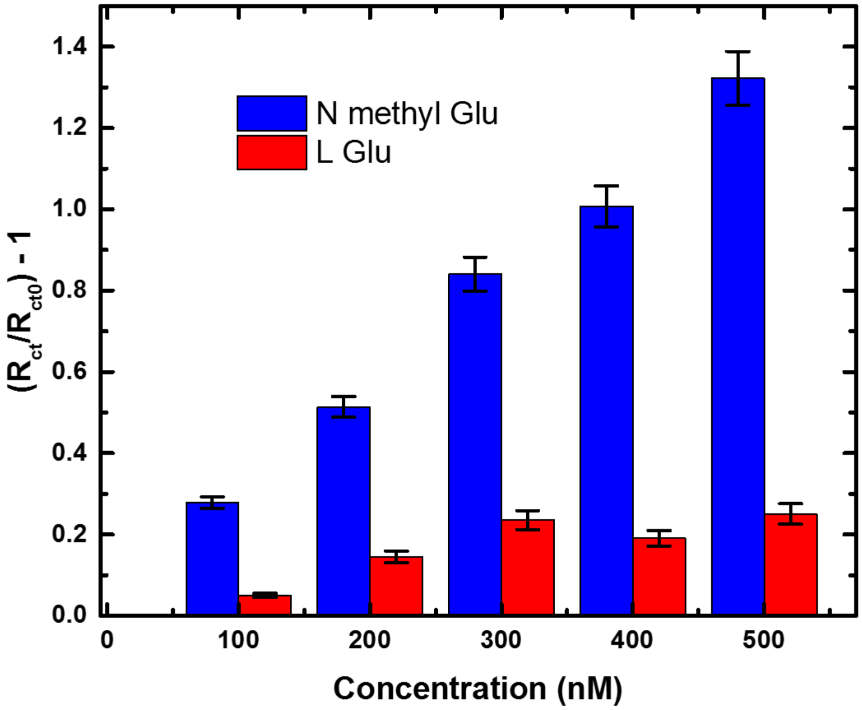

Figure 7.7: Calibration curve for N Methyl Glutamate and L Glutamic acid attachment

CHAPTER 8: CONCLUSION

This thesis discusses a new single-chain templated copolymer with predominantly noncovalent crosslinks as an alternative to structurally rigid traditional templated copolymers with much higher levels of covalent crosslinking. One of the most important observation was the tangling issues related with polymer backbone. Both homopolymers and copolymers of PNIPAM showed slow tangling with time. Using less concentrated templated polymer promoted less tangling and more uniform surface coverage than highly concentrated polymer solutions. The highly oriented and uniformly deposited polymers may yield maximum available binding sites though further investigation is needed.

A new templated polymer synthesis process has been optimized for better templating of the template and higher template recognition. FTIR and NMR techniques were used to identify functional monomers and their composition in lyophilized polymer powder before attachment to the electrode. XPS measurements showed the templated polymer deposition characteristics on electrode and helped to determine appropriate polymer concentration for ensuring maximum chemisorption.

Templated polymer based electrochemical sensor was tested in 3-electrode setup. Experimental data were collected using EIS technique. Impedimetric sensing mechanism was successfully carried out and good selectivities were observed for both 4NP and glutamate electrochemical sensor.

The proposed sensing mechanism discussed in this thesis relied on acid base crosslinking using MAA and 4-VP. In both cases, 4-VP was used as recognition monomer for analyte sensing. Binding with the template molecule within seconds is crucial for analyte sensing; however, further improvement into the synthesis of the TP like better RAFT agent should be investigated.

Traditional Au electrode used for electrochemical sensing usually has much larger diameter considering real life application, imposes greater challenges with signal reproduction and shows less signal to noise ratio. Custom electrode with smaller diameter integrated to microfluidic chip promises better sensitivity and accuracy for sensing low analyte concentration which will be investigated in coming days.

APPENDIX

Theoretical polymer chain length:

Chain length were varied by manipulating the ratio of monomer to RAFT agent (DDMAT). 0.1mmol per mL NIPAM was used for polymerization. If the total volume of polymerization is 100 mL, the volume of NIPAM is 10mmols.

All other functional monomers were scaled to NIPAM. For 50mer, 100mer, 200mer and 500 mer homo PNIPAM, RAFT agent DDMAT were used 0.2 mmol, 0.1 mmol, 0.05 mmol and 0.025 mmol respectively.

Polymer chain length estimation after synthesis:

After polymer synthesis, lyophilized powder can be used to observe the NMR spectra and mol% monomer composition can be estimated

For homo PNIPAM, the chemical shift at δ (~3.64 ppm) found due to [(-S-CH2(CH2)$_{10}$CH3) proton] are attributed to Z group of RAFT agent (DDMAT)[152]. The δ (~4.7 ppm) is attributed to methyl protons from NIPAM[150].

For the templated polymer, the chemical shift at δ (3.64 ppm) due to [(-S-CH2(CH2)10CH3) proton] are attributed to Z group of RAFT agent (DDMAT) [152]. The δ (4.0 ppm) is attributed to methyl protons from NIPAM [150]. The δ (~6.25 ppm) at peak 3 [-CH2] are attributed to MAA {Citation}. The δ (8.5 ppm) at peak 4 are from 4VP [8]. The molar ratio between functional monomer and NIPAM can be calculated via following equation:

$$\frac{Functional\ Monomer\ (Mol)}{NIPAM\ (Mol)} = \frac{\frac{A_1}{No.of\ Proton/s}}{\frac{A_2}{No.of\ Proton/s}}$$

The homo PNIPAM chain length can be estimated from NMR data as following:

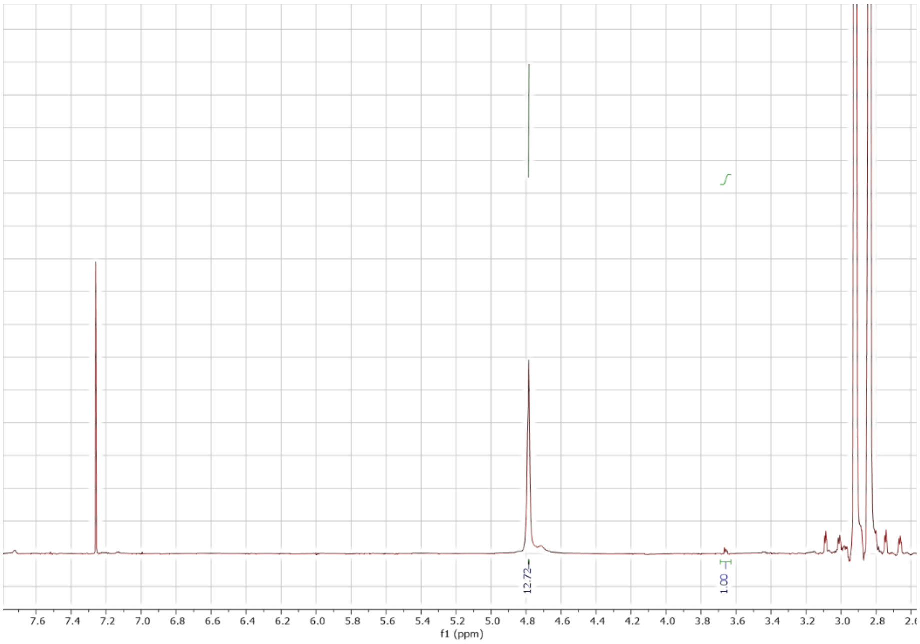

Chain Length Calculation:

Ratio between protons of CTA at δ= 3.7 ppm) and the methine protons of isopropyl group, δ= 4.8 ppm

Chain length =

$$\frac{\frac{Integration\ at\ \delta = 4.8\ \text{ppm}}{\#\ of\ proptons\ at\ \delta = 4.8\ \text{ppm}}}{\frac{Integration\ of at\ \delta = 3.7\ \text{ppm}}{\#\ of\ protons\ atat\ \delta = 3.7\ \text{ppm}}}$$

$$= \frac{\frac{12.72}{1}}{\frac{1}{4}} \approx \mathbf{50.88\ mer}$$

Figure 1: ^{1}H NMR spectra for 50 mer homo PNIPAM

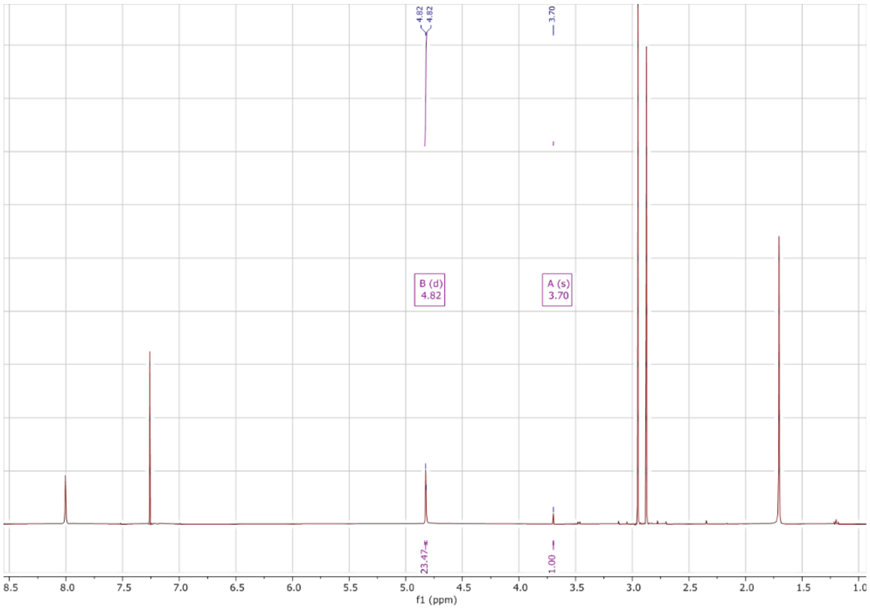

Chain Length Calculation:

Ratio between protons of CTA at δ= 3.7 ppm) and the methine protons of isopropyl group, δ= 4.8 ppm

Chain length =

$$\frac{\frac{Integration\ at\ \delta = 4.8\ \text{ppm}}{\#\ of\ proptons\ at\ \delta = 4.8\ \text{ppm}}}{\frac{Integration\ of at\ \delta = 3.7\ \text{ppm}}{\#\ of\ protons\ atat\ \delta = 3.7\ \text{ppm}}}$$

$$= \frac{\frac{23.47}{1}}{\frac{1}{4}} \approx \mathbf{94\ mer}$$

Figure 2: ^{1}H NMR spectra for 100 mer homo PNIPAM

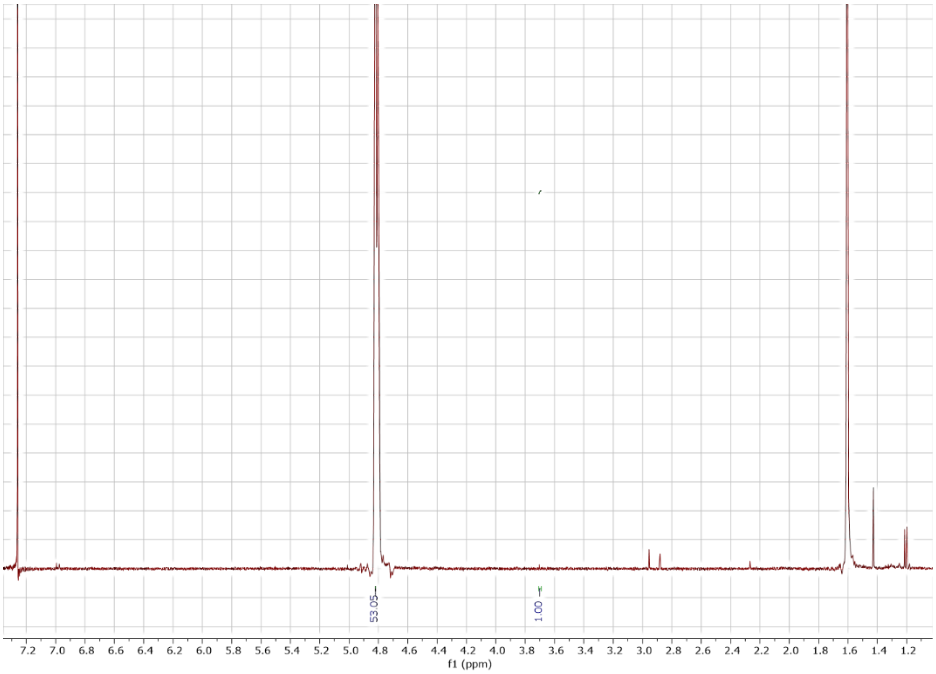

Chain Length Calculation:

Ratio between protons of CTA at δ= 3.7 ppm) and the methine protons of isopropyl group, δ= 4.8 ppm

Chain length =

$$\frac{\frac{Integration\ at\ \delta= 4.8\ \mathrm{ppm}}{\#\ of\ proptons\ \ at\ \delta= 4.8\ \mathrm{ppm}}}{\frac{Integration\ of at\ \delta= 3.7\ \mathrm{ppm}}{\#\ of\ protons\ atat\ \delta= 3.7\ \mathrm{ppm}}}$$

$$= \frac{\frac{53.05}{1}}{\frac{1}{4}} \approx \mathbf{212.2\ mer}$$

Figure 3: ^{1}H NMR spectra for 200 mer homo PNIPAM

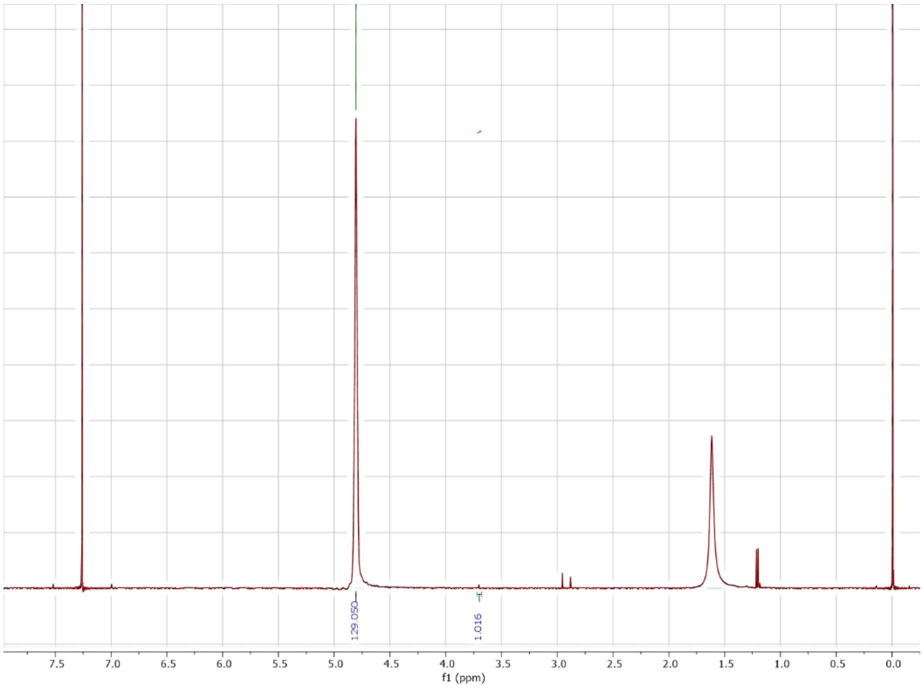

Chain Length Calculation:

Ratio between protons of CTA at δ= 3.7 ppm) and the methine protons of isopropyl group, δ= 4.8 ppm

Chain length =

$$\frac{\frac{Integration\ at\ \delta= 4.8\ \mathrm{ppm}}{\#\ of\ proptons\ \ at\ \delta= 4.8\ \mathrm{ppm}}}{\frac{Integration\ of at\ \delta= 3.7\ \mathrm{ppm}}{\#\ of\ protons\ atat\ \delta= 3.7\ \mathrm{ppm}}}$$

$$= \frac{\frac{129.05}{1}}{\frac{1.016}{4}} \approx \mathbf{508\ mer}$$

Figure 4: ^{1}H NMR spectra for 500 mer homo PNIPAM

XPS sample preparation and measurements:

For XPS measurements, A 60 nm gold initially coated on the top of the 5 nm Chromium (Cr) layer via thermal evaporation technique (Edwards E306A). The gold coated glass slides then patterned via photolithography. Before photolithography, the Au samples were rinsed respectively by acetone, ethanol, and D.I water and the dried via nitrogen flow. Before UV exposure, the examples were spin-coated with s1813 photoresist (MicropsitTM) and baked at 100°C for 1 min. After exposure, the samples developed in 319 developers followed with a rinse in D.I water and post bake at 120°C for 4 mins. The exposed metal area then wet etched via gold and chromium etchant to shape the distinguishable well-separated gold arrays on a glass slide. The sample gold arrays were then cut via glass cutter to form small pieces of the gold surface subjected to gentle THF and D.I water rinse followed by a blow-dry through N_2 gas before polymer deposition.

The PNIPAM-co-MAA-4VP100 polymer (0.5µg/ml) deposited via drop-casting having different exposure times with and without TCEP. The XPS studies performed at Kratos Axis Supra system with a base pressure of 10-9 Torr using the X-ray monochromatized radiation with a pass energy of 50 eV (resolution: 0.5 eV). Spectra were taken by averaging the measurements from four different spots of ~ 15µm for each sample. The XPS peak fitting was carried out using the Escape Data Acquisition System. All analysis of XPS spectra for polymer samples compared to the respective baseline spectra of the bare gold surface. The binding energy of each spectrum considers error within ±0.8eV.

The bare Au surface shows S2p peaks associated with SO_2 interaction (165.8eV) from the air. The S-O binding in the gold surface can occur possibly of binding via the S atom, the two oxygen atoms, and a combination of S and O [153]. During the bond between SO2 and metals, a transfer of electrons from the metal into the LUMO (lowest unoccupied molecular orbital) of SO2 plays a dominant role in the binding energy of the molecule [153]. The “d” valence appears high in the case of Au. Such a scenario leads to low electron donation into the LUMO of SO2, and the molecule adsorbs weakly and does not dissociate on extended Au surfaces [153]. The S2 (163.7eV) peak may arises from the interaction of the sulfur with the adventitious hydrocarbon species present in the bare Au surface [153], [155], [208].

LIST OF REFERENCES

[1] M. J. Whitcombe *et al.*, "The rational development of molecularly imprinted polymer-based sensors for protein detection," *Chem. Soc. Rev.*, vol. 40, no. 3, pp. 1547–1571, Feb. 2011, doi: 10.1039/C0CS00049C.

[2] K. Haupt, "Peer Reviewed: Molecularly Imprinted Polymers: The Next Generation," *Anal. Chem.*, vol. 75, no. 17, pp. 376 A-383 A, Sep. 2003, doi: 10.1021/ac031385h.

[3] K. Haupt and K. Mosbach, "Molecularly Imprinted Polymers and Their Use in Biomimetic Sensors," *Chem. Rev.*, vol. 100, no. 7, pp. 2495–2504, Jul. 2000, doi: 10.1021/cr990099w.

[4] A. Poma, A. Guerreiro, M. J. Whitcombe, E. V. Piletska, A. P. F. Turner, and S. A. Piletsky, "Solid-Phase Synthesis of Molecularly Imprinted Polymer Nanoparticles with a Reusable Template – 'Plastic Antibodies,'" *Adv. Funct. Mater.*, vol. 23, no. 22, pp. 2821–2827, Jun. 2013, doi: 10.1002/adfm.201202397.

[5] F. Ma, Y. Li, B. Tang, and C.-Y. Zhang, "Fluorescent Biosensors Based on Single-Molecule Counting," *Acc. Chem. Res.*, vol. 49, no. 9, pp. 1722–1730, 20 2016, doi: 10.1021/acs.accounts.6b00237.

[6] C. Ding, A. Zhu, and Y. Tian, "Functional Surface Engineering of C-Dots for Fluorescent Biosensing and in Vivo Bioimaging," *Acc. Chem. Res.*, vol. 47, no. 1, pp. 20–30, Jan. 2014, doi: 10.1021/ar400023s.

[7] U. Hanefeld, L. Gardossi, and E. Magner, "Understanding enzyme immobilisation," *Chem. Soc. Rev.*, vol. 38, no. 2, pp. 453–468, Feb. 2009, doi: 10.1039/b711564b.

[8] C. Mateo, J. M. Palomo, G. Fernandez-Lorente, J. M. Guisan, and R. Fernandez-Lafuente, "Improvement of enzyme activity, stability and selectivity via immobilization techniques," *Enzyme Microb. Technol.*, vol. 40, no. 6, pp. 1451–1463, May 2007, doi: 10.1016/j.enzmictec.2007.01.018.

[9] H. Chang *et al.*, "Layer-by-layer assembly of graphene, Au and poly(toluidine blue O) films sensor for evaluation of oxidative stress of tumor cells elicited by hydrogen peroxide.," *Biosens. Bioelectron.*, vol. 41, pp. 789–794, Mar. 2013, doi: 10.1016/j.bios.2012.10.001.

[10] Y. Zhang, X. Bai, X. Wang, K.-K. Shiu, Y. Zhu, and H. Jiang, "Highly Sensitive Graphene–Pt Nanocomposites Amperometric Biosensor and Its Application in Living Cell H2O2 Detection," *Anal. Chem.*, vol. 86, no. 19, pp. 9459–9465, Oct. 2014, doi: 10.1021/ac5009699.

[11] P. Wu, Z. Cai, Y. Gao, H. Zhang, and C. Cai, "Enhancing the electrochemical reduction of hydrogen peroxide based on nitrogen-doped graphene for measurement of its releasing process from living cells," *Chem. Commun.*, vol. 47, no. 40, pp. 11327–11329, Oct. 2011, doi: 10.1039/C1CC14419G.

[12] S. Borgmann, “Electrochemical quantification of reactive oxygen and nitrogen: challenges and opportunities.,” *Anal. Bioanal. Chem.*, vol. 394, no. 1, pp. 95–105, May 2009, doi: 10.1007/s00216-009-2692-1.

[13] Y. Luo, H. Liu, Q. Rui, and Y. Tian, “Detection of Extracellular H2O2 Released from Human Liver Cancer Cells Based on TiO2 Nanoneedles with Enhanced Electron Transfer of Cytochrome c,” *Anal. Chem.*, vol. 81, no. 8, pp. 3035–3041, Apr. 2009, doi: 10.1021/ac802721x.

[14] G. Yu, W. Wu, X. Pan, Q. Zhao, X. Wei, and Q. Lu, “High Sensitive and Selective Sensing of Hydrogen Peroxide Released from Pheochromocytoma Cells Based on Pt-Au Bimetallic Nanoparticles Electrodeposited on Reduced Graphene Sheets,” *Sensors*, vol. 15, no. 2, pp. 2709–2722, Feb. 2015, doi: 10.3390/s150202709.

[15] L. Lin *et al.*, “Intrinsic peroxidase-like catalytic activity of nitrogen-doped graphene quantum dots and their application in the colorimetric detection of H2O2 and glucose,” *Anal. Chim. Acta*, vol. 869, pp. 89–95, Apr. 2015, doi: 10.1016/j.aca.2015.02.024.

[16] F. Wen, Y. Dong, L. Feng, S. Wang, S. Zhang, and X. Zhang, “Horseradish Peroxidase Functionalized Fluorescent Gold Nanoclusters for Hydrogen Peroxide Sensing,” *Anal. Chem.*, vol. 83, no. 4, pp. 1193–1196, Feb. 2011, doi: 10.1021/ac1031447.

[17] Y. Shi, P. Su, Y. Wang, and Y. Yang, “Fe3O4 peroxidase mimetics as a general strategy for the fluorescent detection of H2O2-involved systems.,” *Talanta*, vol. 130, pp. 259–264, Dec. 2014, doi: 10.1016/j.talanta.2014.06.053.

[18] P. Gimeno *et al.*, “High-performance liquid chromatography method for the determination of hydrogen peroxide present or released in teeth bleaching kits and hair cosmetic products,” *J. Pharm. Biomed. Anal.*, vol. 107, pp. 386–393, Mar. 2015, doi: 10.1016/j.jpba.2015.01.018.

[19] D. Yu, P. Wang, Y. Zhao, and A. Fan, “Iodophenol blue-enhanced luminol chemiluminescence and its application to hydrogen peroxide and glucose detection.,” *Talanta*, vol. 146, pp. 655–661, Jan. 2016, doi: 10.1016/j.talanta.2015.06.059.

[20] S. Chakraborty and C. R. Raj, “Pt nanoparticle-based highly sensitive platform for the enzyme-free amperometric sensing of H2O2.,” *Biosens. Bioelectron.*, vol. 24, no. 11, pp. 3264–3268, Jul. 2009, doi: 10.1016/j.bios.2009.04.015.

[21] J. Li, Y. Li, Y. Zhang, and G. Wei, “Highly Sensitive Molecularly Imprinted Electrochemical Sensor Based on the Double Amplification by an Inorganic Prussian Blue Catalytic Polymer and the Enzymatic Effect of Glucose Oxidase,” *Anal. Chem.*, vol. 84, no. 4, pp. 1888–1893, Feb. 2012, doi: 10.1021/ac2026817.

[22] X. M. Chen *et al.*, “Nonenzymatic amperometric sensing of glucose by using palladium nanoparticles supported on functional carbon nanotubes.,” *Biosens. Bioelectron.*, vol. 25, no. 7, pp. 1803–1808, Mar. 2010, doi: 10.1016/j.bios.2009.12.035.

[23] R. C. Bianchi, E. R. da Silva, L. H. Dall‘Antonia, F. F. Ferreira, and W. A. Alves, “A Nonenzymatic Biosensor Based on Gold Electrodes Modified with Peptide Self-Assemblies for Detecting Ammonia and Urea Oxidation,” *Langmuir*, vol. 30, no. 38, pp. 11464–11473, Sep. 2014, doi: 10.1021/la502315m.

[24] H. Chen, X. Wang, G. Liu, A. Lin, Y. Wen, and H. Yang, “Electrochemical construction of porous gold nanostructures on DVD substrate and its application as nonenzymatic hydrogen peroxide sensor,” *Sci. China Chem.*, vol. 58, no. 10, pp. 1585–1592, Oct. 2015, doi: 10.1007/s11426-015-5403-0.

[25] X. Qin, H. Wang, Z. Miao, J. Li, and Q. Chen, “A novel non-enzyme hydrogen peroxide sensor based on catalytic reduction property of silver nanowires.,” *Talanta*, vol. 139, pp. 56–61, Jul. 2015, doi: 10.1016/j.talanta.2015.02.037.

[26] P. Lu *et al.*, “Synthesis and characterization of nickel oxide hollow spheres–reduced graphene oxide–nafion composite and its biosensing for glucose,” *Sens. Actuators B Chem.*, vol. 208, pp. 90–98, Mar. 2015, doi: 10.1016/j.snb.2014.10.140.

[27] O. G. Sahin, “Microwave-assisted synthesis of PtAu@C based bimetallic nanocatalysts for non-enzymatic H2O2 sensor,” *Electrochimica Acta*, vol. 180, pp. 873–878, Oct. 2015, doi: 10.1016/j.electacta.2015.09.015.

[28] Y. Zhang *et al.*, “Graphene quantum dots/gold electrode and its application in living cell H2O2 detection,” *Nanoscale*, vol. 5, no. 5, pp. 1816–1819, Mar. 2013, doi: 10.1039/c3nr33954h.

[29] M. Cieplak and W. Kutner, “Artificial Biosensors: How Can Molecular Imprinting Mimic Biorecognition?,” *Trends Biotechnol.*, vol. 34, no. 11, pp. 922–941, Nov. 2016, doi: 10.1016/j.tibtech.2016.05.011.

[30] W. Zhang *et al.*, “Preparation, Characterization and Application of a Molecularly Imprinted Polymer for Selective Recognition of Sulpiride,” *Materials*, vol. 10, no. 5, p. 475, May 2017, doi: 10.3390/ma10050475.

[31] S. Kia, M. Fazilati, H. Salavati, and S. Bohlooli, “Preparation of a novel molecularly imprinted polymer by the sol–gel process for solid phase extraction of vitamin D3,” *RSC Adv.*, vol. 6, no. 38, pp. 31906–31914, Mar. 2016, doi: 10.1039/C6RA04627D.

[32] A. N. M. B. El-hoshoudy, “Emulsion Polymerization Mechanism,” *Recent Res. Polym.*, Jan. 2018, doi: 10.5772/intechopen.72143.

[33] C. Grenier, “Rapid, High Affinity Binding by Molecularly Imprinted Poly(N-isopropylacrylamide) Copolymers with Mostly Non-Covalent Crosslinks for Chemical Sensing and Separation Applications,” *Dr. Diss.*, Jan. 2016, [Online]. Available: https://scholars.unh.edu/dissertation/2267.

[34] T. G. Drummond, M. G. Hill, and J. K. Barton, “Electrochemical DNA sensors,” *Nat. Biotechnol.*, vol. 21, no. 10, pp. 1192–1199, Oct. 2003, doi: 10.1038/nbt873.

[35] R. Monošík, M. Streďanský, and E. Šturdík, “Biosensors - classification, characterization and new trends,” *Acta Chim. Slovaca*, vol. 5, no. 1, pp. 109–120, Apr. 2012, doi: 10.2478/v10188-012-0017-z.

[36] A. Turner, I. Karube, and G. S. Wilson, *Biosensors : Fundamentals and Applications*. Oxford University Press, 1987.

[37] J.-M. Moon, N. Thapliyal, K. K. Hussain, R. N. Goyal, and Y.-B. Shim, “Conducting polymer-based electrochemical biosensors for neurotransmitters: A review,” *Biosens. Bioelectron.*, vol. 102, pp. 540–552, Apr. 2018, doi: 10.1016/j.bios.2017.11.069.

[38] X. Guo, “Single-Molecule Electrical Biosensors Based on Single-Walled Carbon Nanotubes,” *Adv. Mater.*, vol. 25, no. 25, pp. 3397–3408, Jul. 2013, doi: 10.1002/adma.201301219.

[39] M. A. Booth, S. Harbison, and J. Travas-Sejdic, “Development of an electrochemical polypyrrole-based DNA sensor and subsequent studies on the effects of probe and target length on performance,” *Biosens. Bioelectron.*, vol. 28, no. 1, pp. 362–367, Oct. 2011, doi: 10.1016/j.bios.2011.07.051.

[40] B. Kannan, D. E. Williams, M. A. Booth, and J. Travas-Sejdic, “High-Sensitivity, Label-Free DNA Sensors Using Electrochemically Active Conducting Polymers,” *Anal. Chem.*, vol. 83, no. 9, pp. 3415–3421, May 2011, doi: 10.1021/ac1033243.

[41] B. Zhu, M. A. Booth, P. Shepherd, A. Sheppard, and J. Travas-Sejdic, “Distinguishing cytosine methylation using electrochemical, label-free detection of DNA hybridization and ds-targets,” *Biosens. Bioelectron.*, vol. 64, pp. 74–80, Feb. 2015, doi: 10.1016/j.bios.2014.08.049.

[42] B. Kim, I. H. Jung, M. Kang, H.-K. Shim, and H. Y. Woo, “Cationic Conjugated Polyelectrolytes-Triggered Conformational Change of Molecular Beacon Aptamer for Highly Sensitive and Selective Potassium Ion Detection,” *J. Am. Chem. Soc.*, vol. 134, no. 6, pp. 3133–3138, Feb. 2012, doi: 10.1021/ja210360v.

[43] H. Peng, L. Zhang, T. H. M. Kjällman, and C. Soeller, “DNA Hybridization Detection with Blue Luminescent Quantum Dots and Dye-Labeled Single-Stranded DNA,” *J. Am. Chem. Soc.*, vol. 129, no. 11, pp. 3048–3049, Mar. 2007, doi: 10.1021/ja0685452.

[44] A. R. G. Srinivas, H. Peng, D. Barker, and J. Travas-Sejdic, “Switch on or switch off: An optical DNA sensor based on poly(p-phenylenevinylene) grafted magnetic beads,” *Biosens. Bioelectron.*, vol. 35, no. 1, pp. 498–502, May 2012, doi: 10.1016/j.bios.2012.03.022.

[45] null Janshoff, null Galla, and null Steinem, “Piezoelectric Mass-Sensing Devices as Biosensors-An Alternative to Optical Biosensors?,” *Angew. Chem. Int. Ed Engl.*, vol. 39, no. 22, pp. 4004–4032, Nov. 2000.

[46] K. A. Marx, “Quartz Crystal Microbalance: A Useful Tool for Studying Thin Polymer Films and Complex Biomolecular Systems at the Solution−Surface Interface,” *Biomacromolecules*, vol. 4, no. 5, pp. 1099–1120, Sep. 2003, doi: 10.1021/bm020116i.

[47] D. L. Graham, H. A. Ferreira, N. Feliciano, P. P. Freitas, L. A. Clarke, and M. D. Amaral, “Magnetic field-assisted DNA hybridisation and simultaneous detection using micron-sized spin-valve sensors and magnetic nanoparticles,” *Sens. Actuators B Chem.*, vol. 107, no. 2, pp. 936–944, Jun. 2005, doi: 10.1016/j.snb.2004.12.071.

[48] N. Jaffrezic-Renault, C. Martelet, Y. Chevolot, and J.-P. Cloarec, “Biosensors and Bio-Bar Code Assays Based on Biofunctionalized Magnetic Microbeads,” *Sensors*, vol. 7, no. 4, pp. 589–614, Apr. 2007.

[49] Y. Zhang and D. Zhou, “Magnetic particle-based ultrasensitive biosensors for diagnostics,” *Expert Rev. Mol. Diagn.*, vol. 12, no. 6, pp. 565–571, Jul. 2012, doi: 10.1586/erm.12.54.

[50] R. Koncki, “Recent developments in potentiometric biosensors for biomedical analysis,” *Anal. Chim. Acta*, vol. 599, no. 1, pp. 7–15, Sep. 2007, doi: 10.1016/j.aca.2007.08.003.

[51] J. Halliwell, A. C. Savage, N. Buckley, and C. Gwenin, “Electrochemical impedance spectroscopy biosensor for detection of active botulinum neurotoxin,” *Sens. Bio-Sens. Res.*, vol. 2, pp. 12–15, Dec. 2014, doi: 10.1016/j.sbsr.2014.08.002.

[52] K. Haupt, “Molecularly imprinted polymers in analyticalchemistry,” *Analyst*, vol. 126, no. 6, pp. 747–756, Jan. 2001, doi: 10.1039/B102799A.

[53] M. C. Blanco-López, M. J. Lobo-Castañón, A. J. Miranda-Ordieres, and P. Tuñón-Blanco, “Electrochemical sensors based on molecularly imprinted polymers,” *TrAC Trends Anal. Chem.*, vol. 23, no. 1, pp. 36–48, Jan. 2004, doi: 10.1016/S0165-9936(04)00102-5.

[54] R. Gui, H. Jin, H. Guo, and Z. Wang, “Recent advances and future prospects in molecularly imprinted polymers-based electrochemical biosensors,” *Biosens. Bioelectron.*, vol. 100, pp. 56–70, Feb. 2018, doi: 10.1016/j.bios.2017.08.058.

[55] S. Suriyanarayanan, P. J. Cywinski, A. J. Moro, G. J. Mohr, and W. Kutner, “Chemosensors Based on Molecularly Imprinted Polymers,” in *Molecular Imprinting*, Springer, Berlin, Heidelberg, 2010, pp. 165–265.

[56] J. Luo, C. Fan, X. Wang, R. Liu, and X. Liu, “A novel electrochemical sensor for paracetamol based on molecularly imprinted polymeric micelles,” *Sens. Actuators B Chem.*, vol. 188, pp. 909–916, Nov. 2013, doi: 10.1016/j.snb.2013.07.088.

[57] K. E. Sapsford, C. Bradburne, J. B. Delehanty, and I. L. Medintz, “Sensors for detecting biological agents,” *Mater. Today*, vol. 11, no. 3, pp. 38–49, Mar. 2008, doi: 10.1016/S1369-7021(08)70018-X.

[58] X.-B. Zhang, Z. Wang, H. Xing, Y. Xiang, and Y. Lu, “Catalytic and Molecular Beacons for Amplified Detection of Metal Ions and Organic Molecules with High Sensitivity,” *Anal. Chem.*, vol. 82, no. 12, pp. 5005–5011, Jun. 2010, doi: 10.1021/ac1009047.

[59] S. Liu *et al.*, “A novel label-free electrochemical aptasensor based on graphene–polyaniline composite film for dopamine determination,” *Biosens. Bioelectron.*, vol. 36, no. 1, pp. 186–191, Jun. 2012, doi: 10.1016/j.bios.2012.04.011.

[60] N. Karimian, M. B. Gholivand, and Gh. Malekzadeh, “Cefixime detection by a novel electrochemical sensor based on glassy carbon electrode modified with surface imprinted polymer/multiwall carbon nanotubes,” *J. Electroanal. Chem.*, vol. 771, pp. 64–72, Jun. 2016, doi: 10.1016/j.jelechem.2016.03.042.

[61] H. Wang, H. Zhao, X. Quan, and S. Chen, “Electrochemical Determination of Tetracycline Using Molecularly Imprinted Polymer Modified Carbon Nanotube-Gold Nanoparticles Electrode,” *Electroanalysis*, vol. 23, no. 8, pp. 1863–1869, Aug. 2011, doi: 10.1002/elan.201100049.

[62] H. M. V. Oliveira, F. T. C. Moreira, and M. G. F. Sales, “Ciprofloxacin-imprinted polymeric receptors as ionophores for potentiometric transduction,” *Electrochimica Acta*, vol. 56, no. 5, pp. 2017–2023, Feb. 2011, doi: 10.1016/j.electacta.2010.11.082.

[63] F. Long, Z. Zhang, Z. Yang, J. Zeng, and Y. Jiang, “Imprinted electrochemical sensor based on magnetic multi-walled carbon nanotube for sensitive determination of kanamycin,” *J. Electroanal. Chem.*, vol. 755, pp. 7–14, Oct. 2015, doi: 10.1016/j.jelechem.2015.07.018.

[64] S. Wei, Y. Liu, T. Hua, L. Liu, and H. Wang, “Molecularly imprinted electrochemical sensor for the determination of ampicillin based on a gold nanoparticle and multiwalled carbon nanotube-coated pt electrode,” *J. Appl. Polym. Sci.*, vol. 131, no. 16, Aug. 2014, doi: 10.1002/app.40613.

[65] T. Alizadeh and S. Azizi, “Graphene/graphite paste electrode incorporated with molecularly imprinted polymer nanoparticles as a novel sensor for differential pulse voltammetry determination of fluoxetine,” *Biosens. Bioelectron.*, vol. 81, pp. 198–206, Jul. 2016, doi: 10.1016/j.bios.2016.02.052.

[66] H. R. Rajabi and A. Zarezadeh, “Development of a new chemically modified carbon paste electrode based on nano-sized molecular imprinted polymer for selective and sensitive determination of naproxen,” *J. Mater. Sci. Mater. Electron.*, vol. 27, no. 10, pp. 10911–10920, Oct. 2016, doi: 10.1007/s10854-016-5202-1.

[67] A. Zamora-Gálvez, A. Ait-Lahcen, L. A. Mercante, E. Morales-Narváez, A. Amine, and A. Merkoçi, “Molecularly Imprinted Polymer-Decorated Magnetite Nanoparticles for Selective Sulfonamide Detection,” *Anal. Chem.*, vol. 88, no. 7, pp. 3578–3584, Apr. 2016, doi: 10.1021/acs.analchem.5b04092.

[68] F. Lu *et al.*, “Flow injection chemiluminescence sensor based on core–shell magnetic molecularly imprinted nanoparticles for determination of sulfadiazine,” *Anal. Chim. Acta*, vol. 718, pp. 84–91, Mar. 2012, doi: 10.1016/j.aca.2011.12.054.

[69] Q. Wang *et al.*, “Photoresponsive molecularly imprinted hydrogel casting membrane for the determination of trace tetracycline in milk,” *J. Mol. Recognit.*, vol. 29, no. 3, pp. 123–130, Mar. 2016, doi: 10.1002/jmr.2461.

[70] A. H. Kamel, W. H. Mahmoud, and M. S. Mostafa, “Biomimetic ciprofloxacin sensors made of molecularly imprinted network receptors for potential measurements,” *Anal. Methods*, vol. 3, no. 4, pp. 957–964, Apr. 2011, doi: 10.1039/C0AY00706D.

[71] Y. Yang, H. Niu, and H. Zhang, “Direct and Highly Selective Drug Optosensing in Real, Undiluted Biological Samples with Quantum-Dot-Labeled Hydrophilic Molecularly Imprinted Polymer Microparticles,” *ACS Appl. Mater. Interfaces*, vol. 8, no. 24, pp. 15741–15749, Jun. 2016, doi: 10.1021/acsami.6b04176.

[72] Y. Fuchs, O. Soppera, and K. Haupt, “Photopolymerization and photostructuring of molecularly imprinted polymers for sensor applications—A review,” *Anal. Chim. Acta*, vol. 717, pp. 7–20, Mar. 2012, doi: 10.1016/j.aca.2011.12.026.

[73] L. Zhang and L. Chen, “Fluorescence Probe Based on Hybrid Mesoporous Silica/Quantum Dot/Molecularly Imprinted Polymer for Detection of Tetracycline,” *ACS Appl. Mater. Interfaces*, vol. 8, no. 25, pp. 16248–16256, Jun. 2016, doi: 10.1021/acsami.6b04381.

[74] Y. Hu, Z. Zhang, H. Zhang, L. Luo, and S. Yao, “A sensitive and selective sensor-coated molecularly imprinted sol–gel film incorporating β-cyclodextrin-multi-walled carbon nanotubes and cobalt nanoparticles-chitosan for oxacillin determination,” *Surf. Interface Anal.*, vol. 44, no. 3, pp. 334–341, Mar. 2012, doi: 10.1002/sia.3807.

[75] B. Gao, X.-P. He, Y. Jiang, J.-T. Wei, H. Suo, and C. Zhao, “Computational simulation and preparation of fluorescent magnetic molecularly imprinted silica nanospheres for ciprofloxacin or norfloxacin sensing,” *J. Sep. Sci.*, vol. 37, no. 24, pp. 3753–3759, Dec. 2014, doi: 10.1002/jssc.201401014.

[76] N. Ktari *et al.*, “Design of a polypyrrole MIP-SAW sensor for selective detection of flumequine in aqueous media. Correlation between experimental results and DFT calculations,” *RSC Adv.*, vol. 5, no. 108, pp. 88666–88674, Oct. 2015, doi: 10.1039/C5RA16237H.

[77] W. Lian *et al.*, “Electrochemical sensor using neomycin-imprinted film as recognition element based on chitosan-silver nanoparticles/graphene-multiwalled carbon nanotubes composites modified electrode,” *Biosens. Bioelectron.*, vol. 44, pp. 70–76, Jun. 2013, doi: 10.1016/j.bios.2013.01.002.

[78] V. K. Gupta, M. L. Yola, N. Özaltın, N. Atar, Z. Üstündağ, and L. Uzun, “Molecular imprinted polypyrrole modified glassy carbon electrode for the determination of tobramycin,” *Electrochimica Acta*, vol. 112, pp. 37–43, Dec. 2013, doi: 10.1016/j.electacta.2013.08.132.

[79] A. Florea *et al.*, “Anticancer drug detection using a highly sensitive molecularly imprinted electrochemical sensor based on an electropolymerized microporous metal organic framework,” *Talanta*, vol. 138, pp. 71–76, Jun. 2015, doi: 10.1016/j.talanta.2015.01.013.

[80] M. Bougrini *et al.*, “Development of a novel sensitive molecularly imprinted polymer sensor based on electropolymerization of a microporous-metal-organic framework for tetracycline detection in honey,” *Food Control*, vol. 59, pp. 424–429, Jan. 2016, doi: 10.1016/j.foodcont.2015.06.002.

[81] M. Tertiş *et al.*, “Detection of Dopamine by a Biomimetic Electrochemical Sensor Based on Polythioaniline-Bridged Gold Nanoparticles,” *ChemPlusChem*, vol. 82, no. 4, pp. 561–569, Apr. 2017, doi: 10.1002/cplu.201600539.

[82] A. M. Rosengren, B. C. G. Karlsson, and I. A. Nicholls, “Consequences of Morphology on Molecularly Imprinted Polymer-Ligand Recognition,” *Int. J. Mol. Sci.*, vol. 14, no. 1, pp. 1207–1217, Jan. 2013, doi: 10.3390/ijms14011207.

[83] H. Niu, Y. Yang, and H. Zhang, “Efficient one-pot synthesis of hydrophilic and fluorescent molecularly imprinted polymer nanoparticles for direct drug quantification in real biological samples,” *Biosens. Bioelectron.*, vol. 74, pp. 440–446, Dec. 2015, doi: 10.1016/j.bios.2015.06.071.

[84] A. B. Descalzo, C. Somoza, M. C. Moreno-Bondi, and G. Orellana, “Luminescent Core–Shell Imprinted Nanoparticles Engineered for Targeted Förster Resonance Energy Transfer-Based Sensing,” *Anal. Chem.*, vol. 85, no. 11, pp. 5316–5320, Jun. 2013, doi: 10.1021/ac400520s.

[85] H. Sunayama, T. Ohta, A. Kuwahara, and T. Takeuchi, “Fluorescence signaling molecularly imprinted polymers for antibiotics prepared via site-directed post-imprinting introduction of plural fluorescent reporters within the recognition cavity,” *J. Mater. Chem. B*, vol. 4, no. 44, pp. 7138–7145, Nov. 2016, doi: 10.1039/C6TB02000C.

[86] S. Suriyanarayanan, S. Mandal, K. Ramanujam, and I. A. Nicholls, “Electrochemically synthesized molecularly imprinted polythiophene nanostructures as recognition elements for an aspirin-chemosensor,” *Sens. Actuators B Chem.*, vol. 253, pp. 428–436, Dec. 2017, doi: 10.1016/j.snb.2017.05.076.

[87] Z. Iskierko *et al.*, “Molecularly Imprinted Polymer (MIP) Film with Improved Surface Area Developed by Using Metal–Organic Framework (MOF) for Sensitive Lipocalin (NGAL) Determination,” *ACS Appl. Mater. Interfaces*, vol. 8, no. 31, pp. 19860–19865, Aug. 2016, doi: 10.1021/acsami.6b05515.

[88] A. Fernández-González, R. Badía Laíño, M. E. Diaz-García, L. Guardia, and A. Viale, “Assessment of molecularly imprinted sol–gel materials for selective room temperature phosphorescence recognition of nafcillin,” *J. Chromatogr. B*, vol. 804, no. 1, pp. 247–254, May 2004, doi: 10.1016/j.jchromb.2003.12.030.

[89] J. Czulak *et al.*, “Formation of target-specific binding sites in enzymes: solid-phase molecular imprinting of HRP,” *Nanoscale*, vol. 8, no. 21, pp. 11060–11066, May 2016, doi: 10.1039/C6NR02009G.

[90] L. Chen, X. Wang, W. Lu, X. Wu, and J. Li, “Molecular imprinting: perspectives and applications,” *Chem. Soc. Rev.*, vol. 45, no. 8, pp. 2137–2211, Apr. 2016, doi: 10.1039/C6CS00061D.

[91] A. G. Mayes and M. J. Whitcombe, “Synthetic strategies for the generation of molecularly imprinted organic polymers,” *Adv. Drug Deliv. Rev.*, vol. 57, no. 12, pp. 1742–1778, Dec. 2005, doi: 10.1016/j.addr.2005.07.011.

[92] G. Selvolini and G. Marrazza, “MIP-Based Sensors: Promising New Tools for Cancer Biomarker Determination,” *Sensors*, vol. 17, no. 4, Mar. 2017, doi: 10.3390/s17040718.

[93] “Effect of Chemical Crosslinking on Properties of Polymer Microbeads: A Review,” *Can. Chem. Trans.*, pp. 473–485, Jan. 2016, doi: 10.13179/canchemtrans.2015.03.04.0245.

[94] “Electrochemical Methods: Fundamentals and Applications, 2nd Edition,” *Wiley.com*. https://www.wiley.com/en-us/Electrochemical+Methods%3A+Fundamentals+and+Applications%2C+2nd+Edition-p-9780471043720 (accessed May 11, 2018).

[95] V. Mirceski, R. Gulaboski, M. Lovric, I. Bogeski, R. Kappl, and M. Hoth, “Square-Wave Voltammetry: A Review on the Recent Progress,” *Electroanalysis*, vol. 25, no. 11, pp. 2411–2422, Nov. 2013, doi: 10.1002/elan.201300369.

[96] D. A. C. Brownson and C. E. Banks, “Graphene electrochemistry: Fabricating amperometric biosensors,” *Analyst*, vol. 136, no. 10, pp. 2084–2089, Apr. 2011, doi: 10.1039/C0AN00875C.

[97] H. Cesiulis, N. Tsyntsaru, A. Ramanavicius, and G. Ragoisha, “The Study of Thin Films by Electrochemical Impedance Spectroscopy,” in *Nanostructures and Thin Films for Multifunctional Applications*, Springer, Cham, 2016, pp. 3–42.

[98] H. Helmholtz, “Ueber einige Gesetze der Vertheilung elektrischer Ströme in körperlichen Leitern mit Anwendung auf die thierisch-elektrischen Versuche,” *Ann. Phys.*, vol. 165, no. 6, pp. 211–233, 1853, doi: 10.1002/andp.18531650603.

[99] Bockris J. O’m., Devanathan M. A. V., Müller K., and Butler John Alfred Valentine, “On the structure of charged interfaces,” *Proc. R. Soc. Lond. Ser. Math. Phys. Sci.*, vol. 274, no. 1356, pp. 55–79, Jun. 1963, doi: 10.1098/rspa.1963.0114.

[100] “Analytical Electrochemistry, 3rd Edition,” *Wiley.com*. https://www.wiley.com/en-us/Analytical+Electrochemistry%2C+3rd+Edition-p-9780471678793 (accessed Mar. 21, 2019).

[101] N. Elgrishi, K. J. Rountree, B. D. McCarthy, E. S. Rountree, T. T. Eisenhart, and J. L. Dempsey, “A Practical Beginner’s Guide to Cyclic Voltammetry,” *J. Chem. Educ.*, vol. 95, no. 2, pp. 197–206, Feb. 2018, doi: 10.1021/acs.jchemed.7b00361.

[102] J. Heinze, “Cyclic Voltammetry—‘Electrochemical Spectroscopy’. New Analytical Methods (25),” *Angew. Chem. Int. Ed. Engl.*, vol. 23, no. 11, pp. 831–847, 1984, doi: 10.1002/anie.198408313.

[103] E. J. Olson and P. Bühlmann, “Minimizing Hazardous Waste in the Undergraduate Analytical Laboratory: A Microcell for Electrochemistry,” *J. Chem. Educ.*, vol. 87, no. 11, pp. 1260–1261, Nov. 2010, doi: 10.1021/ed100495k.

[104] M. Khafaji, S. Shahrokhian, and M. Ghalkhani, “Electrochemistry of Levo-Thyroxin on Edge-Plane Pyrolytic Graphite Electrode: Application to Sensitive Analytical Determinations,” *Electroanalysis*, vol. 23, no. 8, pp. 1875–1880, 2011, doi: 10.1002/elan.201100204.

[105] C. Valero Vidal and A. Igual Muñoz, “Effect of physico-chemical properties of simulated body fluids on the electrochemical behaviour of CoCrMo alloy,” *Electrochimica Acta*, vol. 56, no. 24, pp. 8239–8248, Oct. 2011, doi: 10.1016/j.electacta.2011.06.068.

[106] C. Xhoffer, K. Van den Bergh, and H. Dillen, “Electrochemistry: a powerful analytical tool in steel research,” *Electrochimica Acta*, vol. 49, no. 17, pp. 2825–2831, Jul. 2004, doi: 10.1016/j.electacta.2004.01.072.

[107] S. C. Mukhopadhyay, “Sensing and Instrumentation for a Low Cost Intelligent Sensing System,” in *2006 SICE-ICASE International Joint Conference*, Oct. 2006, pp. 1075–1080, doi: 10.1109/SICE.2006.315815.

[108] S. C. Mukhopadhyay and C. P. Gooneratne, “A Novel Planar-Type Biosensor for Noninvasive Meat Inspection,” *IEEE Sens. J.*, vol. 7, no. 9, pp. 1340–1346, Sep. 2007, doi: 10.1109/JSEN.2007.903335.

[109] S. C. Mukhopadhyay, S. D. Choudhury, T. Allsop, V. Kasturi, and G. E. Norris, “Assessment of pelt quality in leather making using a novel non-invasive sensing approach,” *J. Biochem. Biophys. Methods*, vol. 70, no. 6, pp. 809–815, Apr. 2008, doi: 10.1016/j.jbbm.2007.07.003.

[110] S. C. Mukhopadhyay, G. S. Gupta, J. D. Woolley, and S. N. Demidenko, “Saxophone Reed Inspection Employing Planar Electromagnetic Sensors,” *IEEE Trans. Instrum. Meas.*, vol. 56, no. 6, pp. 2492–2503, Dec. 2007, doi: 10.1109/TIM.2007.908253.

[111] “Novel Sensors for Food Inspections.” http://www.sensorsportal.com/HTML/DIGEST/P_581.htm (accessed Apr. 08, 2019).

[112] A. R. M. Syaifudin, S. C. Mukhopadhyay, P. L. Yu, and, C. P. Gooneratne, and J. Kosel, “Characterizations and performance evaluations of thin film interdigital sensors for Gram-negative bacteria detection,” in *2011 Fifth International Conference on Sensing Technology*, Nov. 2011, pp. 181–186, doi: 10.1109/ICSensT.2011.6136959.

[113] A. R. M. Syaifudin, S. C. Mukhopadhyay, P. L. Yu, M. J. Haji-Sheikh, C. Chuang, and H. Wu, “Detection of natural bio-toxins using an improved design interdigital sensors,” in *2011 IEEE SENSORS*, Oct. 2011, pp. 1028–1031, doi: 10.1109/ICSENS.2011.6127038.

[114] A. R. M. Syaifudin, S. C. Mukhopadhyay, and P. L. Yu, “Modelling and fabrication of optimum structure of novel interdigital sensors for food inspection,” *Int. J. Numer. Model. Electron. Netw. Devices Fields*, vol. 25, no. 1, pp. 64–81, 2012, doi: 10.1002/jnm.813.

[115] M. S. Abdul Rahman *et al.*, “Detection of bacterial endotoxin in food: New planar interdigital sensors based approach,” *J. Food Eng.*, vol. 114, no. 3, pp. 346–360, Feb. 2013, doi: 10.1016/j.jfoodeng.2012.08.026.

[116] A. I. Zia *et al.*, “MEMS based impedimetric sensing of phthalates,” in *2013 IEEE International Instrumentation and Measurement Technology Conference (I2MTC)*, May 2013, pp. 855–860, doi: 10.1109/I2MTC.2013.6555536.

[117] “Impedance Spectroscopy: Theory, Experiment, and Applications, 2nd Edition,” *Wiley.com*. https://www.wiley.com/en-us/Impedance+Spectroscopy%3A+Theory%2C+Experiment%2C+and+Applications%2C+2nd+Edition-p-9780471647492 (accessed Apr. 08, 2019).

[118] “Gold Electrode (Au) for voltammetry 3.0 mm dia.” https://www.basinc.com/products/MF-2114 (accessed Apr. 09, 2019).

[119] “Ag/AgCl (3M NaCl) Reference Electrode.” https://www.basinc.com/products/471 (accessed Apr. 09, 2019).

[120] “Platinum Coil Auxiliary Electrode.” https://www.basinc.com/products/794 (accessed Apr. 09, 2019).

[121] “Atom Transfer Radical Polymerization - Chemical Reviews (ACS Publications).” https://pubs.acs.org/doi/abs/10.1021/cr940534g (accessed May 16, 2018).

[122] “Living Free-Radical Polymerization by Reversible Addition−Fragmentation Chain Transfer: The RAFT Process - Macromolecules (ACS Publications).” https://pubs.acs.org/doi/pdf/10.1021/ma9804951 (accessed May 16, 2018).

[123] G. Moad, E. Rizzardo, and S. H. Thang, “Living Radical Polymerization by the RAFT Process – A Third Update,” *Aust. J. Chem.*, vol. 65, no. 8, pp. 985–1076, Sep. 2012, doi: 10.1071/CH12295.

[124] “Macromolecular Design via the Interchange of Xanthates (MADIX): Polymerization of Styrene with O-Ethyl Xanthates as Controlling Agents - Destarac - 2002 - Macromolecular Chemistry and Physics - Wiley Online Library.” https://onlinelibrary.wiley.com/doi/pdf/10.1002/macp.200290002 (accessed May 16, 2018).

[125] S. Z. Zard, “The Genesis of the Reversible Radical Addition–Fragmentation–Transfer of Thiocarbonylthio Derivatives from the Barton–McCombie Deoxygenation: A Brief Account and Some Mechanistic Observations*,” *Aust. J. Chem.*, vol. 59, no. 10, pp. 663–668, Nov. 2006, doi: 10.1071/CH06263.

[126] D. J. Keddie, “A guide to the synthesis of block copolymers using reversible-addition fragmentation chain transfer (RAFT) polymerization,” *Chem. Soc. Rev.*, vol. 43, no. 2, pp. 496–505, Dec. 2013, doi: 10.1039/C3CS60290G.

[127] “Expanding the Scope of RAFT Polymerization: Recent Advances and New Horizons - Macromolecules (ACS Publications).” https://pubs.acs.org/doi/abs/10.1021/acs.macromol.5b00342 (accessed May 17, 2018).

[128] J. B. McLeary, F. M. Calitz, J. M. McKenzie, M. P. Tonge, R. D. Sanderson, and B. Klumperman, “Beyond Inhibition: A 1H NMR Investigation of the Early Kinetics of RAFT-Mediated Polymerization with the Same Initiating and Leaving Groups,” *Macromolecules*, vol. 37, no. 7, pp. 2383–2394, Apr. 2004, doi: 10.1021/ma035478c.

[129] G. Moad, E. Rizzardo, and S. H. Thang, “Living Radical Polymerization by the RAFT Process – A Third Update,” *Aust. J. Chem.*, vol. 65, no. 8, pp. 985–1076, Sep. 2012, doi: 10.1071/CH12295.

[130] G. Moad, E. Rizzardo, and S. H. Thang, “Toward Living Radical Polymerization,” *Acc. Chem. Res.*, vol. 41, no. 9, pp. 1133–1142, Sep. 2008, doi: 10.1021/ar800075n.

[131] I. Bischofberger and V. Trappe, “New aspects in the phase behaviour of poly-N-isopropyl acrylamide: systematic temperature dependent shrinking of PNiPAM assemblies well beyond the LCST,” *Sci. Rep.*, vol. 5, p. 15520, Oct. 2015, doi: 10.1038/srep15520.

[132] V. Aseyev, H. Tenhu, and F. M. Winnik, “Non-ionic Thermoresponsive Polymers in Water,” in *Self Organized Nanostructures of Amphiphilic Block Copolymers II*, vol. 242, A. H. E. Müller and O. Borisov, Eds. Berlin, Heidelberg: Springer Berlin Heidelberg, 2010, pp. 29–89.

[133] V. Aseyev *et al.*, “Mesoglobules of thermoresponsive polymers in dilute aqueous solutions above the LCST,” *Polymer*, vol. 46, no. 18, pp. 7118–7131, Aug. 2005, doi: 10.1016/j.polymer.2005.05.097.

[134] A. V. Gorelov, A. Du Chesne, and K. A. Dawson, “Phase separation in dilute solutions of poly (N-isopropylacrylamide),” *Phys. Stat. Mech. Its Appl.*, vol. 240, no. 3, pp. 443–452, Jun. 1997, doi: 10.1016/S0378-4371(97)00192-1.

[135] P. Kujawa, V. Aseyev, H. Tenhu, and F. M. Winnik, “Temperature-Sensitive Properties of Poly(N-isopropylacrylamide) Mesoglobules Formed in Dilute Aqueous Solutions Heated above Their Demixing Point,” *Macromolecules*, vol. 39, no. 22, pp. 7686–7693, Oct. 2006, doi: 10.1021/ma061604b.

[136] W. Liao, Y. Zhang, Y. Guan, and X. X. Zhu, “Fractal Structures of the Hydrogels Formed in Situ from Poly(N-isopropylacrylamide) Microgel Dispersions,” *Langmuir*, vol. 28, no. 29, pp. 10873–10880, Jul. 2012, doi: 10.1021/la3016386.

[137] W. Liao, Y. Zhang, Y. Guan, and X. X. Zhu, “Gelation Kinetics of Thermosensitive PNIPAM Microgel Dispersions,” *Macromol. Chem. Phys.*, vol. 212, no. 18, pp. 2052–2060, Sep. 2011, doi: 10.1002/macp.201100137.

[138] C. Isarankura-Na-Ayudhya *et al.*, “Computational Insights on Sulfonamide Imprinted Polymers,” *Molecules*, vol. 13, no. 12, pp. 3077–3091, Dec. 2008, doi: 10.3390/molecules13123077.

[139] S. Xu, H. Lu, X. Zheng, and L. Chen, “Stimuli-responsive molecularly imprinted polymers: versatile functional materials,” *J. Mater. Chem. C*, vol. 1, no. 29, pp. 4406–4422, Jul. 2013, doi: 10.1039/C3TC30496E.

[140] C. Sun *et al.*, “The Multi-Template Molecularly Imprinted Polymer Based on SBA-15 for Selective Separation and Determination of Panax notoginseng Saponins Simultaneously in Biological Samples,” *Polymers*, vol. 9, no. 12, Nov. 2017, doi: 10.3390/polym9120653.

[141] C. H. H. Neufeld and C. S. Marvel, “The use of dialysis in polymer purification,” *J. Polym. Sci. [A1]*, vol. 4, no. 11, pp. 2907–2908, 1966, doi: 10.1002/pol.1966.150041117.

[142] A. Dong, S. J. Prestrelski, S. D. Allison, and J. F. Carpenter, “Infrared Spectroscopic Studies of Lyophilization- and Temperature-Induced Protein Aggregation,” *J. Pharm. Sci.*, vol. 84, no. 4, pp. 415–424, Apr. 1995, doi: 10.1002/jps.2600840407.

[143] “Lyophilization and development of solid protein pharmaceuticals - ScienceDirect.” https://www.sciencedirect.com/science/article/pii/S0378517300004233?via%3Dihub (accessed Mar. 21, 2019).

[144] M. H. Futscher, M. Philipp, P. Müller-Buschbaum, and A. Schulte, “The Role of Backbone Hydration of Poly(N-isopropyl acrylamide) Across the Volume Phase Transition Compared to its Monomer,” *Sci. Rep.*, vol. 7, no. 1, p. 17012, Dec. 2017, doi: 10.1038/s41598-017-17272-7.

[145] C. N. R. Rao, R. Venkataraghavan, and T. R. Kasturi, “Contribution to the infrared spectra of organosulphur compounds,” *Can. J. Chem.*, vol. 42, no. 1, pp. 36–42, Jan. 1964, doi: 10.1139/v64-006.

[146] W. Xu, X. Yin, G. He, J. Zhao, and H. Wang, “Photografted temperature-sensitive poly(N-isopropylacrylamide) thin film with a superfast response rate and an interesting transparent–opaque–transparent change in its deswelling process,” *Soft Matter*, vol. 8, no. 11, pp. 3105–3111, Feb. 2012, doi: 10.1039/C2SM07404D.

[147] O. O. Oyeneye, W. Z. Xu, and P. A. Charpentier, “Adhesive RAFT agents for controlled polymerization of acrylamide: effect of catechol-end R groups,” *RSC Adv.*, vol. 5, no. 94, pp. 76919–76926, Sep. 2015, doi: 10.1039/C5RA16193B.

[148] “Synthesis of magnetic, reactive, and thermoresponsive Fe3O4 nanoparticles via surface-initiated RAFT copolymerization of N-isopropylacrylamide and acrolein - Google Search.” https://www.google.com/search?q=Synthesis+of+magnetic%2C+reactive%2C+and+thermoresponsive+Fe3O4+nanoparticles+via+surface%E2%80%90initiated+RAFT+copolymerization+of+N%E2%80%90isopropylacrylamide+and+acrolein&rlz=1C1GCEA_enUS813US813&oq=Synthesis+of+magnetic%2C+reactive%2C+and+thermoresponsive+Fe3O4+nanoparticles+via+surface%E2%80%90initiated+RAFT+copolymerization+of+N%E2%80%90isopropylacrylamide+and+acrolein&aqs=chrome..69i57.1796j0j7&sourceid=chrome&ie=UTF-8 (accessed Jul. 02, 2019).

[149] Yanti, T. Nurhayati, I. Royani, Widayani, and Khairurrijal, “Synthesis and characterization of MAA-based molecularly-imprinted polymer (MIP) with D-glucose template,” *J. Phys. Conf. Ser.*, vol. 739, p. 012143, Aug. 2016, doi: 10.1088/1742-6596/739/1/012143.

[150] E. Tarabukina, A. Rozanova, A. Filippov, M. Constantin, V. Harabagiu, and G. Fundueanu, “Thermo- and pH-responsive phase separation of N-isopropylacrylamide with 4-vinylpyridine random copolymer in aqueous solutions,” *Colloid Polym. Sci.*, vol. 296, no. 3, pp. 557–565, Mar. 2018, doi: 10.1007/s00396-018-4269-z.

[151] X. Gao *et al.*, “pH- and thermo-responsive poly(N-isopropylacrylamide-co-acrylic acid derivative) copolymers and hydrogels with LCST dependent on pH and alkyl side groups,” *J. Mater. Chem. B*, vol. 1, no. 41, pp. 5578–5587, Oct. 2013, doi: 10.1039/C3TB20901F.

[152] Q. Zheng and C. Pan, “Preparation and characterization of dendrimer-star PNIPAAM using dithiobenzoate-terminated PPI dendrimer via RAFT polymerization,” *Eur. Polym. J.*, vol. 42, no. 4, pp. 807–814, Apr. 2006, doi: 10.1016/j.eurpolymj.2005.10.002.

[153] G. Liu, J. A. Rodriguez, J. Dvorak, J. Hrbek, and T. Jirsak, “Chemistry of sulfur-containing molecules on Au(111): thiophene, sulfur dioxide, and methanethiol adsorption,” *Surf. Sci.*, vol. 505, pp. 295–307, May 2002, doi: 10.1016/S0039-6028(02)01377-8.

[154] D. G. Castner, K. Hinds, and D. W. Grainger, “X-ray Photoelectron Spectroscopy Sulfur 2p Study of Organic Thiol and Disulfide Binding Interactions with Gold Surfaces,” *Langmuir*, vol. 12, no. 21, pp. 5083–5086, Jan. 1996, doi: 10.1021/la960465w.

[155] S. Krishnamurthy *et al.*, “Nitrogen ion irradiation of $\mathrm{Au}(110)$: Photoemission spectroscopy and possible crystal structures of gold nitride,” *Phys. Rev. B*, vol. 70, no. 4, p. 045414, Jul. 2004, doi: 10.1103/PhysRevB.70.045414.

[156] Y.-Z. Liu, M.-S. Chen, C.-C. Cheng, S.-H. Chen, and J.-K. Chen, “Fabrication of device with poly(N-isopropylacrylamide)-b-ssDNA copolymer brush for resistivity study,” *J. Nanobiotechnology*, vol. 15, no. 1, p. 68, Oct. 2017, doi: 10.1186/s12951-017-0303-4.

[157] J. V. Hollingsworth, N. V. S. D. K. Bhupathiraju, J. Sun, E. Lochner, M. G. H. Vicente, and P. S. Russo, “Preparation of Metalloporphyrin-Bound Superparamagnetic Silica Particles via ‘Click’ Reaction,” *ACS Appl. Mater. Interfaces*, vol. 8, no. 1, pp. 792–801, Jan. 2016, doi: 10.1021/acsami.5b10034.

[158] G. Greczynski and L. Hultman, “C 1s Peak of Adventitious Carbon Aligns to the Vacuum Level: Dire Consequences for Material’s Bonding Assignment by Photoelectron Spectroscopy,” *Chemphyschem*, vol. 18, no. 12, pp. 1507–1512, Jun. 2017, doi: 10.1002/cphc.201700126.

[159] “Protein Adsorption and Cell Adhesion/Detachment Behavior on Dual-Responsive Silicon Surfaces Modified with Poly(N-isopropylacrylamide)-block-polystyrene Copolymer | Langmuir.” https://pubs.acs.org/doi/pdf/10.1021/la904663m (accessed Jun. 28, 2019).

[160] S. Won, D. J. Phillips, M. Walker, and M. I. Gibson, “Co-operative transitions of responsive-polymer coated gold nanoparticles; precision tuning and direct evidence for co-operative aggregation,” *J. Mater. Chem. B*, vol. 4, no. 34, pp. 5673–5682, Aug. 2016, doi: 10.1039/C6TB01336H.

[161] H. H. Park, H. Park, A. C. Jamison, and T. R. Lee, “Colloidal stability evolution and completely reversible aggregation of gold nanoparticles functionalized with rationally designed free radical initiators,” *Colloid Polym. Sci.*, vol. 292, no. 2, pp. 411–421, Feb. 2014, doi: 10.1007/s00396-013-3071-1.

[162] Y. Tamai, H. Tanaka, and K. Nakanishi, “Molecular Dynamics Study of Polymer−Water Interaction in Hydrogels. 1. Hydrogen-Bond Structure,” *Macromolecules*, vol. 29, no. 21, pp. 6750–6760, Jan. 1996, doi: 10.1021/ma951635z.

[163] S. A. Deshmukh, S. K. R. S. Sankaranarayanan, K. Suthar, and D. C. Mancini, “Role of Solvation Dynamics and Local Ordering of Water in Inducing Conformational Transitions in Poly(N-isopropylacrylamide) Oligomers through the LCST,” *J. Phys. Chem. B*, vol. 116, no. 9, pp. 2651–2663, Mar. 2012, doi: 10.1021/jp210788u.

[164] A. K. Tucker and M. J. Stevens, “Study of the Polymer Length Dependence of the Single Chain Transition Temperature in Syndiotactic Poly(N-isopropylacrylamide) Oligomers in Water,” *Macromolecules*, vol. 45, no. 16, pp. 6697–6703, Aug. 2012, doi: 10.1021/ma300729z.

[165] G. Paradossi and E. Chiessi, “Tacticity-Dependent Interchain Interactions of Poly(N-Isopropylacrylamide) in Water: Toward the Molecular Dynamics Simulation of a Thermoresponsive Microgel,” *Gels*, vol. 3, no. 2, p. 13, Jun. 2017, doi: 10.3390/gels3020013.

[166] S. M. Larsson, “Simulations of polymer solutions displaying a lower critical solution temperature,” p. 26.

[167] C. W. Scales, A. J. Convertine, and C. L. McCormick, “Fluorescent Labeling of RAFT-Generated Poly(N-isopropylacrylamide) via a Facile Maleimide−Thiol Coupling Reaction,” *Biomacromolecules*, vol. 7, no. 5, pp. 1389–1392, May 2006, doi: 10.1021/bm060192b.

[168] R. Sips, “On the Structure of a Catalyst Surface. II,” *J. Chem. Phys.*, vol. 18, no. 8, pp. 1024–1026, Aug. 1950, doi: 10.1063/1.1747848.

[169] R. J. Umpleby, S. C. Baxter, Y. Chen, R. N. Shah, and K. D. Shimizu, “Characterization of Molecularly Imprinted Polymers with the Langmuir−Freundlich Isotherm,” *Anal. Chem.*, vol. 73, no. 19, pp. 4584–4591, Oct. 2001, doi: 10.1021/ac0105686.

[170] B. Charmas and R. Leboda, “Effect of surface heterogeneity on adsorption on solid surfaces: Application of inverse gas chromatography in the studies of energetic heterogeneity of adsorbents,” *J. Chromatogr. A*, vol. 886, no. 1, pp. 133–152, Jul. 2000, doi: 10.1016/S0021-9673(00)00432-5.

[171] W. Rudziński, A. Dominko, and B. W. Wojciechowski, “Mixed-gas adsorption on real solid surfaces: Lack of correlations between adsorption energies of various components related to the wide applicability of the generalized Langmuir-Freundlich isotherm equation,” *Chem. Eng. J. Biochem. Eng. J.*, vol. 64, no. 1, pp. 85–98, Oct. 1996, doi: 10.1016/S0923-0467(96)03118-1.

[172] Å. Larsson, "Assessment of polyclonal antibody binding of ligand by sips' equation or by the exact polyclonal equation. comparison of models," *Mol. Immunol.*, vol. 25, no. 12, pp. 1239–1249, Dec. 1988, doi: 10.1016/0161-5890(88)90038-7.

[173] H. Ardebrant and R. J. Pugh, "Surface acidity/basicity of road stone aggregates by adsorption from non-aqueous solutions," *Colloids Surf.*, vol. 53, no. 1, pp. 101–116, Jan. 1991, doi: 10.1016/0166-6622(91)80038-P.

[174] E. P. Randviir and C. E. Banks, "Electrochemical impedance spectroscopy: an overview of bioanalytical applications," *Anal. Methods*, vol. 5, no. 5, pp. 1098–1115, Feb. 2013, doi: 10.1039/C3AY26476A.

[175] J. H. Sluyters, "On the impedance of galvanic cells: I. Theory," *Recl. Trav. Chim. Pays-Bas*, vol. 79, no. 10, pp. 1092–1100, 1960, doi: 10.1002/recl.19600791013.

[176] V. Ganesh, S. K. Pal, S. Kumar, and V. Lakshminarayanan, "Self-assembled monolayers (SAMs) of alkoxycyanobiphenyl thiols on gold—A study of electron transfer reaction using cyclic voltammetry and electrochemical impedance spectroscopy," *J. Colloid Interface Sci.*, vol. 296, no. 1, pp. 195–203, Apr. 2006, doi: 10.1016/j.jcis.2005.08.051.

[177] A. Niazi and A. Yazdanipour, "Spectrophotometric simultaneous determination of nitrophenol isomers by orthogonal signal correction and partial least squares," *J. Hazard. Mater.*, vol. 146, no. 1, pp. 421–427, Jul. 2007, doi: 10.1016/j.jhazmat.2007.03.063.

[178] P. R. Gogate and A. B. Pandit, "A review of imperative technologies for wastewater treatment I: oxidation technologies at ambient conditions," *Adv. Environ. Res.*, vol. 8, no. 3, pp. 501–551, Mar. 2004, doi: 10.1016/S1093-0191(03)00032-7.

[179] J. C. Spain and D. T. Gibson, "Pathway for Biodegradation of p-Nitrophenol in a Moraxella sp," *Appl. Environ. Microbiol.*, vol. 57, no. 3, pp. 812–819, Mar. 1991.

[180] F. P. Carvalho, "Agriculture, pesticides, food security and food safety," *Environ. Sci. Policy*, vol. 9, no. 7, pp. 685–692, Nov. 2006, doi: 10.1016/j.envsci.2006.08.002.

[181] A. Asan and I. Isildak, "Determination of major phenolic compounds in water by reversed-phase liquid chromatography after pre-column derivatization with benzoyl chloride," *J. Chromatogr. A*, vol. 988, no. 1, pp. 145–149, Feb. 2003, doi: 10.1016/S0021-9673(02)02056-3.

[182] S. Dong, L. Chi, Z. Yang, P. He, Q. Wang, and Y. Fang, "Simultaneous determination of dihydroxybenzene and phenylenediamine positional isomers using capillary zone electrophoresis coupled with amperometric detection," *J. Sep. Sci.*, vol. 32, no. 18, pp. 3232–3238, Sep. 2009, doi: 10.1002/jssc.200900120.

[183] I. V. Cruz and O. Fatibello-Filho, "Biosensor based on paraffin/graphite modified with sweet potato tissue for the determination of hydroquinone in cosmetic cream in organic phase.," *Talanta*, vol. 52, no. 4, pp. 681–689, Jul. 2000.

[184] L. Han and X. Zhang, “Simultaneous Voltammetry Determination of Dihydroxybenzene Isomers by Nanogold Modified Electrode,” *Electroanalysis*, vol. 21, no. 2, pp. 124–129, 2009, doi: 10.1002/elan.200804403.

[185] L. Chen, Y. Tang, K. Wang, C. Liu, and S. Luo, “Direct electrodeposition of reduced graphene oxide on glassy carbon electrode and its electrochemical application,” *Electrochem. Commun.*, vol. 13, no. 2, pp. 133–137, Feb. 2011, doi: 10.1016/j.elecom.2010.11.033.

[186] D. M. Zhao, X. H. Zhang, L. J. Feng, L. Jia, and S. F. Wang, “Simultaneous determination of hydroquinone and catechol at PASA/MWNTs composite film modified glassy carbon electrode.,” *Colloids Surf. B Biointerfaces*, vol. 74, no. 1, pp. 317–321, Nov. 2009, doi: 10.1016/j.colsurfb.2009.07.044.

[187] B. Thirumalraj, C. Rajkumar, S.-M. Chen, and K.-Y. Lin, “Determination of 4-nitrophenol in water by use of a screen-printed carbon electrode modified with chitosan-crafted ZnO nanoneedles,” *J. Colloid Interface Sci.*, vol. 499, pp. 83–92, Aug. 2017, doi: 10.1016/j.jcis.2017.03.088.

[188] C. Yao, H. Sun, H.-F. Fu, and Z.-C. Tan, “Sensitive simultaneous determination of nitrophenol isomers at poly(p-aminobenzene sulfonic acid) film modified graphite electrode,” *Electrochimica Acta*, vol. 156, pp. 163–170, Feb. 2015, doi: 10.1016/j.electacta.2015.01.043.

[189] C. Li, Z. Wu, H. Yang, L. Deng, and X. Chen, “Reduced graphene oxide-cyclodextrin-chitosan electrochemical sensor: Effective and simultaneous determination of o- and p-nitrophenols,” *Sens. Actuators B Chem.*, vol. 251, pp. 446–454, Nov. 2017, doi: 10.1016/j.snb.2017.05.059.

[190] C. Yang, “Electrochemical Determination of 4-Nitrophenol Using a Single-Wall Carbon Nanotube Film-Coated Glassy Carbon Electrode,” *Microchim. Acta*, vol. 148, no. 1, pp. 87–92, Sep. 2004, doi: 10.1007/s00604-004-0240-4.

[191] Y. Zeng, Y. Zhou, T. Zhou, and G. Shi, “A novel composite of reduced graphene oxide and molecularly imprinted polymer for electrochemical sensing 4-nitrophenol,” *Electrochimica Acta*, vol. 130, pp. 504–511, Jun. 2014, doi: 10.1016/j.electacta.2014.02.130.

[192] M. Santhiago, C. S. Henry, and L. T. Kubota, “Low cost, simple three dimensional electrochemical paper-based analytical device for determination of p-nitrophenol,” *Electrochimica Acta*, vol. 130, pp. 771–777, Jun. 2014, doi: 10.1016/j.electacta.2014.03.109.

[193] Y. Tang, R. Huang, C. Liu, S. Yang, Z. Lu, and S. Luo, “Electrochemical detection of 4-nitrophenol based on a glassy carbon electrode modified with a reduced graphene oxide/Au nanoparticle composite,” *Anal. Methods*, vol. 5, no. 20, pp. 5508–5514, Sep. 2013, doi: 10.1039/C3AY40742J.

[194] X. X. Jiao, H. Q. Luo, and N. B. Li, “Fabrication of graphene–gold nanocomposites by electrochemical co-reduction and their electrocatalytic activity toward 4-nitrophenol oxidation,” *J. Electroanal. Chem.*, vol. 691, pp. 83–89, Feb. 2013, doi: 10.1016/j.jelechem.2012.12.013.

[195] L. Ai and J. Jiang, “Catalytic reduction of 4-nitrophenol by silver nanoparticles stabilized on environmentally benign macroscopic biopolymer hydrogel,” *Bioresour. Technol.*, vol. 132, pp. 374–377, Mar. 2013, doi: 10.1016/j.biortech.2012.10.161.

[196] P. S. da Silva, B. C. Gasparini, H. A. Magosso, and A. Spinelli, “Gold nanoparticles hosted in a water-soluble silsesquioxane polymer applied as a catalytic material onto an electrochemical sensor for detection of nitrophenol isomers,” *J. Hazard. Mater.*, vol. 273, pp. 70–77, May 2014, doi: 10.1016/j.jhazmat.2014.03.032.

[197] A. A. Rabi-Stanković *et al.*, “Electrooxidation of p-nitrophenol on organobentonite modified electrodes,” *Appl. Clay Sci.*, vol. 77–78, pp. 61–67, Jun. 2013, doi: 10.1016/j.clay.2013.04.003.

[198] L. Chen, X. Wang, W. Lu, X. Wu, and J. Li, “Molecular imprinting: perspectives and applications,” *Chem. Soc. Rev.*, vol. 45, no. 8, pp. 2137–2211, Apr. 2016, doi: 10.1039/C6CS00061D.

[199] J. Zhang, Q. Zhu, Y. Zhang, Z. Zhu, and Q. Liu, “Methanol Gas-Sensing Properties of SWCNT-MIP Composites,” *Nanoscale Res. Lett.*, vol. 11, no. 1, p. 522, Nov. 2016, doi: 10.1186/s11671-016-1675-3.

[200] E. Caro, N. Masqué, R. M. Marcé, F. Borrull, P. A. G. Cormack, and D. C. Sherrington, “Non-covalent and semi-covalent molecularly imprinted polymers for selective on-line solid-phase extraction of 4-nitrophenol from water samples,” *J. Chromatogr. A*, vol. 963, no. 1, pp. 169–178, Jul. 2002, doi: 10.1016/S0021-9673(02)00360-6.

[201] E. Herrero-Hernández, R. Carabias-Martínez, and E. Rodríguez-Gonzalo, “Behavior of Phenols and Phenoxyacids on a Bisphenol-A Imprinted Polymer. Application for Selective Solid-Phase Extraction from Water and Urine Samples,” *Int. J. Mol. Sci.*, vol. 12, no. 5, pp. 3322–3339, May 2011, doi: 10.3390/ijms12053322.

[202] X. Huang, L. Kong, X. Li, C. Zheng, and H. Zou, “Molecular imprinting of nitrophenol and hydroxybenzoic acid isomers: effect of molecular structure and acidity on imprinting,” *J. Mol. Recognit. JMR*, vol. 16, no. 6, pp. 406–411, Dec. 2003, doi: 10.1002/jmr.627.

[203] A.-E. Radi, “Electrochemical Aptamer-Based Biosensors: Recent Advances and Perspectives,” *International Journal of Electrochemistry*, 2011. https://www.hindawi.com/journals/ijelc/2011/863196/ (accessed Jul. 04, 2019).

[204] “Determination of Alanine Aminotransferase with an Electrochemical Nano Ir-C Biosensor for the Screening of Liver Diseases.” https://www.ncbi.nlm.nih.gov/pmc/articles/PMC4264364/ (accessed Mar. 10, 2019).

[205] T. Borisova *et al.*, “An amperometric glutamate biosensor for monitoring glutamate release from brain nerve terminals and in blood plasma,” *Anal. Chim. Acta*, vol. 1022, pp. 113–123, Aug. 2018, doi: 10.1016/j.aca.2018.03.015.

[206] S. Kurbanoglu, S. A. Ozkan, and A. Merkoçi, “Nanomaterials-based enzyme electrochemical biosensors operating through inhibition for biosensing applications,” *Biosens. Bioelectron.*, vol. 89, pp. 886–898, Mar. 2017, doi: 10.1016/j.bios.2016.09.102.

[207] L. Uzun and A. P. F. Turner, “Molecularly-imprinted polymer sensors: realising their potential,” *Biosens. Bioelectron.*, vol. 76, pp. 131–144, Feb. 2016, doi: 10.1016/j.bios.2015.07.013.

[208] J. A. Rodriguez *et al.*, “Activation of Gold on Titania: Adsorption and Reaction of SO2 on Au/TiO2(110),” *J. Am. Chem. Soc.*, vol. 124, no. 18, pp. 5242–5250, May 2002, doi: 10.1021/ja020115y.